# Assessment of Turbulence Modeling for Compressible Flow Around Stationary and Oscillating Cylinders

by

Alejandra Uranga
B.S. in Aerospace Engineering, Florida Institute of Technology, 2004

A Thesis Submitted in Partial Fulfillment of the
Requirements for the Degree of
MASTER OF APPLIED SCIENCE
in the
Department of Mechanical Engineering.



University of Victoria

# Assessment of Turbulence Modeling for Compressible Flow Around Stationary and Oscillating Cylinders

by

Alejandra Uranga
B.S. in Aerospace Engineering, Florida Institute of Technology, 2004

Supervisory Commitee

---

Dr. Nedjib Djilali, Supervisor (Dept. of Mechanical Engineering,
University of Victoria, BC, Canada)

---

Dr. Afzal Suleman, Supervisor (Dept. of Mechanical Engineering,
University of Victoria, BC, Canada)

---

Dr. Peter Oshkai, Departmental Member (Dept. of Mechanical Engineering,
University of Victoria, BC, Canada)

---

Dr. Frédéric Péneau, Outside Member (Dept. of Engineering and Aviation,
Euro American Institute of Technology, France)

---

Dr. Carl Ollivier-Gooch, External Examiner (Dept. of Mechanical Engineering,
University of British Columbia, BC, Canada)

Supervisory Commitee

Dr. Nedjib Djilali, Supervisor (Dept. of Mechanical Engineering, University of Victoria, BC, Canada)

Dr. Afzal Suleman, Supervisor (Dept. of Mechanical Engineering, University of Victoria, BC, Canada)

Dr. Peter Oshkai, Departmental Member (Dept. of Mechanical Engineering, University of Victoria, BC, Canada)

Dr. Frédéric Péneau, Outside Member (Dept. of Engineering and Aviation, Euro American Institute of Technology, France)

Dr. Carl Ollivier-Gooch, External Examiner (Dept. of Mechanical Engineering, University of British Columbia, BC, Canada)

# Abstract

A numerical analysis of the flow over stationary and transversely oscillating circular cylinders at Reynolds numbers of 3900 and 3600, respectively, is undertaken to assess various turbulence modeling techniques for the simulation of vortex shedding phenomena. Four turbulence models are considered, namely the one-equation Spalart-Allmaras model [Spalart & Allmaras (1994)] and the $k$-$\tau$ model by Speziale *et al.* (1992) for URANS closure, the constant-coefficient Smagorinsky-Lilly subgrid-scale model for Large Eddy Simulations, and the adaptive $k$-$\tau$ model proposed by Magagnato & Gabi (2002) for Very Large Eddy Simulations.

A key contribution of this work is comparison of results obtained with the same numerical procedure, discretization algorithms, and artificial dissipation but different

turbulence modeling techniques in order to properly differentiate between errors due to numerical and to modeling aspects.

Through the study of the flow around the stationary cylinder, it is shown that the use of an inadequate time step has a small effect on global average quantities, but a noticeable impact on the pressure coefficient around the cylinder, as well as on the evolution of velocity along the centerline, thus showing that simulations with too large a time step are unable to properly resolve the recirculation zone and wake. Global average quantities are found to be relatively insensitive to three-dimensional resolution.

Detailed analysis of three-dimensional URANS simulations reveals that the Spalart-Allmaras model is unable to properly predict the location of the separation point, separation being delayed significantly. This results in too small a mean recirculation zone, under-estimated back-pressure, and up to 25% over-estimation of the drag. Yet, this simple model provides an accurate value for the Strouhal number and good fluctuating velocity profiles. The $k$-$\tau$ Speziale turbulence model predicts all global quantities accurately, and yields good velocity profiles along the wake as well as an adequate pressure distribution on the cylinder wall.

Large and Very Large Eddy Simulations of the flow around a stationary cylinder reveal an important three-dimensionality, and the formation on the upper and lower surfaces of two secondary eddies in addition to the two large vortices. Furthermore, the LES properly captures the dynamics in the laminar boundary layer as reflected by the skin friction values even though it makes use of a constant coefficient Smagorinsky subgrid-scale model.

In the study of the transversely oscillating cylinder with two-dimensional URANS $k$-$\tau$ Speziale simulations, the lock-in region starts at significantly lower motion frequencies than observed in experimental results, while the phase shift was not observed. No numerical studies close to this Reynolds number are available in the literature, and further investigation is required.

# Table of Contents

# List of Tables

# List of Figures

# Acknowledgements

William Blake wrote that "the road of excess leads to the palace of wisdom" (The Marriage of Heaven and Hell, 1790-1793); I have always believe it to be true, but had never tasted its sweetness and bitterness so deeply as in the past two years. Still, these years in Victoria as a master's student have been fantastic.

For this I would like to acknowledge my two supervisors, Ned Djilali and Afzal Suleman. First for giving me the opportunity to be one of their students and for funding my studies. Second, and most importantly for giving me intellectual and moral support, each one of them in their very personal manner. Thank you Ned for the fruitful discussions, especially during the writing of this thesis. Thank you Afzal for all your advice on matters unrelated to my studies but important to my professional and personal life.

I could never have carried out this numerical work without the help of the main developer of the computational code, Franco Magagnato from the University of Karlsruhe, Germany. The email exchanges that we had and most particularly your ten days visit to Victoria this summer have made a precious contribution to my work. Thank you for sharing your expertise and long experience in computational fluid mechanics with me. It is amazing how you make everything seem "trivial".

Rumour has it that graduate students do not have a life... except for the life within graduate studies, in the lab. For making this part of my life such a nice experience, I thank Marc Secanell and Gonçalo Pedro, who were always there for either cheer me up, share my frustration, or laugh at my lack of luck (*i.e.* lack of convergence in the

simulations).

To Frédéric Péneau, I thank you for your guidance and for infecting me with the love of research and of computational fluid dynamics; thank you for being who you are and sharing it with me, for your truthfulness, your perseverance, your patience and lack thereof. Thanks for the evenings and weekends that we spent figuring out what was wrong with the turbulence models. It's been three summers in a row that we work together, and each summer has been more incredible than the previous one. Meet you next year.

To Julien, thank you for following me in my craziest adventures and paddling with me in the most calm lakes and most turbulent rivers. Your patience, understanding and love go beyond words; I wouldn't be here without you.

*to life*

# Chapter 1

# Introduction

In an address to the British Association for the Advancement of Science in 1932, Horace Lamb reportedly said "I am an old man now, and when I die and go to Heaven there are two matters on which I hope for enlightenment. One is quantum electrodynamics, and the other is the turbulent motion of fluids. And about the former I am really rather optimistic" [Goldstein (1969)]. More than seventy years later, there is still an enormous amount of facts to comprehend about turbulence, and it is my belief that the best years of turbulence research are still to come. The focus here is on the turbulent vortex shedding past circular cylinders.

With the exponential increase in computer power since the late 1960's and the accompanying decrease in costs, computational prediction of flows — usually referred to as Computational Fluid Dynamics, or CFD — is becoming more and more the preferred tool in fluid mechanics, being today as important as experimental procedures. Computational methods can be a good choice for industry because of their relatively low cost, but they have also great advantages to fundamental research. Not only do numerical simulations allow for better control of certain conditions and flow measurements without the use of intrusive probes, but most importantly they do not suffer from some limitations inherent to experimental techniques, such as difficulties

in obtaining accurate measurements of certain physical quantities, *e.g.* fluctuating pressure, and in reproducing high Mach and Reynolds number flows.

## 1.1 Motivation

The main purpose of this study is to compare the accuracy and effectiveness (*i.e.* computational cost relative to resulting accuracy) of turbulence modeling techniques for the simulation of vortex shedding phenomena, including turbulence models for Unsteady Reynolds-Averaged Navier-Stokes (URANS) equations, as well as subgrid-scale models for Large and Very Large Eddy Simulation (LES and VLES). The investigation focuses on the flow over stationary and oscillating circular cylinders as a test case configuration. Throughout this work the term turbulence modeling technique is used to refer to both turbulence models for URANS equations and sub-grid scale models for LES and VLES.

Tiny fibers in liquids, thin wires and cables in wind, chimney stacks, and rockets traveling in cross winds are all examples of problems involving a circular cylinder placed in a flow stream. The flow past a static circular cylinder has been studied in detail since the beginning or the twentieth century with the works by Bénard (1908), and yet it is still being considered both as a subject of interest in itself and as a validation tool. Its power as a validation case resides in its geometrical simplicity, which makes it easy to set up both experimentally and numerically, as well as in the availability of numerical and experimental data in the literature. Furthermore, the physical phenomena encountered are rich in variety and complexity, brought about by the interaction between three shear layers: the boundary layer, the separation free shear layer, and the wake.

Depending on the inflow Reynolds number, there can be no wake formation at all, a closed wake, or vortex shedding can take place while the flow may be fully laminar, partly turbulent, or fully turbulent. Transition to turbulence can take place in the

boundary layer around the cylinder, in the shear layer that follows separation, or in the wake; the different regimes are presented in the following section. The presence of a curved solid surface, and the resulting pressure gradient, generates a sensitive boundary layer and presents quantities that are appropriate for detailed comparisons, such as the variation of the pressure coefficient, the skin friction, or the separation point and even reattachment point. A thorough analysis of the mean fields can be undertaken, since mean quantities are sensitive enough to provide a good test for turbulence models. Additionally, the investigation of instantaneous boundary layer development and small as well as large coherent structures is also of great interest.

The choice of a problem for comparison of turbulence modeling techniques was thus relatively straightforward and consists of the flow past a circular cylinder, both when the cylinder is stationary and during oscillations in the transversal direction (perpendicular to the inflow). Through an in-depth validation of both the numerical code and discretization methods as well as turbulence modeling techniques, this study will prepare the field for simulations of more complex problems in fluid-structure interaction, such as the resolution of three-dimensional turbulent flow around a pitching-and-heaving (flapping) airfoil which is close to the propulsion method of fish and has never been undertaken (to the author's knowledge), or the fluid-strucure interaction in wings and bluff bodies, and other aeroelasticity problems.

Since a turbulence modeling technique should be able to correctly simulate both laminar and turbulent regions of the flow, the particular Reynolds number at which the stationary cylinder should be studied must be sufficiently high to ensure the flow is turbulent in certain regions but small enough for the boundary layer to remain laminar through its evolution, in order to observe the transition to turbulence in the shear layers that result from separation and whose dynamics are of crucial importance. Furthermore, since three-dimensional large eddy simulations without wall functions are to be carried out, the boundary layer needs to be properly resolved by the computational grid, and hence the choice of the Reynolds number is also determined by

the practical consideration of the available computational resources. Finally, accurate and detailed experimental and numerical data from the literature is required, and since this work is computational, the availability of Direct Numerical Simulation (DNS) and LES results is important. Therefore, the flow around a stationary circular cylinder is simulated at a Reynolds number based on cylinder diameter and inflow velocity, $Re_D = U_0 D/\nu$, of 3900, which corresponds to the so-called sub-critical regime.

Simulations of a cylinder oscillating transversely in uniform flow were undertaken at a Reynolds number of 3600, this choice being justified as follows. First, the physics of the flow must be similar to the ones observed in the case of the stationary cylinder, such that the Reynolds number must be close to 3900. However, the motion of the cylinder induces an higher effective flow velocity, and hence higher effective Reynolds number, compared to the stationary case. In order to use the same computational grid for both the static and oscillating cylinders, it is then desirable for the Reynolds number of the moving case to be slightly below the one chosen for the static case. Finally, data need to be available for comparison, and detailed experimental results have been reported in the literature for a Reynolds number of 3600. Since the literature review revealed that there are no numerical results available at, or close to, this Reynolds number, these simulations will also contribute to filling the gap.

Numerical simulations of a stationary cylinder in uniform flow in the sub-critical regime have been carried out by different research groups using a variety of turbulence modeling techniques (URANS, LES, DNS) and associated models (algebraic, eddy-viscosity, sub-grid scale models of different kinds and complexities), and comparisons between the results obtained by each group done in an attempt to justify the differences between the turbulence modeling techniques used. However, a study of the results obtained with *the same numerical procedure, discretization algorithms, and artificial dissipation* but different turbulence modeling techniques is not available, and would allow to properly differentiate between errors due to numerical and

to modeling considerations. This is particularly important in Large Eddy Simulations in which the grid determines both the discretization of the governing equations and the cut between the resolution of the equations and the sub-grid scale modeling of unresolved scales.

## 1.2 Background

Bénard (1908) and Kármán (1912) were the first to study the flow past a circular cylinder, experimentally and theoretically, respectively, while the first numerical solution was obtained at low Reynolds numbers by Thom (1933). Before the advent of modern computers, Kawaguti (1953) obtained a similar solution by using a mechanical desk calculator, working 20 hours per week for 18 months, totaling more than 1500 hours.

Since those early days, a great number of studies, theoretical, experimental, and numerical, have been published in the literature concerning the flow around stationary cylinders, and a fair amount on the transversely oscillating cylinder though only relatively few of numerical type. A brief and non-exhaustive review of some publications and major results is presented in this section, with emphasis on the flow regimes and phenomena that are of particular interest to the present study.

### 1.2.1 Stationary Cylinder

When a smooth bluff body, such as a circular cylinder, is placed in a uniform stream at relatively high Reynolds numbers, separation occurs along the continuous curvature and is not fixed as in the presence of sharp corners. The boundary layer that forms around the cylinder is subjected to a favorable pressure gradient on the half front of the object, followed by an adverse pressure gradient which induces separation. After separation, the boundary layer becomes a free shear layer bounding the wake.

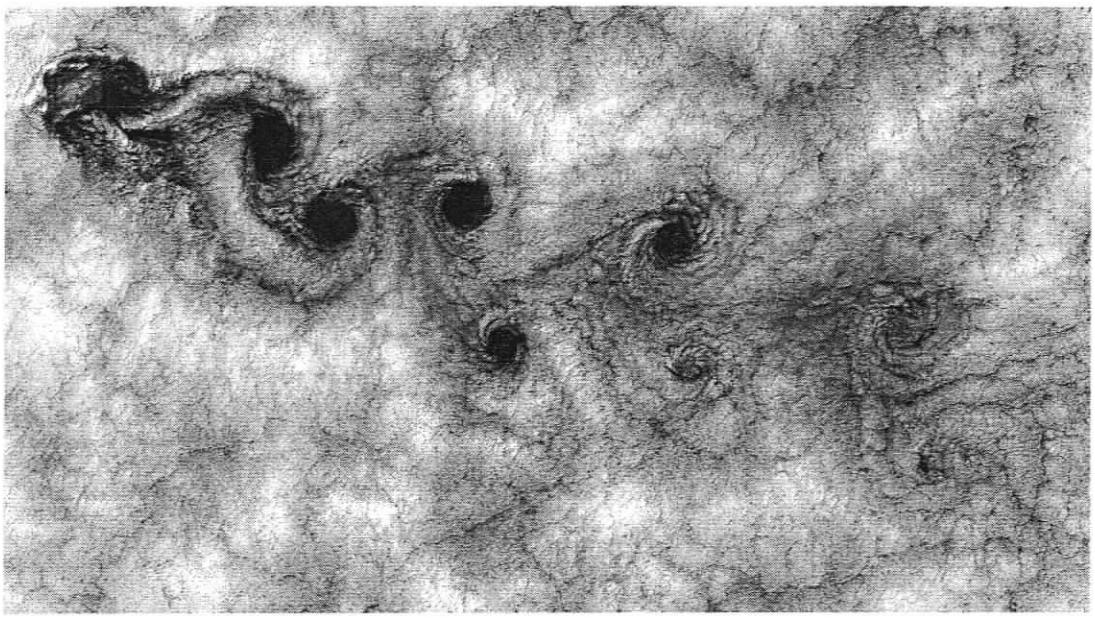

Figure 1.1: Kármán vortex street forming off the Chilean coast over Alexander Selkirk. The island's highest point rises 1.6 km over the surrounding sea-level and triggers the vortex shedding from wind-driven clouds, the tip of the obstacle over the clouds being around 9 km wide. (NASA image taken by Landsat 7 satellite on Sept. 15, 1999)

As stated earlier, studies on the flow around a cylinder can be found as early as the beginning of the twentieth century with the experimental works by Bénard (1908). When in 1912 Theodor von Kármán studied the theoretical stability of two rows of vortices, which came to be known as a Kármán vortex street (*i.e.* the periodic pattern of counter-rotating vortices caused by unsteady separation from a bluff body), the interest in such flows spread throughout the scientific community, not only because of its theoretical appeal but also for the beauty of the phenomena, as can be observed in Figure 1.1 which shows a Kármán vortex street forming off the Chilean coast over Alexander Selkirk Island and made visible by the clouds.

In practical applications, the value of the Reynolds number based on cylinder diameter "ranges from less than one up to a hundred for tiny fibers in liquids, from a few hundred to thousands for thin wires and cables in wind, and from a few million for chimney stacks to hundreds of millions for cooling towers and interplanetary rockets

exposed to high cross winds" [Zdravkovich (1997)]. Over these flow regimes, the flow can be from fully laminar with no separation nor wake, to fully turbulent. "A particular feature of the flow around bluff bodies, as first noted by Dryden and later elaborated by Roshko and Fiszdon, is a succession of transitions in various regions of the disturbed flow" [*id.*], which define the different flow regimes than may be encountered.

### Flow Regimes

When Berger & Wille (1972) published their review on "Periodic Flow Phenomena", which deals mostly with the widely studied flow past a circular cylinder, there were still many undetermined issues and controversies; it was not always clear if observations were related to the vortex shedding phenomena or to the experimental conditions. Yet, and in spite of the lack of convincing physical explanations, most of the phenomena that are known today were already described.

Williamson (1996) and Zdravkovich (1997) provide a detailed description and explanation of the different regimes associates with the problem of a circular cylinder in uniform flow, which we shall now summarize. In the case of the flow past a cylinder without disturbances (such as free-stream turbulence, surface roughness, end effects, wall blockage, *etc.*), the Reynolds number based on cylinder diameter and free-stream velocity, $Re_D = U_0 D/\nu$, is the only governing parameter, and hence is used to delimit the various flow regimes. As summarized in Table 1.1, the following regimes are observed

1. laminar steady regime for $Re_D$ up to around 200 (Zdravkovisch takes 180-200, and Williamson 140-194);

2. transition to turbulence in the wake for $Re_D$ between around 200 and 400 (Zdravkovisch takes 180-200 and 350-400, while Williamson's lower bound is 190-260);

Table 1.1: Flow regimes for a circular cylinder in uniform flow, from Williamson (1996) and Zdravkovich (1997). The Reynolds number is based on cylinder diameter and free-stream velocity; ranges are approximative; k denotes $10^3$ and M denotes $10^6$.

| **Regime** | **Sub-Regime** | **Reynolds Number Range** |
|---|---|---|
| Laminar | Creeping Flow (No Separation) | 0 → 4-5 |
| | Steady Separation (Closed Wake) | 4-5 → 30-49 |
| | Periodic Shedding | 30-49 → 180-200 |
| Transition in Wake | Far-Wake Transition (Regular) | 180-200 → 220-260 |
| | Wake Transition (Irregular) | 250 → 400 |
| Transition in Shear Layer (Sub-Critical) | Undulations in Shear Layer | 400 → 1,000 |
| | Transition Waves Roll Up | 1k-2k → 20k-40k |
| | Turbulence in Shear Layers | 20k-40k → 100k-200k |
| Transition in Boundary Layer | Pre-Critical | 100k-200k → 300k-340k |
| | One-Bubble | 300k-340k → 380k-400k |
| | Two-Bubble | 380k-400k → 500k-1M |
| | Super-Critical | 500k-1M → 3.4M-6M |
| | Post-Critical | 3.4M-6M → *unknown* |
| Turbulent | Turbulent Onset at Stagnation | *unknown* |

3. transition in the shear layers for $Re_D$ between around 1,000 and $200 \times 10^3$;

4. transition in the boundary layer for $Re_D$ above around $200 \times 10^3$.

The laminar state can be sub-divided into three regimes. Below a Reynolds number of 5, creeping flow occurs where there is no separation; it is as if the flow was inviscid, the streamlines in front of the cylinder being symmetric with respect to the ones on the back. As the Reynolds number increases, a closed wake attached to the back of the cylinder appears; the flow is separated but has a steady symmetric wake, and the free-shear layers resulting from the separation meet at the confluence point that demarcates the end of the wake. When the value of $Re_D$ reaches the region between 50 and 200, an oscillation of the shear layers starting at the confluence point is observed, which gives birth to a staggered array of laminar vortex shedding, the *Kármán vortex street*, as first observed by Bénard (1908). The frequency of the shed-

ding is characterized by the Strouhal number (also called non-dimensional frequency), $St = fU_0/D$ where $f$ is the frequency, $U_0$ the free-stream velocity, and $D$ the cylinder diameter, named after Vincenc Strouhal who studied the humming of telegraph wires in 1878 (this name having been proposed by Bénard (1926)).

Above a Reynolds numbers of 200, transition to turbulence starts taking place in the far wake, and moves closer and closer to the cylinder back as the Reynolds number further increases. From Reynolds number of around 220 on, there is a change in shedding frequency and the transition to turbulence occurs close to the region of vortex formation near the back of the cylinder.

Transition in the free shear layers, that develop from the boundary layer separation on each side of the obstacle, takes place for Reynolds numbers between around 350 and 200,000. Following the suggestion by Wieselsberger (1921), this regime is called *sub-critical* because it precedes the steep decrease in drag coefficient observed when the boundary layer transitions. From Reynolds numbers of 350 to around 2,000, transition waves appear as undulations of the free shear layers, after which transition waves roll up into discrete vortices along the free shear layers which then turn turbulent. Burst to turbulence in the free shear layers then occurs for Reynolds numbers above 10,000 to 20,000, the shear layers rolling up into alternative vortices of positive and negative vorticity. As $Re_D$ further increases, and up to 100,000-200,000, the transition in the shear layer moves closer and closer to the cylinder, eventually taking place very close to the rear of the cylinder.

Further increase in the Reynolds number above 100,000 results in the onset of transition taking place along the separation lines, which is accompanied by a drop in the drag coefficient due to a delay in vortex formation. A sudden decrease in drag coefficient and increase in vortex shedding frequency is followed by the one-bubble regime for $Re_D$ between $300 \times 10^3$ and $400 \times 10^3$, in which the free shear layers reattach to the cylinder surface and define a separation bubble. Another discontinuous fall in the drag coefficient and jump in the shedding frequency is followed by the formation

of a second separation bubble, in what is called the two-bubble regime which takes place for $Re_D$ between around $400 \times 10^3$ and $0.5 \times 10^6$. In the subsequent super-critical regime ($Re_D$ between $500 \times 10^3$ and $4 \times 10^6$), periodic vortex shedding is prevented by irregularly separation lines caused by the disruption and fragmentation of the separation bubbles. Finally, when the Reynolds number exceeds $3.4 \times 10^6$, the boundary layer transitions before separation and the periodic vortex shedding reappears as observed by Roshko (1961); this regime is called post-critical or trans-critical.

There certainly exists a Reynolds number above which the flow is turbulent from the beginning of the boundary layer, but this phenomena has been rarely and inconsistently observed, due to the difficulty of reaching such high-velocity flows experimentally and of simulating them numerically.

### Sub-Critical Regime at Reynolds Number 3900

As indicated earlier, the Reynolds number for the study of a stationary cylinder has been set to $Re_D = 3900$, which corresponds to the sub-critical flow regime. We are interested in the transition to turbulence that takes place in the shear layers, the formation of statistically periodic vortex shedding, and the ability of turbulence models to properly capture the flow structures, average and instantaneous. In this section we shall describe previous numerical studies of this problem and some of the significant findings. Table 1.2 gives a summary of the main numerical studies considered here for comparison.

The detailed experimental measurements of the mean flow in the wake by Lourenco & Shih (1993) and by Ong & Wallace (1996) at $Re_D = 3900$ motivated the numerical study at this Reynolds number by many researchers. Parviz Moin and collaborators of the Center for Turbulence Research at Stanford University undertook a systematic numerical study of the flow at this Reynolds number, including a Direct Numerical

Table 1.2: Main numerical studies considered for comparison with the present research, all of them simulating a stationary cylinder in uniform flow at $Re_D = 3900$. Note: all the LES Smagorinsky use van Driest damping; incomp. $\equiv$ incompressible, comp. $\equiv$ compressible, FD $\equiv$ finite differences, FE $\equiv$ finite element, FV $\equiv$ finite volume, SP $\equiv$ spectral.

| **Reference** | **Type** | **Solver** |
|---|---|---|
| Tremblay *et al.* (2000) | DNS | incomp., FV |
| Ma *et al.* (2000) | DNS<br>LES Smagorinsky<br>($C_S = 0.032$ and 0.196) | incomp.,<br>SP |
| Beaudan (1994) | LES no model<br>LES dynamic Germano<br>LES Smagorinsky | comp.,<br>FD |
| Mittal (1996) and (1997) | LES dynamic localization | incomp., FD |
| Kravchenko & Moin (2000) | LES dynamic Germano | incomp., FE |
| Fröhlich *et al.* (1998) | LES Smagorinsky<br>($C_S = 0.1$) | incomp., FV |
| Breuer (1998) | LES no model<br>LES Smagorinsky ($C_S = 0.1$)<br>LES dynamic Germano | incomp.,<br>FD |
| Franke & Frank (2002) | LES Yoshisawa<br>(Smagorinsky type $C_S = 0.1$) | comp.,<br>FV |

Simulation (DNS) and a series of Large Eddy Simulations (LES), all using a span length of $\pi$ diameters (see Beaudan (1994), Mittal (1996), Mittal & Moin (1997) Kravchenko & Moin (2000)).

Kravchenko & Moin (2000) performed incompressible Large Eddy Simulations with the dynamic subgrid-scale model by Germano *et al.* (1991). They showed that if the separating shear layers are not resolved properly, the mean separation length will be underestimated, while "inadequate grid resolution can cause early transition in the shear layers separating from the cylinder which leads to inaccurate predictions of the near-wake flow statistics". They also found that the differences in mean velocity profile with and without subgrid-scalde modeling were insignificant, which was

also observed by Beaudan (1994) and Breuer (1998). This suggests that the small scale structures have little influence on the average flow quantities, which can then be obtained relatively accurately with modest computational effort through the use Unsteady Reynolds-Averaged Navier-Stokes simulations with simple algebraic turbulence models, a fact which is confirmed in this study.

Ma *et al.* (2000) carried out a DNS and a LES of the incompressible Navier-Stokes equations using a spectral finite element method. They studied the flow at different Reynolds numbers, including 500, 1000, 3900, and 5000, and gave a detailed analysis at 3900. The use of different span lengths ($\pi D/2$, $\pi D$, $3\pi D/2$, $2\pi D$) with constant resolution (cell span) showed that a span length of $\pi D$ is appropriate; this value was adopted in this study and was also chosen by Franke & Frank (2002), Breuer (1998), Kravchenko & Moin (2000), Fröhlich *et al.* (1998). They also noted that the structures become less and less wide in the third direction as the Reynolds number increases, which suggests that the higher the Reynolds number the smaller the span of the computational domain needs to be.

Their simulations unveil the existence of two different states of the very near wake (*i.e.* less than three diameters downstream of the cylinder), which depend on the span length and spanwise resolution of the computational domain: "two converged states, distinctly different, were obtained in the very near wake [...] but then converge downstream. This reflects the dynamics of the flow, which is governed by the shear layers in the very near wake which are quite sensitive to disturbances, and of the vortex shedding in the region downstream which is more robust." They even showed that both mean and root-mean-square (r.m.s.) velocity profiles were obtained accurately with the use of only two modes in the span direction without a subgrid-scale model, which further confirms the robustness of the wake and hence allows us to expect good results in the wake even with simple URANS models.

Finally Ma *et al.* (2000) conclude that "the span length is very important in determining the r.m.s. values in the very near wake and correspondingly the mean

velocity profiles" since "it appears that excessive dissipation due either to the subfilter model or the discretization can suppress significantly the small-scale fluctuations, altering greatly the inertial range" of the near wake spectrum. The present study attempts to verify this statement.

Franke & Frank (2002) used a compressible, cell-centered, finite volume solver to perform a LES with the subgrid-scale model by Yoshizawa (1986). Their domain span is also $\pi D$ and the flow Mach number is 0.2. Through a comparison between results of LES reported in the literature, they concluded that the differences observed in mean quantities (mean drag coefficient, mean back pressure, mean separation angle, Strouhal number) can be attributed, primarily, to the variation in the number of averaging periods employed, and that at least 200 non-dimensional averaging periods ($fD/U_0$) are necessary to obtain reliable mean quantities from LES. Also they explain the differences between the DNS results of Ma *et al.* (2000) and those of Tremblay *et al.* (2000) by the difference in boundary conditions in the normal direction: Ma used zero gradient at the top and bottom of the domain (located nine diameters from the cylinder center) which represents flow between two mirrored cylinders; in Tremblay the simulation corresponds to the flow between two cylinders translated one from the other since they use periodic boundary conditions twenty diameters away from the cylinder. This led them to the conclusion that "the flow around a circular cylinder at $Re_D = 3900$ is very sensitive to the boundary conditions, the cylinder span and small disturbances, caused by insufficient resolution and/or increased viscosity. This is in accordance with experimental results, which are known to be very sensitive to aspect ratio, blockage effect, end conditions, turbulence level, etc." [Franke & Frank (2002)].

It is interesting to note that Mittal (1996) and Mittal & Moin (1997) use farfield boundary conditions at $y/D = \pm 10$, which results in an acceleration of the flow at the edge of the wake, and is close to the effect observed in the DNS by Ma *et al.* (2000). Thus Mittal decided to enlarge the domain to $y/D = \pm 25$ for his LES. In our

study, the domain height was chosen to be $y/D = \pm 20$, and hence our results should be close to those of Mittal, and be subjected to negligible blockage effects.

The term blockage effects refers to the influence of the finite height of the computational domain on the simulation results, or of the finite height of the test section in experiments. Anagnostopoulos and collaborators (Anagnostopoulos *et al.* (1996) and Anagnostopoulos & Minear (2004)) studied the effect of the domain height on the two-dimensional flow past a circular cylinder in laminar regime. They observed that "the blockage alters the flow field, in such a way that the flow pattern obtained for an increased blockage corresponds to that occuring for a [lower Strouhal number] at unblocked conditions. [...] The higher blockage acts to [...] increase the drag coefficient". Their conclusion is that "blockage effect is almost negligible for blockages [i.e. ratio of cylinder diameter to domain height] lower than 20%", or equivalently for a domain height larger than five diameters.

### 1.2.2 Oscillating Cylinder

While there are many publication on oscillating cylinder flow and vortex induced vibrations, few of them are of numerical nature, and to our knowledge none at, or close to, the Reynolds number $R_D = 3600$. This section, which does not intend to be exhaustive, will introduce some of the characteristics of this type of flow and results of interest published in the literature.

Certainly the most remarkable feature of the problem involving a cylinder oscillating transversely in a uniform stream is the *lock-in* phenomenon: when the cylinder oscillates at a frequency close to the natural vortex shedding frequency of the stationary cylinder in the same flow, the frequency of vortex shedding locks-in to the natural shedding frequency, independently of the motion frequency and amplitude. As in simple oscillators, lock-in can occur at harmonics of the natural frequency; thus the term *primary lock-in* refers to the lock-in that occurs at an oscillating frequency

that is close to the natural shedding frequency of the stationary cylinder, while secondary lock-in takes place at half the cylinder frequency, and tertiary lock-in at a third.

A way of describing lock-in is given by Blackburn & Henderson (1999) who writes that "in forced oscillation studies, vortex shedding is entrained by the cylinder motion, hence the vortex shedding frequency changes to match the cylinder oscillation frequency".

This was observed by Bishop & Hassan (1964), who were among the first to investigate the motion of a circular cylinder perpendicularly to a uniform stream. They measured lift and drag forces on a horizontal cylinder driven vertically in a water channel, in order to find out how the forces on the cylinder are influenced by its forced oscillations. They observed lock-in which they interpreted as a peak, or resonance, at forcing frequency slightly below the natural shedding frequency, and made the analogy with the response of a simple oscillator to forced harmonic vibrations.

For Williamson & Roshko (1988), lock-in "occurs when the trajectory wavelength is comparable with the distance a non-oscillating cylinder travels through the fluid in one cycle of shedding [in vortex-induced vibrations]. In the fundamental lock-in region, the acceleration phase of the body motion at the start of each cycle has the effect of rolling-up both of the separating shear layers into a fresh pair of vortices. The continuously accelerating/decelerating body thereby sheds four regions of vorticity each cycle."

The second most widely studied property of the flow from an oscillating cylinder in free-stream was also observed by Bishop & Hassan (1964). When the lift force drops sharply, the phase difference between the lift signal and the forcing motion changes abruptly (this is referred to as *phase switch* or *phase shift*), while the location of this phase change depends on whether the frequency is being increased or decreased

(*hysteresis*).

Bishop & Hassan (1964) found evidence of hysteresis depending whether the forcing frequency was increased or decreased, with hysteresis bound by two frequencies $f_1$ and $f_2$ (whose values depend on the inflow Reynolds number and oscillation amplitude); when the frequency is above $f_2$, negative value of phase occurs, which correspond to negative energy, while for frequency values below $f_1$ the phase is around 170° (positive energy). When the frequency is decreasing, the phase jumps from 90° to 180°, whereas when it is increasing, the phase jumps from 170° to 180°. Both Zdravkovich (1982) and Öngören & Rockwell (1988) also demonstrated the existence of a change in the timing of vortex shedding on either side of the phase jump.

Williamson & Roshko (1988), who carried out experiments in a towing water tank, assert that "an abrupt change in the cylinder force can only be due to an abrupt change in the vortex force, *i.e.* to a sharp change in the dynamics of the shed vorticity." They address the question of "why does the vortex formation change its character through synchronization, and why does it change so suddenly at a critical wavelength?". Through a thorough investigation at many oscillating frequencies and amplitudes, they outlined the different regions of vortex synchronization in the $(\lambda/D\,,\,A/D)$ plane, $\lambda$ being the wavelength of corresponding sinewave trajectory of forced oscillation, and $A$ amplitude of oscillations. Most of the research is done in what Williamson & Roshko (1988) call the 2S region where fundamental lock-in occurs and one vortex is shed per half cycle, as in the natural Kármán street observed in the static cylinder in uniform flow. The reader is referred to the paper by Williamson & Roshko (1988) for a detailed discussion of the different modes.

They associate the phase switch to a jump from what they call the 2S mode — corresponding to the classical Kármán street mode in which two vortices are shed per cycle — to what they refer to as the 2P mode in which two vortex pairs are shed per cycle. For Williamson & Roshko (1988), "the vortices in the wake are not simply the result of one vortex shedding each half cycle, [...] but rather the wake involves

the roll up of four separate vortices each cycle. Below the critical trajectory size, a pair of like-sign vortices amalgamates in each half cycle, whereas above the critical condition the four vortices from each cycle organize themselves into two vortex pairs convecting away from the wake centerline."

However, Bishop & Hassan (1964) present no visualization associated with phase change, and Öngören & Rockwell (1988) as well as Den Hartog (1934, reproduced in Zdravkovich (1982)) observed the phase shift but no change in shedding mode, the shedding being always of Kármán-type. Furthermore, the phase shift is hard to observe and requires highly accurate measurement techniques, or simulations with low dissipative numerical schemes and highly accurate models, which may explain why it has never been observed in numerical simulations, to the author's knowledge. The existence of two distinct modes of vortex shedding that explain the phase shift remains an open question, and requires further investigation.

Den Hartog attributes the phase shift to a change in sign of the mechanical energy transfer from the flow to the cylinder, which coincides with the explanation of Blackburn & Henderson (1999) who studied a single oscillating amplitude, $A/D = 0.25$, over a range of frequencies near the vortex shedding frequency of the corresponding fixed cylinder, and concluded that "the phase-switching is associated with a change in sign of the mechanical energy transfer between the cylinder and the flow. [...] Discontinuous switch in phase of vortex shedding results from the outcome of a competition between two vorticity production mechanisms: the pressure gradient and the motion-induced vorticity production on the basal surface".

Stansby (1976) makes use of a low turbulence (0.25% intensity) wind tunnel and hot wire anemometry to study the transverse oscillations, with varying amplitudes $A/D$ between 0.01 and 0.48, of a circular cylinder with end plates at $Re_D = 3600$. He observed a phase angle jump by 180° at values of frequency ratio (of oscillatory motion to natural shedding frequency) which decreased with increasing amplitude. At $Re_D = 3600$ and $A/D = 0.25$, the value of the frequency ratio at the phase switch

is 0.86, which is close to the lower bound given by Bishop & Hassan (1964). This shift is accompanied by a change in wake width from a value larger than the width for a fixed cylinder (for frequencies lower than the one at which switch occurs) to a value smaller (for frequencies above the switch one). He also found that the "vortex shedding frequency locked on to the cylinder frequency and to submultiples of the cylinder frequency, and the lock-in range of motion frequencies depends on motion amplitude and Reynolds number".

Through a series of experiments in which a cylinder is towed in a still-liquid tank, Tanida *et al.* (1973) obtained results for a cylinder oscillating transversely at $Re_D = 80$ and 4,000, the Strouhal number of the oscillations being varied between 0 and 0.35. "When the oscillating frequency is either small or large enough, or with the frequency detrained more than 35% away from the Strouhal frequency, the vortex shedding occurs at the natural Strouhal frequency irrespectively of the oscillation, and the two sets of fluctuating forces are superposed upon each other. As the driving frequency approaches the Strouhal frequency, however, the system is synchronized to oscillate at the forcing frequency, and vortices are shed with frequency [ratio of oscillating to natural shedding frequency] of 1. The synchronization occurs over a finite frequency range, in which (a) the lift force oscillates regularly with fairly constant amplitude and takes a maximum value at around the center of the synchronization range, being accompanied by a sudden phase lag, and (b) the mean drag force also takes a maximum value at around the center of the range".

An interesting question that arises is whether the vortex-induced vibration phenomenon can be studied via the analysis of forced oscillations. According to Bearman (1984), "for a freely suspended bluff body oscillating at a steady amplitude, it can be assumed that if the same body is forced to oscillate at a similar amplitude ratio, reduced velocity, and Reynolds number, then the flow patterns will be identical. This bold statement presumes that the precise previous history of the motion is unimportant. The available experimental evidence suggests that free and forced-vibration

flows are the same." However, the present author agrees with Blackburn & Henderson (1999) who oppose this view and state that "entrainment behavior in vortex-induced vibration of flexible or flexibly mounted circular cylinders differs from that for forced oscillation. The primary reason is that a wider range of system dynamics is available in vortex-induced vibration, where the fluid-structure coupling can occur in both directions, as opposed to forced oscillation experiments, where the fluid motion is coupled to the body motion but not vice versa."

Since, to the knowledge of the author, no numerical simulations of circular cylinder oscillating transversely at a Reynolds numbers around 3600 are have been published to date, for the present study comparison will be made with the experimental results by Stansby (1976) at $Re_D = 3600$, and by Tanida *et al.* (1973) at $Re_D = 4000$.

## 1.3 Scope of the Research

The present research is focused around two sets of numerical simulations. The first is the simulation of a circular cylinder in uniform flow at $Re_D = 3900$, and the observation of the vortex shedding and associated velocity, density, pressure, and vorticity fields, as well as the resulting mean drag coefficient, Strouhal number, pressure and skin friction coefficients around the surface, back pressure coefficient, and velocity profiles along in the wake. The second problem is that of a circular cylinder oscillating transversely in a uniform stream at $Re_D = 3600$, for which we wish to observe the primary lock-in and the phase shift.

For both problems, a comprehensive study of mean fields, which are of particular interest to design, and of detailed instantaneous fields and fluctuating quantities, which are of major importance to fundamental research in fluid dynamics and turbulence modeling, were done, with particular attention to the separation process.

A thorough validation of the numerical code and discretization methods was car-

ried out, as well as the turbulence models and subgrid-scale models considered, namely

- one-equation Spalart-Allmaras model for the solution of Unsteady Reynolds-Averaged Navier-Stokes (URANS) equations [Spalart & Allmaras (1994)];
- two-equation $k$-$\tau$ model by Speziale *et al.* (1992) for URANS simulations;
- Large Eddy Simulation (LES) with the Smagorinsky subgrid-scale and Smagorinsky constant set to $C_S = 0.065$;
- Very Large Eddy Simulation with the adaptive $k$-$\tau$ model proposed by Magagnato & Gabi (2002).

This will allow for comparison of the accuracy and effectiveness (computational cost relative to accuracy) of the above-mentioned turbulence modeling techniques for the compressible simulation of vortex shedding phenomena. A key contribution of this work is a comparison of results obtained with *the same numerical procedure, discretization algorithms, and artificial dissipation* but different turbulence modeling techniques in order to properly differentiate between errors due to numerical and to modeling aspects, which is particularly difficult in LES in which the grid determines both the discretization of the governing equations and the cut between the resolution of the equations and the sub-grid scale modeling of unresolved scales. Thus particular attention is given to the generation of the computational grid, to the selection of an appropriate time step, and to the choice of discretization and numerical dissipation schemes.

Furthermore, the commercial CFD package Fluent was used to simulate the flow around the stationary cylinder, in an attempt to obtain another base for comparison for the research code SPARC (Structured PArallel Research Code) which is used for the present study.

In order to accomplish the objectives of this research, the compressible dynamic mixed model was implemented into the computational research code, and a procedure

for setting up the cylinder rigid-body motion was devised. Finally, a framework for the numerical study of a flapping airfoil in the turbulent flow regime at $Re_D = 40,000$, including motion and grid, was put in place.

## 1.4 Thesis Outline

A general introduction to the problem of turbulence modeling as applied to the flow around a circular cylinder, as well as an overview of the previous works related to the problem and to the particular investigation carried out in this work has been presented in this chapter.

The next chapter is devoted to three main items related to the theoretical background of this study. First, a general introduction to turbulence and its simulation is given, followed by the governing equations of compressible, unsteady, viscous flow. Then, a detailed description of the turbulence modeling techniques that were used is presented, with emphasis on the features of each model in the hope that the reader will be able to better comprehend the reasons for the success, or lack thereof, of each model in the simulation of the vortex shedding behind circular cylinders in sub-critical regime. Finally, the computational code and numerical schemes are described, with a justification of their selection.

Detailed results of the simulations of the flow around a stationary circular cylinder at $Re_D = 3900$ and those of the transverse oscillation of a cylinder in a uniform stream at $Re_D = 3600$ are presented in Chapter 3.

The last chapter states the conclusions of this investigation on the comparative assessment of the turbulence modeling techniques considered, and describes some of the further work that is in progress, as well as questions that emerged from the results presented here and that shall be the subject of future studies.

# Chapter 2

# Numerical Simulation of Turbulent Flows

The purpose of this chapter is to provide a brief description of turbulence phenomena and to introduce the governing equations that are solved by the numerical code. The turbulence modeling techniques that are used for this research are presented in detail so that their applicability, or lack thereof, to the vortex shedding past a cylinder will be better understood. Finally, the computational code and numerical schemes employed are presented.

## 2.1 About Turbulence

While the equations governing the motion of a Newtonian fluid, and hence of turbulence, are known since the works by Navier and by Stokes in 1823 and 1845, respectively, they have no exact analytical solution for flows of practical interest, and are numerically challenging because of their highly non-linear character. Even though turbulent flows have been extensively investigated for more than a century, turbulence still remains "the most important unsolved problem of classical physics", as

reportedly phrased by Richard Feynman [Moin & Kim (1997)].

How can order turn into chaos? How can one start from a fully determined problem, governed by well-known equations, and arrive to an unpredictable and unrepeatable solution, as is often the case in complex turbulence studies? As Lorenz (1993) points out, "sometimes a distinction is made between "chaos" and "complexity", with the former term referring to irregularity in time, and the latter implying irregularity in space." These two types of irregularities are often found together in turbulent flows.

The theory of chaos is concerned with the description of the behavior of nonlinear dynamical systems. The definition of what the word *chaos* refers to and implies is well beyond the scope of this thesis, but I shall venture to give a few details in order to make my point. The main characteristic of a chaotic system is its sensitivity to initial and boundary conditions, what is commonly called the butterfly effect. The meteorologist Edward Lorenz (1993) asked "does the flap of a butterfly's wings in Brazil set off a tornado in Texas?" and concluded that the atmosphere is overwhelmingly unstable because: (i) small perturbations in the coarser structure of the weather pattern [...] tend to double in about three days; (ii) small perturbations in the finer structure [...] tend to grow much more rapidly, doubling in hours or less; and (iii) perturbations in the finer structure, having attained appreciable size, tend to induce errors in the coarser structure.

Thus, the behavior of the weather, and also the behavior of turbulent flows, appears to be random when it is in fact deterministic ("later states evolve from earlier ones according to a fixed law" [*id.*]). And for Lorenz to conclude that "today's errors in weather forecasting [...] arise mainly from our failure to observe even the coarser structure with near completeness, our somewhat incomplete knowledge of the governing physical principles, and the inevitable approximations which must be introduced in formulating these principles as procedures which the human brain or the computer can carry out".

Back to our parallel with fluid dynamics: the equations governing the motion of turbulent flows are deterministic but form a nonlinear dynamical system. Thus, it is the belief of the author that the un-repeatability (impossibility of finding exactly the same properties in a repetition of the same setup) and hence unpredictability (impossibility of predicting the end state) of experiments and computer simulations is due to the high sensitivity of the flow to errors in the setup and in experimental measurements, for the former, and to truncation errors in floating point computations for the later. One should strive to reduce the experimental and numerical errors as much as possible, in order to be able to see the larger picture and coherence of turbulent flows.

### 2.1.1 Characterization of Turbulence

Because of its intrinsic complexity, turbulence has no precise definition. Hinze (1975) defines turbulent motion as "an irregular condition of flow in which the various quantities show a random variation with time and space coordinates so that statistically distinct average values can be discerned", while Peter Bradshaw (1971) underlines its main characteristics when stating that "turbulence is a three dimensional time dependent motion in which vortex stretching causes velocity fluctuations to spread to all wavelengths between a minimum determined by viscous forces and a maximum determined by the boundary conditions. It is the usual state of fluid motion except at low Reynolds numbers".

In spite of the lack of a formal definition, turbulence is generally agreed to having the following characteristics, as partly listed by Tennekes & Lumley (1972) in their introduction,

- randomness in both space and time, meaning that the value of the variables are not the same "every time the experiment is repeated under the same set of conditions" [Pope (2000)];

- diffusivity, *i.e.* the spreading of fluctuations through the fluid, which is responsible for rapid mixing and large transport of momentum, heat, and mass;
- three-dimensionality and rotationality: high levels of fluctuating vorticity mainly maintained by vortex stretching, which requires the flow to be three-dimensional;
- dissipation, which results from the increase in internal energy at the expense of kinetic energy through viscous shear stresses;
- and a continuous and broad range of length scales: turbulent eddies range in size from the width of the flow down to the smallest dissipative scales, the Kolmogorov scales.

### 2.1.2 Governing Equations of Fluid Flow

The purpose of this section is to express the equations governing the flow of a fluid in a form appropriate for the understanding and derivation of the equations, including turbulence models, that are solved during a numerical simulation. For a complete derivation of the equations, the reader is referred to the classical textbooks by Anderson (2003) and White (1991).

Most of the fluids of engineering interest, such as air and water, are Newtonian fluids. A Newtonian, or linear, fluid is defined as a substance for which the velocity gradient is proportional to the applied shear, which in cartesian coordinates defines the total stress tensor, $\sigma'_{ij}$, as

$$\sigma'_{ij} \equiv -p\delta_{ij} + \delta_{ij}\lambda\frac{\partial u_i}{\partial x_i} + \mu\left(\frac{\partial u_i}{\partial x_j} + \frac{\partial u_j}{\partial x_i}\right) \tag{2.1}$$

where $p$ is the static — *i.e.* thermodynamic — pressure, $\lambda$ is the second coefficient of viscosity — also called coefficient of bulk viscosity — which is associated only with volume expansion, $\mu$ is the dynamic viscosity of the fluid, $x_i$ is $i^{\text{th}}$ position coordinate,

and $u_i$ is the velocity component in the $i^{th}$ direction. The Kronecker delta function is such that

$$\delta_{ij} \equiv \begin{cases} 1 \text{ if } i = j \\ 0 \text{ if } i \neq j \end{cases}$$

and ensures that the deformation stress reduces to the hydrostatic pressure, $p$, when the strain rates $(\partial u_i/\partial x_j + \partial u_i/\partial x_i)$ vanish.

The second viscosity coefficient is a somewhat controversial term, and the interested reader should refer to Landau & Lifschitz (1959). In this work, Stokes' hypothesis is adopted, such that

$$\lambda + \frac{2}{3}\mu = 0$$

and hence equation (2.1) reduces to

$$\sigma'_{ij} = -p\delta_{ij} - \frac{2}{3}\mu\frac{\partial u_i}{\partial x_i}\delta_{ij} + \mu\left(\frac{\partial u_i}{\partial x_j} + \frac{\partial u_j}{\partial x_i}\right). \tag{2.2}$$

The molecular viscosity is assumed to vary with temperature according to the kinetic theory of Sutherland (1893), which is generally more accurate than the power law, such that

$$\frac{\mu}{\mu_0} = \left(\frac{T}{T_0}\right)^{3/2}\frac{T_0 + S}{T + S} \tag{2.3}$$

where $\mu_0$ and $T_0$ are reference values, and $S = 110.4\text{K}$ is the effective temperature of the gas called Sutherland constant. Equivalently,

$$\mu = \frac{bT^{3/2}}{T + S} \tag{2.4}$$

for $b = 1.458 \times 10^{-6}\text{kg/m}\cdot\text{s}\cdot\sqrt{\text{K}}$. A thorough discussion of the coefficient of viscosity can be found in White (1991).

The motion of a Newtonian fluid is governed by the conservation of mass, momen-

tum and energy. For a compressible flow, the conservation of mass — also referred to as the continuity equation — can be written as

$$\frac{\partial \rho}{\partial t} + \frac{\partial}{\partial x_i}\left(\rho u_i\right) = 0. \tag{2.5}$$

The momentum equation is a vector equation and thus forms a set of three scalar equations, which are commonly known as the Navier-Stokes equations in reference to Navier and Stokes who derived them independently in 1823 and 1845 respectively. In the absence of gravity or other body forces, and using Stokes' hypothesis, these equations read

$$\frac{\partial \left(\rho u_i\right)}{\partial t} + \frac{\partial \left(\rho u_i u_j\right)}{\partial x_j} = -\frac{\partial p}{\partial x_i} + \frac{\partial \sigma_{ij}}{\partial x_j} \quad \text{for } i \in \{1,2,3\} \tag{2.6}$$

where $\sigma_{ij}$ is the viscous stress tensor

$$\sigma_{ij} \equiv \mu\left(\frac{\partial u_i}{\partial x_j} + \frac{\partial u_j}{\partial x_i}\right) - \frac{2}{3}\mu\frac{\partial u_k}{\partial x_k}\delta_{ij}. \tag{2.7}$$

Alternatively, by using the conservation of mass, equation (2.6) can be written as

$$\rho\left(\frac{\partial u_i}{\partial t} + u_j\frac{\partial u_i}{\partial x_j}\right) = -\frac{\partial p}{\partial x_i} + \frac{\partial \sigma_{ij}}{\partial x_j}. \tag{2.8}$$

Finally, the energy equation is derived from the first law of thermodynamics. For a calorically perfect gas — *i.e.* one with constant specific heats — in adiabatic flow, it can be expressed as

$$\frac{\partial \left(\rho c_v T\right)}{\partial t} + \frac{\partial \left(\rho u_i c_v T\right)}{\partial x_i} = -p\frac{\partial u_i}{\partial x_i} + \frac{\partial}{\partial x_i}\left(\kappa\frac{\partial T}{\partial x_i}\right) + \sigma_{ij}\frac{\partial u_i}{\partial x_j}$$

where $T$ is the static temperature, $c_v$ the specific heat at constant volume, and $\kappa$ the

thermal conductivity of the fluid. Thus

$$c_v \left[ \frac{\partial (\rho T)}{\partial t} + \frac{\partial (\rho u_i T)}{\partial x_i} \right] = -p \frac{\partial u_i}{\partial x_i} + \frac{\partial}{\partial x_i} \left( \kappa \frac{\partial T}{\partial x_i} \right) + \sigma_{ij} \frac{\partial u_i}{\partial x_j} \tag{2.9}$$

Equivalently, making use of the continuity relation the above equation can be written as

$$c_v \left[ \rho \frac{\partial (T)}{\partial t} + \rho u_i \frac{\partial (T)}{\partial x_i} \right] = -p \frac{\partial u_i}{\partial x_i} + \frac{\partial}{\partial x_i} \left( \kappa \frac{\partial T}{\partial x_i} \right) + \sigma_{ij} \frac{\partial u_i}{\partial x_j} \tag{2.10}$$

There are six unknowns in the system of five equations (2.5), (2.6), (2.9), namely the density, $\rho$, the pressure, $p$, the static temperature, $T$, and the three components of velocity, $u_i$. Hence, in compressible flow, an equation of state is necessary, for which we use the ideal gas law

$$p = \rho R T \tag{2.11}$$

in which $R$ is the specific gas constant, set to 287 kJ/kg·K for air.

In summary, the fluid flow of a compressible ideal gas is governed by the following equations

$$\begin{aligned}
&\frac{\partial \rho}{\partial t} + \frac{\partial (\rho u_i)}{\partial x_i} = 0 \\
&\frac{\partial (\rho u_i)}{\partial t} + \frac{\partial (\rho u_i u_j)}{\partial x_j} = -\frac{\partial p}{\partial x_i} + \frac{\partial \sigma_{ij}}{\partial x_j} \\
&c_v \left[ \frac{\partial (\rho T)}{\partial t} + \frac{\partial (\rho u_i T)}{\partial x_i} \right] = -p \frac{\partial u_i}{\partial x_i} + \frac{\partial}{\partial x_i} \left( \kappa \frac{\partial T}{\partial x_i} \right) + \sigma_{ij} \frac{\partial u_i}{\partial x_j} \\
&p = \rho R T.
\end{aligned}$$

Equations (2.5), (2.6), (2.9), and (2.11) form a closed system that can, in theory, be solved for the six unknowns: they contain all the physics of the flow, but there is no general analytical solution. Therefore, one has to make use of numerical methods to approximate the solution, which involve discretizing and linearizing the equations before finding a solution using tools of linear algebra. The computational research

code used for the present work, SPARC (Structured PArallel Research Code), is described in detail in section 2.5.

### 2.1.3 The Need for Turbulence Models

At this point in our discussion, a legitimate question to ask would be: if the exact equations governing fluid flow are known and if one can use linearization techniques to solve them, why do we need turbulence models? The main reason is the limitation in computational power: the discretized equations need to be solved at discrete points in the flow domain, and hence a large number of node points, or grid volumes depending on the solution technique, is necessary to achieve high levels of accuracy. As mentioned earlier, turbulence is characterized by a continuous range of characteristic scales, spatial and temporal, and thus one would need to solve the motion down to the smallest eddies, which is done in Direct Numerical Simulations (DNS). Hence the size of the grid elements needs to be very small, and a DNS requires computers with a large amount of memory and processing power. Even with the progress in technology and the decline of computer prices, many problems of practical interest cannot be solved through a DNS in an acceptable time, particularly when the flow Reynolds number is high since the computational cost of a three-dimensional simulation increases approximately with the cube of the Reynolds number.

Another important justification for the use of turbulence models, or more generally turbulence simulation techniques, is that while the governing equations contain all the physics of the flow, they are not readily discernible. In other words, because the equations are highly non-linear, one cannot easily predict how the flow behavior would be affected by a change in the conditions. For instance how would the flow respond to a small change in velocity, or to a small change in the entering air turbulence level? How would the boundary layer on a wing be modified by the presence of gusts? The process of deriving a turbulence model — neglecting certain terms with respect

to some others and certain effect to retain only the main aspects — together with the simplification that a turbulence model represents (particular true for algebraic models) carve out fundamental properties of the flow, such as its dissipativeness and diffusivity, and hence can sometimes teach us more than the exact equations.

The importance of turbulence models is not only confined to the prediction of flows; it resides also in their ability to provide an understanding of the fundamental physical phenomena involved. One is no longer satisfied with the observation and description of flows; one seeks to understand and encapsulate the physics of turbulent phenomena through the derivation and testing of models.

### 2.1.4 Flow Decomposition

It is customary, and convenient as will soon become clear, to decompose any quantity, $\phi(x_i, t)$, as

$$\phi(x_i, t) = \overline{\phi}(x_i, t) + \phi'(x_i, t) \tag{2.12}$$

In an Unsteady Reynolds Average Navier-Stokes (URANS) approach, where the flow equations are averaged over time, $\overline{\phi}(x_i, t)$ is the time average (mean) value and $\phi'(x_i, t)$ is the fluctuating component. In a Large Eddy Simulation, the fields are decomposed into a resolved component $\overline{\phi}(x_i, t)$ and a subgrid component $\phi'(x_i, t)$. Thus the overline operation can refer to either an averaging (temporal) in the case of a URANS, or a filtering (spatial) in the case of a LES.

Some important properties of any such decomposition are

$$\begin{aligned} \overline{\phi_1 + \phi_2} &= \overline{\phi_1} + \overline{\phi_2} \\ \overline{\frac{\partial \phi}{\partial x}} &= \frac{\partial \overline{\phi}}{\partial x} \\ \overline{\int \phi dx} &= \int \overline{\phi} dx \end{aligned} \tag{2.13}$$

By applying the over-line operator to both sides of the continuity equation (2.5) and simplifying using the properties (2.13), one gets the expression for the continuity equation of over-lined quantities, namely

$$\frac{\partial \overline{\rho}}{\partial t} + \frac{\partial \left(\overline{\rho u_i}\right)}{\partial x_i} = 0. \tag{2.14}$$

Similarly, applying the over-line operator to the momentum equation (2.6) yields, after appropriate simplification,

$$\frac{\partial}{\partial t}\left(\overline{\rho u_i}\right) + \frac{\partial}{\partial x_j}\left(\overline{\rho u_i u_j}\right) = -\frac{\partial \overline{p}}{\partial x_i} + \frac{\partial}{\partial x_j}\left[\mu\left(\frac{\partial \overline{u_i}}{\partial x_j} + \frac{\partial \overline{u_j}}{\partial x_i}\right) - \frac{2}{3}\mu\frac{\partial \overline{u_k}}{\partial x_k}\delta_{ij}\right]$$

which can be written as

$$\frac{\partial}{\partial t}\left(\overline{\rho u_i}\right) + \frac{\partial}{\partial x_j}\left(\overline{\rho u_i u_j}\right) = -\frac{\partial \overline{p}}{\partial x_i} + \frac{\partial \overline{\sigma_{ij}}}{\partial x_j} \tag{2.15}$$

with

$$\overline{\sigma_{ij}} = \mu\left(\frac{\partial \overline{u_i}}{\partial x_j} + \frac{\partial \overline{u_j}}{\partial x_i}\right) - \frac{2}{3}\mu\frac{\partial \overline{u_k}}{\partial x_k}\delta_{ij}. \tag{2.16}$$

The energy equation (2.9) is also recast in the form

$$c_v\left[\frac{\partial \left(\overline{\rho T}\right)}{\partial t} + \frac{\partial \left(\overline{\rho u_i T}\right)}{\partial x_i}\right] = -\overline{p\frac{\partial u_i}{\partial x_i}} + \frac{\partial}{\partial x_i}\overline{\left(\kappa\frac{\partial T}{\partial x_i}\right)} + \overline{\sigma_{ij}\frac{\partial u_i}{\partial x_j}}, \tag{2.17}$$

while the ideal gas law reads

$$\overline{p} = R\overline{\rho T}. \tag{2.18}$$

Equations (2.14), (2.15), (2.17), and (2.18) are valid for any averaging or filtering that decomposes the scalar $\phi$ into two components $\overline{\phi}$ and $\phi'$, and hence are the equations that are solved in most numerical techniques for fluid flows.

### 2.1.5 Favre Averaging and Favre Filtering

The modeling of turbulence started with incompressible flows, in which the model involves an equation for the velocity correlation $\overline{u_i u_j}$. When working with compressible flows, in order to avoid having to deal with triple correlations of the type $\overline{\rho u_i u_j}$, the common practice is to replace them by double correlations through the use of the density-weighted averaging procedure suggested by Alexandre Favre (1965) in which the density-weighted component, $\widetilde{\phi}$, of a variable $\phi$ is defined in such a way that

$$\overline{\rho}\tilde{\phi} = \overline{\rho\phi}, \tag{2.19}$$

where $\overline{\rho}$ is the density that is computed in the simulation. Hence, when working with the URANS equations, $\overline{\rho}$ is the mean density and we refer to the procedure as *Favre-averaging* with the use of ensemble averaging

$$\tilde{\phi}(x_i,t) \equiv \frac{1}{\overline{\rho}} \lim_{N\to\infty} \frac{1}{N} \sum_{n=1}^{N} \rho(x_i,\tau)\phi(x_i,\tau)d\tau \tag{2.20}$$

where $N$ is the number of measurement sets (realizations) for the same conditions, which is appropriate for experimental techniques but is rarely used in conjunction with numerical techniques since simulations are seldom run more than once. In the particular case where the flow is periodic with period $T$, the ensemble average is equivalent to a phase average, and

$$\tilde{\phi}(x_i,t) \equiv \frac{1}{\overline{\rho}\,2T} \int_{-T}^{T} \rho(x_i,\tau)\phi(x_i,\tau)d\tau. \tag{2.21}$$

In conjunction with LES, $\overline{\rho}$ is the resolved density, and the term *Favre-filtering* is employed with

$$\tilde{\phi}(x_i,t) \equiv \frac{1}{\overline{\rho}\,\mathcal{V}} \int\int\int_{\mathcal{V}} \rho(x_i,t)\phi(x_i,t)d\mathcal{V} \tag{2.22}$$

where the integral is carried out over a grid cell volume $\mathcal{V}$.

Let us introduce the fundamental property of Favre quantities (2.19) into the continuity equation (2.14) to get

$$\frac{\partial \overline{\rho}}{\partial t} + \frac{\partial \left(\overline{\rho}\, \widetilde{u}_i\right)}{\partial x_i} = 0. \tag{2.23}$$

The momentum equation (2.15) becomes

$$\frac{\partial}{\partial t}\left(\overline{\rho}\, \widetilde{u}_i\right) + \frac{\partial}{\partial x_j}\left(\overline{\rho}\, \widetilde{u_i u_j}\right) = -\frac{\partial \overline{p}}{\partial x_i} + \frac{\partial \overline{\sigma_{ij}}}{\partial x_j} \tag{2.24}$$

and since we wish to express as many terms as possible using Favre-averaged/filtered quantities, the above equation is transformed by first adding $\partial\left(\overline{\rho}\, \widetilde{u}_i\, \widetilde{u}_j\right)/\partial x_j$ to both sides as follows

$$\frac{\partial}{\partial t}\left(\overline{\rho}\, \widetilde{u}_i\right) + \frac{\partial}{\partial x_j}\left(\overline{\rho}\, \widetilde{u_i u_j} + \overline{\rho}\, \widetilde{u}_i\, \widetilde{u}_j\right) = -\frac{\partial \overline{p}}{\partial x_i} + \frac{\partial}{\partial x_j}\left(\overline{\sigma_{ij}} + \overline{\rho}\, \widetilde{u}_i\, \widetilde{u}_j\right),$$

or equivalently

$$\frac{\partial}{\partial t}\left(\overline{\rho}\, \widetilde{u}_i\right) + \frac{\partial}{\partial x_j}\left(\overline{\rho}\, \widetilde{u}_i\, \widetilde{u}_j\right) = -\frac{\partial \overline{p}}{\partial x_i} + \frac{\partial}{\partial x_j}\left(\overline{\sigma_{ij}} + \overline{\rho}\, \widetilde{u}_i\, \widetilde{u}_j - \overline{\rho}\, \widetilde{u_i u_j}\right),$$

and finally rearranging to get

$$\frac{\partial}{\partial t}\left(\overline{\rho}\, \widetilde{u}_i\right) + \frac{\partial}{\partial x_j}\left(\overline{\rho}\, \widetilde{u}_i\, \widetilde{u}_j\right) = -\frac{\partial \overline{p}}{\partial x_i} + \frac{\partial}{\partial x_j}\left[\overline{\sigma_{ij}} - \overline{\rho}\left(\widetilde{u_i u_j} - \widetilde{u}_i\, \widetilde{u}_j\right)\right],$$

which we write as

$$\frac{\partial}{\partial t}\left(\overline{\rho}\, \widetilde{u}_i\right) + \frac{\partial}{\partial x_j}\left(\overline{\rho}\, \widetilde{u}_i\, \widetilde{u}_j\right) = -\frac{\partial \overline{p}}{\partial x_i} + \frac{\partial}{\partial x_j}\left(\overline{\sigma_{ij}} - \tau_{ij}\right) \tag{2.25}$$

with

$$\tau_{ij} \equiv -\overline{\rho}\left(\widetilde{u_i u_j} - \widetilde{u}_i\, \widetilde{u}_j\right). \tag{2.26}$$

Finally, the energy equation and the ideal gas law are recast in the respective

forms

$$c_v \left[ \frac{\partial \left( \overline{\rho} \tilde{T} \right)}{\partial t} + \frac{\partial \left( \overline{\rho} \tilde{u}_i \tilde{T} \right)}{\partial x_i} \right] = -\overline{p \frac{\partial u_i}{\partial x_i}} + \frac{\partial}{\partial x_i} \overline{\left( \kappa \frac{\partial T}{\partial x_i} \right)} + \overline{\tau_{ij} \frac{\partial u_i}{\partial x_j}}, \tag{2.27}$$

and

$$\overline{p} = \overline{\rho} R \tilde{T}. \tag{2.28}$$

To summarize, in compressible flow simulations the Favre-averaged/filtered equations are solved, namely

$$\frac{\partial \overline{\rho}}{\partial t} + \frac{\partial}{\partial x_i} \left( \overline{\rho} \tilde{u}_i \right) = 0 \tag{2.29}$$

$$\frac{\partial}{\partial t} \left( \overline{\rho}\, \widetilde{u}_i \right) + \frac{\partial}{\partial x_j} \left( \overline{\rho}\, \widetilde{u}_i\, \widetilde{u}_j \right) = -\frac{\partial \overline{p}}{\partial x_i} + \frac{\partial}{\partial x_j} \left[ \overline{\sigma_{ij}} - \overline{\rho} \left( \widetilde{u_i u_j} - \widetilde{u}_i\, \widetilde{u}_j \right) \right] \tag{2.30}$$

$$c_v \left[ \frac{\partial \left( \overline{\rho} \tilde{T} \right)}{\partial t} + \frac{\partial \left( \overline{\rho} \tilde{u}_i \tilde{T} \right)}{\partial x_i} \right] = -\overline{p \frac{\partial u_i}{\partial x_i}} + \frac{\partial}{\partial x_i} \overline{\left( \kappa \frac{\partial T}{\partial x_i} \right)} + \overline{\tau_{ij} \frac{\partial u_i}{\partial x_j}}, \tag{2.31}$$

$$\overline{p} = \overline{\rho} R \tilde{T} \tag{2.32}$$

where the tilde denotes Favre-averaged quantities if the simulation is of URANS type, and Favre-filtered quantities when doing a LES.

In summary, we are simply replacing quantities such as $\overline{\rho u_i}$ and $\overline{\rho u_i u_j}$ by $\overline{\rho}\, \widetilde{u}_i$ and $\overline{\rho}\, \widetilde{u_i u_j}$, by making use of the Favre decomposition for velocity $u_i = \tilde{u}_i + u_i''$ and for temperature and $T = \tilde{T} + T''$, where the double primes denotes fluctuating components with respect to the density-averaged/filtered counterparts. Note that the equations obtained by introducing the Favre-averaging/filtering procedure represent an important simplification since the only new term compared to the equations for the instantaneous quantities is the so-called Favre-averaged/filtered Reynolds-stress tensor $-\overline{\rho u_i u_j} = -\overline{\rho}\, \widetilde{u_i u_j}$ which needs to be modeled.

### 2.1.6 Classification of Turbulence Modeling Techniques

How does one model the Reynolds stresses $-\overline{\rho u_i u_j} = -\overline{\rho}\,\widetilde{u_i u_j}$ ? Whether the modeling is applied to the whole computational domain, as in the URANS approach, or only represents certain scales of the flow, as in LES, one way is to use the turbulent (or eddy) viscosity concept according to which the Reynolds stresses are proportional to the rate of deformation and a parameter similar to the molecular viscosity, and then to employ an equation for the turbulent (or eddy) viscosity instead. Another method is to directly use a transport equation for the Reynolds stresses.

There are two main ways of classifying the methods for predicting turbulent flows. One can consider what physical quantity is being modeled, whether it is a the turbulent length scale, the turbulent viscosity, or the Reynolds stresses. Alternatively, the methods can be categorized according to which motions are solved for and which motions are modeled. In this second approach, there are six categories — some of which are illustrated in Figure 2.1 — according to Bardina *et al.* (1980), namely

- use of correlations to obtain quantities of interest, such as the friction factor as a function of the Reynolds number;
- use of integral equations;
- solution of a *one-point closure* which involves the use of the *Reynolds Averaged Navier-Stokes* (RANS) equations to solve for the mean quantities together with a turbulence model required for closure;
- solution of a *two-point closure* which involves the use of equations for the correlation of the velocity components (or their Fourier transform) at two points in the domain;
- *Large-Eddy Simulation* (LES) in which the larger scales of motion are solve and the smaller scales are modeled;

- *Direct Numerical Simulation* (DNS) in which all the turbulent motions are computed.

To this list one can add the Detached Eddy Simulation (DES) which treats near-wall regions in a URANS manner and regions far from the wall as in an LES, the Probability Density Function (PDF) which relies on the modeling of a transport equation for the probability density function of velocity for instance; and the Very Large Eddy Simulation which is similar to an LES except that the solved motions cover a smaller part of the energy spectrum and the subgrid modeling is of URANS type.

The following sections are devoted to explaining the turbulence modeling techniques that are used in the present study.

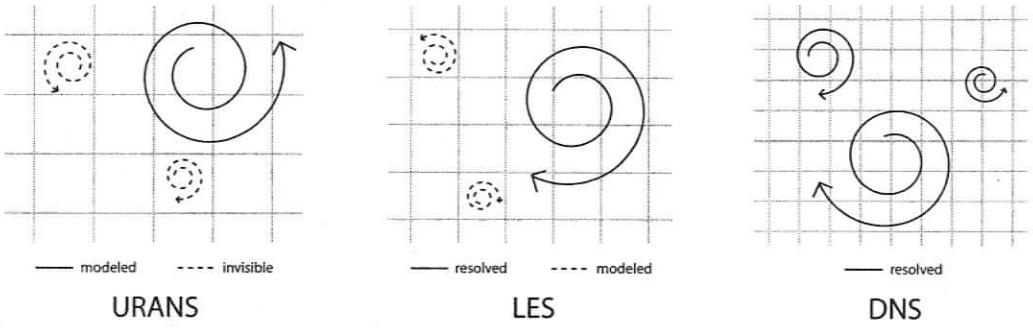


Figure 2.1: Illustration of the three main turbulence simulation techniques: in URANS all the turbulent scales are modeled and nothing accounts for the ones too small to be captured by the computational grid; in LES the subgrid scales (smaller than the characteristic size of the grid) are modeled while the large scales are resolved; in DNS the grid is small so as to resolve all the scales.

## 2.2 Turbulence Models for Reynolds-Averaged Navier-Stokes Equations

### 2.2.1 Principle

Single-point closure methods are certainly the most widely used framework for turbulence modeling. In the context of flow with large scale unsteadiness, they involve the solution of the the Unsteady Reynolds Averaged Navier-Stokes equations (URANS), which are derived below.

In 1894 Osborne Reynolds suggested the decomposition of the instantaneous flow quantities into a mean and a fluctuating component, the so-called *Reynolds decomposition*,

$$\phi(x_i,t) = \overline{\phi}(x_i,t) + \phi'(x_i,t) \tag{2.33}$$

which has a form similar to equation (2.12), but is defined in terms of the ensemble average

$$\overline{\phi}(x_i,t) = \lim_{N\to\infty} \frac{1}{N} \sum_{n=1}^{N} \phi_n(x_i,t) \tag{2.34}$$

for the mean component, $\phi'(x_i,t)$ being the fluctuating component. The number $N$ refers to the number of measurement sets for the same conditions, as in section 2.1.5. In the particular case where the flow is periodic, with period $T$, the ensemble average is equivalent to a phase average, and

$$\overline{\phi}(x_i,t) = \frac{1}{2T} \int_{-T}^{T} \phi(x_i,t)dt. \tag{2.35}$$

From the definition of the mean quantity,

$$\overline{\overline{\phi}} = \overline{\phi} \tag{2.36}$$

$$\overline{\phi'} = 0 \tag{2.37}$$

$$\widetilde{\phi''} = 0 \tag{2.38}$$

where the last equality can be derived by taking the Favre decomposition $\phi = \tilde{\phi} + \phi''$ and multiplying through by the density to get $\rho\phi = \rho\tilde{\phi} + \rho\phi''$, which by taking the average of both sides yields,

$$\overline{\rho\phi} = \overline{\rho\tilde{\phi}} + \overline{\rho\phi''}.$$

Since

$$\overline{\rho\tilde{\phi}} = \rho\frac{\overline{\rho\phi}}{\overline{\rho}} = \overline{\rho}\frac{\overline{\rho\phi}}{\overline{\rho}} = \overline{\rho}\tilde{\phi},$$

then

$$\overline{\rho\phi} = \overline{\rho}\tilde{\phi} + \overline{\rho\phi''},$$

which is simplified using $\overline{\rho}\,\tilde{\phi} = \overline{\rho\phi}$ and gives $\overline{\rho\phi''} = \overline{\rho}\,\widetilde{\phi''} = 0$, and thus $\widetilde{\phi''} = 0$ *Q.E.D.*

Hence applying the Reynolds or Favre averaging to any linear term simply gives the corresponding mean quantity. The Reynolds-Averaged Navier Stokes equations are identical in form to the Favre-averaged equations (2.23), (2.25), (2.27), and (2.28) if one considers the over-line operation to be the Reynolds average. These equations do not form a closed set for the mean values since terms have appeared that cannot be expressed in terms of the Favre-average quantities which are computed. This is of course due to the non-linearity of the flow equations. Further relations are needed which are commonly called turbulence models because no exact relations have been derived — yet — for the turbulence correlations.

When dealing with the URANS equations in Favre-averaged form, it is convenient

to simplify the Reynolds stresses $\tau_{ij}$ by making use of the property for averages

$$\overline{\phi_1\phi_2} = \overline{\phi_1}\,\overline{\phi_2} + \overline{\phi_1'\phi_2'}$$

in its expression for Favre-average quantities

$$\widetilde{\phi_1\phi_2} = \widetilde{\phi_1}\,\widetilde{\phi_2} + \widetilde{\phi_1''\phi_2''}$$

in order to write

$$\tau_{ij} = -\overline{\rho}\left(\widetilde{u_i u_j} - \widetilde{u_i}\,\widetilde{u_j}\right) = -\overline{\rho}\left(\widetilde{u_i}\widetilde{u_j} + \widetilde{u_i'' u_j''} - \widetilde{u_i}\,\widetilde{u_j}\right). \tag{2.39}$$

Thus, in URANS simulation where time averages are used, the Reynolds stresses to be modeled are simply

$$\tau_{ij} = -\overline{\rho}\,\widetilde{u_i'' u_j''} = -\overline{\rho u_i'' u_j''} \tag{2.40}$$

and as such are referred to as *turbulent* Reynolds stresses since they involves fluctuating velocity components.

In this work, two turbulence models are used in conjunction with the URANS equations: the Spalart-Allmaras one-equation model and the two-equation $k$-$\tau$ model by Speziale *et al.* (1992). Both of these models belong to the family of eddy-viscosity models since they rely on the eddy viscosity (also called turbulent viscosity) hypothesis introduced by Boussinesq in 1877 which assumes that the Reynolds stresses are analogous to a stress and hence are assumed proportional to the strain, *i.e.* in compressible flow

$$-\overline{\rho u_i'' u_j''} = \mu_t\left(\frac{\partial \overline{u_i}}{\partial x_j} + \frac{\partial \overline{u_j}}{\partial x_i}\right) - \frac{2}{3}\overline{\rho}\,k\delta_{ij} \tag{2.41}$$

where $k$ is the turbulent kinetic energy defined as

$$k \equiv \frac{1}{2}\frac{\overline{\rho u_i'' u_i''}}{\overline{\rho}} = \frac{1}{2}\widetilde{u_i'' u_i''}.$$

and $\mu_t$ is the eddy (or turbulent) viscosity which needs to be modeled. It is interesting to note than in incompressible flows we model $-\overline{u_i' u_j'}$ and use the turbulent kinematic viscosity $\nu_t$, both viscosities being of course related through the density.

Hence the effect of turbulence is to increase dissipation and can be characterized by the eddy viscosity, as if the turbulent eddies were colliding and exchanging momentum, in analogy with the collision of the fluid molecules which determines the viscosity of the fluid. Thus one can simply replace the viscosity coefficient in the momentum equation by an effective viscosity which is the sum of the laminar viscosity — a fluid property — and of the turbulent viscosity — a flow property.

There have been many objections to the validity of this hypothesis, mainly because the analogy between molecular and eddy viscosity has no real physical basis: eddies, contrary to molecules, are not rigid and are deformed by collisions. Furthermore, the eddy viscosity concept imposes that the Reynolds stress vanishes whenever the velocity gradient is zero, which is contrary to certain observations, for instance in decaying grid turbulence and along the centerline of a round jet [Pope (2000)]. However, a viscosity scalar yields good results whenever one of the velocity gradients, thus when one of the Reynolds stresses, is dominant and hence works well for thin-layer simulations where turbulence is mainly isotropic.

Another disadvantage is that some flow situations require a negative turbulent viscosity which is not physically sound, and the eddy viscosity is a scalar — which implicitly assumes the flow to be isotropic — while it might need to take different values for the different components of the Reynolds stresses in order to properly model the flow. Finally, the eddy viscosity models do not take into account the history of the flow — as if turbulence could be reduced to an instant in time, which has been shown not to be true for instance when a boundary layer transitions in the presence of free-stream turbulence [Pénéau *et al.* (2000) and Pénéau *et al.* (2004)] — and the assumption that the Reynolds stresses are aligned with the deformation tensor is not always justified. Yet, eddy viscosity models are extremely popular, because of their

THIS PAGE MISSING FROM ORIGINAL DOCUMENT SUBMITTED

identical to $\mu_t$ except in the viscous region, and is defined by

$$\mu_t = \breve{\mu} f_{\mu_1}(\chi) \tag{2.42}$$

for

$$\chi \equiv \frac{\breve{\mu}}{\mu}. \tag{2.43}$$

A partial differential equation is used for the intermediate variable, namely

$$\begin{aligned} \frac{D\breve{\mu}}{Dt} &= c_{b_1}\left[1 - f_{t_2}\right]\breve{S}\breve{\mu} + \frac{1}{\sigma}\left[\nabla\cdot\left(\left(\mu+\breve{\mu}\right)\nabla\breve{\mu}\right) + c_{b_2}\left(\nabla\breve{\mu}\right)^2\right] \\ &\quad - \left[c_{w_1} f_w - \frac{c_{b1}}{\kappa^2} f_{t_2}\right]\left[\frac{\breve{\mu}}{d}\right]^2 + f_{t_1}\Delta U^2 \end{aligned} \tag{2.44}$$

where $D/Dt \equiv \partial/\partial t + u_i \partial/\partial x_i$ is the total derivative and $\breve{S} \equiv S + \frac{\breve{\mu}}{\kappa^2 d^2} f_{v_2}$. The values of the constants and intermediary functions can be found in Appendix A.

In the above equations and coefficients, the subscript $b$ stands for *basic* and the corresponding terms are related to the production — first term in (2.44) — and diffusion — second term in (2.44) — of eddy viscosity. The subscript $w$ stands for *wall* and as Spalart & Allmaras (1994) point out "in a boundary layer the blocking effect of a wall is felt at a distance through the pressure term, which acts as the main destruction term for the Reynolds shear stress. This suggests a destruction term in the transport equation for the eddy viscosity" which is the third term in (2.44). The subscript $v$ stands for *viscous* and the corresponding terms are related to the wall function in the boundary layer. Finally, the subscript $t$ stands for *trip* which refers to fact that "the transition point is imposed by an actual trip, or natural but obtained from a separate method [...]. In a Navier-Stokes code [...] the model is 'primed' by numerical errors upstream of the trip. It then transitions at a rate that depends on numerical details and has little to do with the boundary layer's true propensity to transition, as controlled by pressure gradient, suction, and so on." [*id.*]. Thus through the introduction of the trip term the model is able to account fairly well for boundary

layer transition without being very sensitive to boundary layer resolution.

In this work, we study the flow around a static circular cylinder at Reynolds number based on diameter of 3900 and the flow on an oscillating cylinder at Reynolds number 3600. Thus, in all the cases considered, the boundary layer separates while it is still laminar, and the transition to turbulence takes place in the resulting shear layer [Zdravkovich (1997)]. Thus the trip term in the Spalart-Allmaras model — last term in equation (2.44) — should not significantly affect the ability of the model to predict the flow under consideration, and is not implemented in the computational code used.

### 2.2.3 $k$-$\tau$ Model by Speziale *et al.*

Attempting to encompass all the characteristics of turbulence into a single equation is very difficult, as attested by the complexity of the Spalart-Allmaras modeling equation; thus, very early, researchers have used two or more equations in order to model turbulence. In the early nineties, the $k$-$\epsilon$ model and its variants (where $k$ is the turbulent kinetic energy and $\epsilon = \nu \overline{\partial u_i'/\partial x_j \, \partial u_i'/\partial x_j}$ is the turbulent dissipation rate) were the most popular two-equation models in use but their limitation was starting to be felt in the computing community, in particular its inadequacy to be integrated with a solid boundary — which is necessary when wall transport properties are required or where there is flow separation [see Djilali *et al.* (1991), Speziale *et al.* (1992)] — due to the fact that it is not asymptotically consistent. Alternative models were being proposed, such as $k$-$\omega$ models which make use of an equation for the reciprocal turbulent time scale $\omega = \epsilon/k$. In 1992, C.G. Speziale, R. Abid, and E.C. Anderson proposed a $k$-$\tau$ model where equations for the turbulent kinetic energy $k$ and the turbulent time scale $\tau \equiv k/\epsilon$ are used. The model solves for the eddy viscosity as

$$\mu_t = \overline{\rho} C_\mu f_\mu k \tau \tag{2.45}$$

with the model equations being the transport for turbulent kinetic energy, $k$, and turbulent time scale, $\tau$, as given in Appendix A.

Wall variables are used, namely

$$y^+ \equiv y u_\tau / \nu \tag{2.46}$$

where the shear velocity $u_\tau$ is defined by

$$u_\tau \equiv \sqrt{\sigma_w / \rho} \tag{2.47}$$

and the wall shear stress $\sigma_w$ is given by

$$\sigma_w = \mu \left( \frac{\partial \overline{u_1}}{\partial x_2} + \frac{\partial \overline{u_2}}{\partial x_1} \right)_{wall} \tag{2.48}$$

since the wall is assumed to be located on an $x_1$-$x_3$ plane and perpendicular to the local $x_2$ direction.

The two main contributions of Speziale *et al.* (1992) with respect to previous two-equation turbulence models (such as the classical $k$-$\epsilon$) are: improved asymptotic behavior (*i.e.* near the wall $k \sim y^2$ as expected) thanks to the introduction of a wall damping function, and the existence of a "natural" boundary condition for the turbulent time scale $\tau$, namely $\tau = y^2/2\nu$. "The improved wall damping functions [were] obtained by an asymptotic analysis using the results of direct numerical simulations of turbulent channel flow" [Speziale *et al.* (1992)]. The interested reader can find more details on the models and test cases in the publication by Speziale *et al.* (1992).

## 2.3 Subgrid-Scale Models for Large Eddy Simulation

### 2.3.1 Principle

The simulation of turbulent flows using URANS methods can be very useful and efficient whenever the main goal is to predict mean quantities of engineering interest. However, they are inadequate whenever one wishes to observe smaller scale motions, or study phenomena associated with unsteady turbulent motions, such as aeroacoustics. For most applications, the computational cost of DNS is prohibitive while URANS approaches are not accurate enough; an intermediate approach is the use of a Large Eddy Simulation (LES).

In a LES, the large scale motions are resolved while the small scale ones are modeled through a subgrid-scale model; this can be thought of as applying a DNS to the large scales and a URANS to the small ones. The principle behind LES is thus justified by the fact that the larger scales, because of their size and strength, carry most of the flow energy and are responsible for most of the transport, and therefore should be simulated precisely (*i.e.* resolved). On the other hand, the small scales have relatively little influence on the mean flow and thus can be approximated (*i.e.* modeled). Furthermore, small scales tend to be more homogeneous and isotropic and hence are far easier to model than the large scales, which yields high accuracy of the overall simulations. Therefore, the limit between the resolved and the subgrid scales should be located in the inertial subrange where the energy decays as $k^{-5/3}$.

The fields are decomposed as follows

$$\phi(x_i,t) = \overline{\phi(x_i,t)} + \phi'(x_i,t) \tag{2.49}$$

where

$$\overline{\phi(x_i,t)} = \int G(x_i - x_i')\phi(x_i')dx' \tag{2.50}$$

is the resolved, or filtered [Leonard (1974)], large-scale component, and $\phi'(x_i,t)$ is the subgrid component. The spatial filter kernel, $G(x_i - x_i')$, is a localized function which filters out any wavelength smaller that the filter cutoff wavelength $k_f$, and is normalized such that $\int G(x_i - x_i')dx' = 1$. Several types of filter kernels have been used in LES, among which the Gaussian filter (smooth and infinitely differentiable), the box filter (average over a rectangular region), the cutoff filter (used in Fourier space to eliminate all coefficients below the cutoff), and the top-hat filter (implicit filtering by numerical discretization). In the early days of LES, the filter and the discretization grid were closely related, and hence the adjective subgrid is used to refer to the non-filtered components, even though a relation between the filter and the grid is generally not required.

The main difference between the URANS and the LES approaches is that in a URANS simulation a time averaging is used through the Reynolds decomposition while a LES uses a spatial averaging (filtering). Contrary to the Reynolds decomposition, in the resolved-subgrid decomposition $\overline{\overline{\phi}} \neq \overline{\phi}$ and $\overline{\phi'} \neq 0$.

The governing equations to be solved are the Favre-filtered equations (2.23), (2.25), (2.27), and (2.28) where the overline denotes filtered variables. A closure issue similar to the one encountered in URANS type simulations arises, since

$$\overline{\rho}\,\widetilde{u_i u_j} \neq \overline{\rho}\,\widetilde{u}_i\,\widetilde{u}_j \tag{2.51}$$

and hence the subgrid-scale Reynolds stresses, $\overline{\rho}\,\widetilde{u_i u_j}$, cannot be expressed in terms of resolved variables such as $\widetilde{u}_i$ and needs to be modeled. We chose to model the subgrid-scale stress terms $\tau_{ij}$ as they appear in the Favre-filtered equations, namely

$$\tau_{ij} \equiv \overline{\rho}\,(\,\widetilde{u_i u_j} - \widetilde{u}_i\widetilde{u}_j\,)\,. \tag{2.52}$$

In this work, three different subgrid-scale models are considered: the Smagorinsky-Lilly model (1967), the dynamic Smagorinsky model, and the dynamic mixed model (DMM) by Zang *et al.* (1993).

### 2.3.2 The Smagorinsky-Lilly Subgrid-Scale Model

The simplest and most commonly used subgrid-scale model is the one proposed by the climatologist Smagorinsky (1963). It is an eddy viscosity model based on the hypothesis that the small-scale structures are in equilibrium: by equating the energy production to the energy dissipation, the transport of turbulent kinetic energy yields the model equation in compressible flow as

$$\tau_{ij} = -2\mu_t \overline{S_{ij}} \tag{2.53}$$

where the rate of strain $\overline{S_{ij}}$ is defined by

$$\overline{S_{ij}} \equiv \frac{1}{2}\left(\frac{\partial \overline{u_i}}{\partial x_j} + \frac{\partial \overline{u_j}}{\partial x_i}\right). \tag{2.54}$$

The detailed derivation of the Smagorinsky subgrid-scale model can be found in Ferziger & Perić (2002) and Gatski *et al.* (1996).

The subgrid-scale viscosity is then given by

$$\mu_t = \overline{\rho}\,(C_S\Delta)^2\,|\overline{S}| \tag{2.55}$$

where $C_S$ is the Smagorinsky constant, $\Delta$ is the size of the largest subgrid-scale eddies (length associated with the filter), and $|\overline{S}| = \sqrt{2\overline{S_{ij}}\,\overline{S_{ij}}}$ is the characteristic filtered rate of strain. The filter width $\Delta$ is defined by

$$\Delta \equiv (\Delta_1\Delta_2\Delta_3)^{1/3} \tag{2.56}$$

where $\Delta_i$ is the filter size in the $ith$ direction.

From the way the model is setup, there is an obvious drawback: the Smagorinsky constant needs to be tailored to the particular flow and even Reynolds number. Another major shortcoming is that the model can be excessively dissipative (see Germano *et al.* (1991)); thus one has to reduce the value of the Smagorinsky constant to 0.065 (instead of the 0.2 value originally proposed and which works well for isotropic turbulence). Furthermore, the model constant needs to be reduced near walls.

The main deficiencies of the Smagorinsky model are summarized by Zang *et al.* (1993) as

(i) it requires an input model constant which is flow dependent;

(ii) it yields incorrect asymptotic behavior near walls and in laminar flow;

(iii) it does not allow for energy backscatter from the subgrid-scale eddies to the resolved ones;

(iv) and it assumes that the principal axes of the subgrid-scale stress tensor are aligned with those of the resolved strain rate tensor.

A successful way to reduce the eddy viscosity near the walls, and hence to respond to issue (ii) is to apply the van Driest damping function which is commonly used in URANS models to reduce the eddy viscosity near walls, such that

$$C_S^2 = C_{S_0}^2 \left[1 - \exp\left(-y^+/A^+\right)\right]^2 \tag{2.57}$$

where $C_{S_0}$ is the undamped Smagorinsky constant, $y^+ = yu_\tau/\nu$ is the distance to the wall in wall units, and $A^+$ is a constant which characterizes the damping magnitude. The use of the van Driest damping (2.57) with $C_{S_0} = 0.065$ and $A^+ = 25$ in conjunction with the original Smagorinsky model was proposed by Lilly (1967) and is usually referred to as the Smagorinsky-Lilly subgrid-scale model.

### 2.3.3 Subgrid-Scale Reynolds Stress Decomposition

In early LES of incompressible flow, decomposition of velocity in terms of resolved and subgrid-scale components was introduced in the first term of the Reynolds stress only, as follows

$$\begin{aligned}
\tau_{ij} &= \overline{u_i u_j} - \overline{u_i}\,\overline{u_j} \\
&= \overline{\left(\overline{u_i} + u_i'\right)\left(\overline{u_j} + u_j'\right)} - \overline{u_i}\,\overline{u_j} \\
&= \overline{\overline{u_i}\,\overline{u_j} + \overline{u_i}u_j' + u_i'\overline{u_j} + u_i'u_j'} - \overline{u_i}\,\overline{u_j} \\
&= \overline{\overline{u_i}\,\overline{u_j}} + \overline{\overline{u_i}u_j'} + \overline{u_i'\overline{u_j}} + \overline{u_i'u_j'} - \overline{u_i}\,\overline{u_j} \\
&= \left[\overline{\overline{u_i}\,\overline{u_j}} - \overline{u_i}\,\overline{u_j}\right] + \left[\overline{\overline{u_i}u_j'} + \overline{u_i'\overline{u_j}}\right] + \left[\overline{u_i'u_j'}\right]
\end{aligned}$$

or

$$\tau_{ij} = \mathcal{L}_{ij} + \mathcal{C}_{ij} + \mathcal{R}_{ij} \tag{2.58}$$

with

$$\mathcal{L}_{ij} \equiv \overline{\overline{u_i}\,\overline{u_j}} - \overline{u_i}\,\overline{u_j} \tag{2.59}$$

$$\mathcal{C}_{ij} \equiv \overline{\overline{u_i}\,u_j'} + \overline{\overline{u_j}\,u_i'} \tag{2.60}$$

$$\mathcal{R}_{ij} \equiv \overline{u_i'u_j'} \tag{2.61}$$

The *Leonard* terms $\mathcal{L}_{ij}$ represent the production of small-scale eddies due to the interaction of two resolved scales and can be computed explicitly from the resolved field. The *cross* terms $\mathcal{C}_{ij}$ represent the interaction between large eddies and small eddies, and can transfer energy between the two in either direction; thus it is responsible for *backscattering*, *i.e.* energy transfer from the subgrid scales to the larger resolved ones. The *Reynolds* terms $\mathcal{R}_{ij}$ account for the interaction between two small eddies.

It is important to note that the decomposition based on definitions (2.59), (2.60), (2.61) does not have the property of Galilean invariance — *i.e.* the same laws are valid

on any inertial reference frame — as pointed out by Speziale (1985). Specifically $\mathcal{R}_{ij}$ is invariant and so is the sum $\mathcal{L}_{ij}+\mathcal{C}_{ij}$, but not the terms $\mathcal{L}_{ij}$ and $\mathcal{C}_{ij}$ by themselves. Thus if the Leonard term is computed explicitly, as it can be, the results will not be invariant with change of reference frame. This motivated Germano *et al.* (1991) to re-derive the terms by introducing the decomposition into both of the terms composing the Reynolds stresses, namely

$$\begin{aligned}
\tau_{ij} &= \overline{u_i u_j} - \overline{u_i}\,\overline{u_j} \\
&= \overline{(\overline{u_i}+u_i')\left(\overline{u_j}+u_j'\right)} - \overline{\overline{u_i}+u_i'}\,\overline{\overline{u_j}+u_j'} \\
&= \overline{\overline{u_i}\,\overline{u_j}+\overline{u_i}u_j'+u_i'\overline{u_j}+u_i'u_j'} - \left(\overline{\overline{u_i}}+\overline{u_i'}\right)\left(\overline{\overline{u_j}}+\overline{u_j'}\right) \\
&= \overline{\overline{u_i}\,\overline{u_j}}+\overline{\overline{u_i}u_j'}+\overline{u_i'\overline{u_j}}+\overline{u_i'u_j'}-\overline{\overline{u_i}}\,\overline{\overline{u_j}}-\overline{\overline{u_i}}\,\overline{u_j'}-\overline{u_i'}\,\overline{\overline{u_j}}-\overline{u_i'}\,\overline{u_j'} \\
&= \left[\overline{\overline{u_i}\,\overline{u_j}}-\overline{\overline{u_i}}\,\overline{\overline{u_j}}\right]+\left[\overline{\overline{u_i}u_j'}+\overline{u_i'\overline{u_j}}\right]+\left[\overline{u_i'u_j'}-\overline{u_i'}\,\overline{u_j'}\right]
\end{aligned}$$

which is equivalent to taking

$$\tau_{ij} = \mathcal{L}_{ij}^m + \mathcal{C}_{ij}^m + \mathcal{R}_{ij}^m \tag{2.62}$$

and redefining the terms as

$$\mathcal{L}_{ij}^m \equiv \overline{\overline{u_i}\,\overline{u_j}}-\overline{\overline{u_i}}\,\overline{\overline{u_j}} \tag{2.63}$$

$$\mathcal{C}_{ij}^m \equiv \overline{\overline{u_i}\,u_j'}+\overline{\overline{u_j}\,u_i'}-\left(\overline{\overline{u_i}}\,\overline{u_j'}+\overline{\overline{u_j}}\,\overline{u_i'}\right) \tag{2.64}$$

$$\mathcal{R}_{ij}^m \equiv \overline{u_i'u_j'}-\overline{u_i'}\,\overline{u_j'} \tag{2.65}$$

with the additional constraint that the filter must be a linear function (*i.e.* $\overline{f_1+g_2} = \overline{f_1}+\overline{g_2}$ and $\overline{\alpha f} = \alpha\overline{f}$ for any variables $f$ and $g$, and any scalar $\alpha$). The superscript $m$ refers to *modified* and the above terms are known as the *modified Leonard terms*, the *modified cross terms* and the *modified Reynolds terms*, respectively.

Now, if when dealing with a compressible flow one tries to proceed in a similar

manner, one would start by writing the subgrid Reynolds stresses as

$$\begin{aligned}
\tau_{ij} &= \overline{\rho}\widetilde{u_i u_j} - \overline{\rho}\,\widetilde{u}_i\,\widetilde{u}_j \\
&= \overline{\rho u_i u_j} - \frac{\overline{\rho}\,\widetilde{u}_i\,\overline{\rho}\,\widetilde{u}_j}{\overline{\rho}} \\
&= \overline{\left(\frac{\rho u_i \rho u_j}{\rho}\right)} - \frac{\overline{\rho u_i}\,\overline{\rho u_j}}{\overline{\rho}}
\end{aligned}$$

and introduce the decomposition

$$\rho u_i = \overline{\rho u_i} + (\rho u_i)'$$

to get

$$\begin{aligned}
\tau_{ij} &= \overline{\left(\frac{\left(\overline{\rho u_i} + (\rho u_i)'\right)\left(\overline{\rho u_j} + (\rho u_j)'\right)}{\rho}\right)} - \frac{\overline{\overline{\rho u_i} + (\rho u_i)'}\,\overline{\overline{\rho u_i} + (\rho u_i)'}}{\overline{\rho}} \\
&= \left[\overline{\left(\frac{\overline{\rho u_i}\,\overline{\rho u_j}}{\rho}\right)} - \frac{\overline{\overline{\rho u_i}}\,\overline{\overline{\rho u_j}}}{\overline{\rho}}\right] \\
&\quad + \left[\overline{\left(\frac{\overline{\rho u_i}\,(\rho u_j)'}{\rho}\right)} + \overline{\left(\frac{(\rho u_j)'\,\overline{\rho u_i}}{\rho}\right)} - \left(\frac{\overline{\overline{\rho u_i}}\,\overline{(\rho u_j)'}}{\overline{\rho}} + \frac{\overline{(\rho u_j)'}\,\overline{\overline{\rho u_i}}}{\overline{\rho}}\right)\right] \\
&\quad + \left[\overline{\left(\frac{(\rho u_i)'\,(\rho u_j)'}{\rho}\right)} - \frac{\overline{(\rho u_i)'}\,\overline{(\rho u_j)'}}{\overline{\rho}}\right]
\end{aligned}$$

which is equivalent to defining the Leonard, cross, and Reynolds terms as, respectively

$$\mathcal{L}_{ij}^c = \overline{\left(\frac{\overline{\rho u_i}\,\overline{\rho u_j}}{\rho}\right)} - \frac{\overline{\overline{\rho u_i}}\,\overline{\overline{\rho u_j}}}{\overline{\rho}} \tag{2.66}$$

$$\mathcal{C}_{ij}^c = \overline{\left(\frac{\overline{\rho u_i}\,(\rho u_j)'}{\rho}\right)} + \overline{\left(\frac{(\rho u_j)'\,\overline{\rho u_i}}{\rho}\right)} - \left(\frac{\overline{\overline{\rho u_i}}\,\overline{(\rho u_j)'}}{\overline{\rho}} + \frac{\overline{(\rho u_j)'}\,\overline{\overline{\rho u_i}}}{\overline{\rho}}\right) \tag{2.67}$$

$$\mathcal{R}_{ij}^c = \overline{\left(\frac{(\rho u_i)'\,(\rho u_j)'}{\rho}\right)} - \frac{\overline{(\rho u_i)'}\,\overline{(\rho u_j)'}}{\overline{\rho}} \tag{2.68}$$

The problem that arises is that these terms involve both $\rho$ and $\overline{\rho}$, thus in particular the

Leonard terms cannot be calculated explicitly, which they could be in incompressible flow, and need to be modeled. This is a fundamental issue, too often overlooked, in Large Eddy Simulation of compressible flows.

### 2.3.4 The Self-Similarity Subgrid-Scale Model of Bardina *et al.*

The scale-similarity model of Bardina (1983) does not assume colinearity (*i.e.* axes alignment) between the subgrid-scale stress and the resolved strain rate. It relies on the idea that "the important interactions between the resolved and unresolved scales involve the smallest eddies of the former and the largest eddies of the latter *i.e.* eddies that are a little larger or a little smaller than the length scale, $\Delta$, associated with the filter". When combining the scale-similarity approach with the Smagorinsky subgrid-scale model, one obtains what is called a *mixed* model.

For incompressible flows, Bardina (1983) suggested that the Leonard terms be computed explicitly and the terms $\mathcal{C}_{ij} + \mathcal{R}_{ij}$ be modeled following the self-similarity principle, and hence assuming that

$$\overline{\overline{u_i}} \approx \overline{u_i} \quad \text{and} \quad u_i' \approx \overline{u_i} - \overline{\overline{u_i}} \tag{2.69}$$

from which

$$\mathcal{C}_{ij} = \overline{\overline{u_i}}\left(\overline{u_j} - \overline{\overline{u_j}}\right) + \overline{\overline{u_j}}\left(\overline{u_i} - \overline{\overline{u_i}}\right) \tag{2.70}$$

$$\mathcal{R}_{ij} = \left(\overline{u_j} - \overline{\overline{u_j}}\right)\left(\overline{u_i} - \overline{\overline{u_i}}\right) \tag{2.71}$$

such that what the model reads

$$\mathcal{C}_{ij} + \mathcal{R}_{ij} = \overline{u_i}\,\overline{u_j} - \overline{\overline{u_i}}\,\overline{\overline{u_j}} \tag{2.72}$$

Originally, Bardina (1983) introduced a factor of 1.1 in front of the right-hand-side of (2.72), but Speziale (1985) suggested a factor of unity instead in order to respect Galilean invariance.

The study of DNS results showed that the approximation (2.72) is inaccurate near walls [Gatski *et al.* (1996)], which can be explained by noting that Bardina's model suited for Galilean invariance is equivalent, in incompressible flow, to calculating explicitly the Leonard terms and neglecting the cross and Reynolds terms [Speziale (1985)]. However, as explained in the previous section, in compressible flow the equivalent of the Leonard term, $L_{ij}$, cannot be computed explicitly anymore and is modeled following Vreman (1995) as

$$L_{ij}^c = \overline{\left(\frac{\overline{\rho u_i}\,\overline{\rho u_j}}{\overline{\rho}}\right)} - \frac{\overline{\overline{\rho u_i}}\,\overline{\overline{\rho u_j}}}{\overline{\overline{\rho}}} \tag{2.73}$$

$$L_{ij}^c = \overline{\overline{\rho}\,\widetilde{u_i}\,\widetilde{u_j}} - \frac{\overline{\overline{\rho}\widetilde{u_i}}\,\overline{\overline{\rho}\widetilde{u_j}}}{\overline{\overline{\rho}}}. \tag{2.74}$$

The right-hand side can be computed directly from the resolved fields, but the equality is not exact and one should keep in mind that it remains a model.

Even though the Leonard terms are dominant, energy dissipation down to subgrid-scales is not possible since the model is only a function of the resolved field. Thus, the self-similarity procedure alone hardly dissipates any energy and needs to be combined with another model. "It was found that the scale similarity model did not dissipate energy, however, when it was combined linearly with the Smagorinsky model, the resulting "mixed model" did dissipate energy and predicted turbulence statistics better than the Smagorinsky model alone" [Zang *et al.* (1993)].

Bardina's self-similarity procedure has the great advantages of providing energy backscatter from the subgrid-scale structures, and of not requiring alignment between the subgrid-scale stress tensor, $\tau_{ij}$, and the resolved strain rate tensor, $\overline{S_{ij}}$.

### 2.3.5 The Dynamic Subgrid-Scale Model of Germano *et al.*

In order to overcome the main limitation of the Smagorinsky model — *i.e.* that it involves the use of a constant which needs to be tailored to the particular flow and which may need to vary between regions (issue (i) in the deficiencies list) — the constant can be made a variable parameter and computed from the resolved field as was proposed by Germano and collaborators [Germano *et al.* (1991) and Germano (1992)]; this procedure is called a *dynamic* approach.

The basic assumption is that the same parameter can model the resolved field and the field obtained from a coarser filter (called *test filter*), so these two fields can be compared in order to obtain the local value of the model parameter, which is local to every spatial point and every time step. Germano (1996) expresses this in the following way: "the basic ingredient of this new formulation is to derive the Smagorinsky coefficient [...] by imposing that two different large eddy representations of a turbulent flow: the computed large eddy simulation and a tested large eddy simulation at a higher level, are equivalent from a statistical point of view". The reader is referred to Ferziger & Perić (2002), Germano *et al.* (1991), Germano (1992), and Germano (1996) for further details.

The generalization of the dynamic model by Germano and collaborators to compressible flows was carried out by Moin *et al.* (1991), and is summarized in Appendix A. The subgrid-scale stress tensor is given by

$$\tau_{ij} = \overline{\rho}\left(\widetilde{u_i u_j} - \widetilde{u}_i \widetilde{u}_j\right) = \overline{\rho u_i u_j} - \frac{\overline{\rho u_i}\,\overline{\rho u_j}}{\overline{\rho}}.$$

where the tilde and over-line refer to Favre-filtered and resolved quantities, respectively. A test filter that has a larger width than the resolved filter (which is determined by the grid size) is now introduced, and test-filtered quantities are denoted by a hat operator which is always applied to resolved quantities. The test-filtered stress tensor

$\mathcal{T}_{ij}$ is defined similarly to the subgrid-scale stress tensor as

$$\mathcal{T}_{ij} \equiv \widehat{\overline{\rho u_i u_j}} - \frac{\widehat{\overline{\rho u_i}}\,\widehat{\overline{\rho u_j}}}{\widehat{\overline{\rho}}}.$$

Thus we define the compressible equivalent of the Leonard terms as

$$L_{ij} = \mathcal{T}_{ij} - \widehat{\tau_{ij}} = \left(\frac{\widehat{\overline{\rho u_i}\,\overline{\rho u_j}}}{\overline{\rho}}\right) - \frac{\widehat{\overline{\rho u_i}}\,\widehat{\overline{\rho u_j}}}{\widehat{\overline{\rho}}}$$

or

$$L_{ij} = (\widehat{\overline{\rho}\widetilde{u}_i\widetilde{u}_j}) - \widehat{\overline{\rho}}\,\widehat{\widetilde{u}}_i\widehat{\widetilde{u}}_i \tag{2.75}$$

It is important to note that $L_{ij}$ can be computed from the resolved fields, and is hence called the resolved stress. The test-filter is always applied to resolved quantities (*i.e.* the hat operator is always on top of an over-line), the test-filter width being larger than the resolved filter linked to the grid size.

Now the Smagorinsky eddy viscosity approach is followed, in the same formulation as Vreman (1995), such that

$$\tau_{ij} = -2\overline{\rho}C\Delta^2|\widetilde{S}|\widetilde{S_{ij}} \tag{2.76}$$

This is equivalent to making use of equation (2.53) with the subgrid-scale viscosity defined similarly to the one in the Smagorinsky model equation (2.55), except that the dynamic model constant $C$ is not squared so that negative values are possible to account for backscattering.

The parameter $C$ is determined using equation (2.75) for the resolved stress terms, and their expression is given by

$$C = -\frac{\langle \mathcal{L}_{ij}\mathcal{M}_{ij} \rangle}{\langle 2\Delta^2\mathcal{M}_{ij}\mathcal{M}_{ij} \rangle} \tag{2.77}$$

where

$$\mathcal{M}_{ij} = \widehat{\overline{\rho}} \left( \frac{\widehat{\Delta}}{\Delta} \right)^2 |\widehat{\overline{S}}| \, \widehat{\overline{S_{ij}}} - \overline{\rho} \widehat{|\overline{S}| S_{ij}} \tag{2.78}$$

where the operation $\langle \, \rangle$ refers to a volume average carried out at the level of the test filter (while some other authors average on a plane parallel to the wall or along an homogeneous direction); such an averaging procedure in necessary in order to avoid the fraction that defines the coefficients to be indeterminate from a vanishing of the denominator for instance. The reader is referred to the paper by Moin *et al.* (1991) for a complete derivation.

The ratio of test-filter size to filter size $\widehat{\Delta}/\Delta$ is the only adjustable input to the model. A ratio of two is appropriate when using a cutoff filter and can be justified as follows. For simplicity consider a one-dimensional grid; in order for a certain structure to be resolved, it needs to be at least twice as large as the grid spacing, and hence three grid nodes are needed. The subgrid-scale eddies are by definition the structures that the filter cannot resolve and hence their size is smaller than the filter width (distance between two grid nodes). A structure smaller than the test-filter width $\widehat{\Delta}$ is not seen by the hat operation but is captured by the original filter since the latter has a width $\Delta$ equal to half the size of the structure.

On the other hand, if the test-filter is much wider than the original filter, the test-filtered quantities may be influenced by the large scale motions; the subgrid-scale model should only account for the effects of the subgrid-scale motions on the large scale ones, and the model coefficient be the same for the filter and the test filter. "If the character of the test filter is very different from the basic filter, the assumption that [the model constant] is the same at the two levels might not be justified" [Germano (1996)], and furthermore "large values [of the ratio $\widehat{\Delta}/\Delta$] imply that the stresses due to the large energy-carrying structures are used to determine the contribution of the subgrid scales" [Germano *et al.* (1991)]. Therefore a ratio $\widehat{\Delta}/\Delta$

of two is adequate and is retained for this study.

When the dynamic procedure is combined with the Smagorinsky model, as in the previous derivation, the dynamic localization Smagorinsky subgrid-scale model is obtained (localization refering to the fact that the value of the model parameter is local in time and space), or simply the dynamic Smagorinsky model.

The limitations of the dynamic Smagorinsky model proposed by Germano *et al.* (1991) are twofold: first, it still assumes that the principal axes of the subgrid-scale stress tensor are aligned with those of the resolved strain rate tensor; second excessive energy backscatter (very negative eddy viscosity) may occur due to the large fluctuations of the locally-computed coefficient, which can cause exponentially growing numerical instabilities [Zang *et al.* (1993)]. These numerical instabilities can partly be alleviated by setting a minimum value for the eddy viscosity equal to the negative of the molecular viscosity — a procedure called clipping — or alternatively by averaging the coefficient in space (along an homogeneous direction) or in time. The dynamic Smagorinsky model "can accurately predict mean flow quantities when the averaged model coefficient is used but gives inadequate representation of the local quantities" [Zang *et al.* (1993)].

### 2.3.6 The Dynamic Mixed Subgrid-Scale Model of Zang *et al.*

Zang *et al.* (1993) combined the dynamic procedure applied to the Smagorinsky model by Germano *et al.* (1991) with the mixed model of Bardina (1983) to obtain a dynamic mixed model. It makes use of the dynamic formulations with the modified Leonard, cross, and Reynolds terms defined in (2.63), (2.64), (2.65), respectively, and assumes that the mixed model can be applied to the test filter such that the test-filter stress can be written

$$\mathcal{T}_{ij} = -2\,C\,\widehat{\overline{\Delta}^2}\,|\widehat{\overline{S}}|\,\widehat{\overline{S}_{ij}} + \mathcal{L}_{ij}^{T} \tag{2.79}$$

where

$$\mathcal{L}_{ij}^{T} = \overline{\overline{\rho}\,\widetilde{u}_i\,\widetilde{u}_j} - \overline{\overline{\rho}}\,\overline{\widetilde{u}_i}\,\overline{\widetilde{u}_i} \tag{2.80}$$

Using the least-squares approach proposed by Lilly (1992), the model coefficient is finally given by

$$C = -\frac{\langle\,(\mathcal{L}_{ij} - \mathcal{H}_{ij})\,\mathcal{M}_{ij}\,\rangle}{\langle\,2\Delta^2\mathcal{M}_{ij}\mathcal{M}_{ij}\,\rangle} \tag{2.81}$$

where

$$\begin{aligned}
\mathcal{H}_{ij} &= \widehat{\left(\frac{\widehat{\rho u_i}\,\widehat{\rho u_j}}{\widehat{\overline{\rho}}}\right)} - \frac{\widehat{\overline{\rho u_i}}\,\widehat{\overline{\rho u_j}}}{\widehat{\overline{\overline{\rho}}}} - \left[\widehat{\left(\frac{\overline{\rho u_i}\,\overline{\rho u_j}}{\overline{\rho}}\right)} - \frac{\overline{\overline{\rho u_i}}\,\overline{\overline{\rho u_j}}}{\overline{\overline{\rho}}}\right] \\
&= \widehat{\widehat{\overline{\rho}}\,\widehat{\widetilde{u}_i}\,\widehat{\widetilde{u}_j}} - \widehat{\overline{\overline{\rho}}}\,\widehat{\overline{\widetilde{u}_i}}\,\widehat{\overline{\widetilde{u}_j}} - \left(\widehat{\overline{\rho}\,\widetilde{u}_i\,\widetilde{u}_j} - \overline{\overline{\rho}}\,\overline{\widetilde{u}_i}\,\overline{\widetilde{u}_i}\right) \qquad (2.82) \\
\mathcal{M}_{ij} &= \widehat{\overline{\rho}}\left(\frac{\widehat{\Delta}}{\Delta}\right)^2 |\widehat{\overline{S}}|\,\widehat{\overline{S}_{ij}} - \overline{\rho}\widehat{|\overline{S}|S_{ij}} \qquad (2.83)
\end{aligned}$$

For numerical stability, the total viscosity, $\mu + \mu_t$, is set to zero whenever its computed value is negative, which guarantees that the total viscosity — and hence the total diffusivity — is not negative.

The dynamic mixed subgrid-scale model by Zang *et al.* (1993) has the following characteristics: it satisfies Galilean invariance; it requires less modeling than the dynamic model since the modified Leonard terms, $\mathcal{L}_{ij}^{m}$, are explicitly calculated; provides energy backscatter from the subgrid-scale motion to the resolved scales; and it does not assume alignment between the subgrid-scale stress and the resolved strain rate tensors. The capabilities of the incompressible version of this model in capturing near wall dynamics have been shown in Pénéau *et al.* (2000) and Pénéau *et al.* (2004).

## 2.4 Very Large Eddy Simulation

### 2.4.1 Principle

LES has great advantages with respect to URANS simulations since in the latter all the turbulent (fluctuating) motions are modeled, while in the former only the subgrid-scale eddies are approximated. However, the computational cost of LES can be prohibitive for certain high Reynolds number flows, in particular near walls where the boundary layer needs to be resolved. An alternative is to carry out a *Very Large Eddy Simulation* (VLES) which is a compromise between LES and URANS methods.

In a LES "the filtered velocity field accounts for the bulk (say 80%) of the turbulent kinetic energy everywhere in the flow field. In VLES the grid and filter are too large to resolve the energy-containing motions, and instead a substantial fraction of the energy resides in the residual motions." [Pope (2000)]. As a consequence, a VLES can be carried out on a significantly coarser grid than a LES but is more sensitive to the accuracy of the subgrid-scale model. Because the purpose of running a VLES is to decrease the computational coast of the simulation and to be used on relatively coarse grids, subgrid-scale models used in VLES are usually derived from URANS models, this approach being often referred to as an *adaptive* turbulence model and was first suggested by Speziale (1998).

In practice, carrying out a VLES on a flow is often equivalent to performing a LES away from the walls and a URANS simulation close to the walls, with the advantage being to resolve precisely most of the large turbulent motions while not resolving the boundary layer in all its details.

### 2.4.2 Adaptive $k$-$\tau$ Model by Magagnato *et al.*

Magagnato & Gabi (2002) proposed a VLES method based on the $k$-$\tau$ model by Craft *et al.* (1995). Instead of choosing the grid size to be the filter width, the filter length

is chosen locally between the spatial filter width (determined by the grid)

$$L_s = 2\Delta = 2\left(\Delta x \times \Delta y \times \Delta z\right)^{1/3} \tag{2.84}$$

and the temporal filter width

$$L_t = |u| \times \Delta t \tag{2.85}$$

where $\Delta x$, $\Delta y$, $\Delta z$ are the grid cell sizes in the three coordinate directions, $\Delta t$ is the simulation time step, and $|u|$ is the flow velocity in the considered cell. Then the filter width is taken to be

$$\Delta = \max\left(L_s\,,\, L_t\right). \tag{2.86}$$

Through this filter width, the turbulent kinetic energy, $k$, and the turbulent time scale, $\tau$, are decomposed into a resolved and an un-resolved part; the un-resolved, or subgrid-scale, part is modeled through the non-linear eddy viscosity $k$-$\tau$ model by Craft *et al.* (1995), which uses the transport equations for $k$ and $\tau$, which are given in Appendix A.

The eddy viscosity is taken to be

$$\mu_t = \rho\, c_\mu\, f_\mu\, k'\, \tau' \tag{2.87}$$

and the subgrid-scale Reynolds stress is obtained from

$$-\overline{\rho u_i' u_j'} = -\widetilde{\bar{\rho} u_i' u_j'} = \rho c_\mu k' \tau' S_{ij} - \frac{2}{3}\rho k' \delta_{ij} - \rho v_i' v_j' + \frac{2}{3}\rho k' \delta_{ij}\,, \tag{2.88}$$

where $v_i'$ are random velocities calculated at each time step using a Langevin-type equation. Further details on the model and its derivation can be found in Appendix A and in Craft *et al.* (1995) and Magagnato & Gabi (2002).

The great advantage of the VLES model is that it can be used on any grid since the model adapts itself to the grid size through (2.86) so as to properly either resolve

or model the flow. Thus, it can be used on a grid as coarse as one used for a URANS computation and should predict turbulence as accurately as a LES away from the walls, while modeling the boundary layer flow.

This concludes our presentation of the turbulence models and subgrid-scale models considered in this work. The following section presents the numerical discretization techniques and solution methods employed, as well as the type of boundary condition used to set up the problem of a circular cylinder in uniform flow.

## 2.5 On the Computational Code SPARC

### 2.5.1 Overview

The main computation code used in this study, SPARC (Structured PArallel Research Code) — formerly known as KAPPA (KArlsruhe Parallel Program for Aerodynamics) — is a research code written in FORTRAN90 and chiefly developed by the Department of Fluid Machinery at the University of Karlsruhe, Germany, under the direction of Franco Magagnato. It runs in parallel architectures with distributed memory using Message Passing Interface (MPI), while having the capability to simulate a wide range of problems with its steady/unsteady, incompressible/preconditioned/compressible, inviscid/viscous, and laminar/turbulent solvers. A relatively large and leading-edge number of turbulence models and numerical schemes are already implemented and, most importantly, since the modular source code is available at the University of Victoria through a collaborative agreement, new models and schemes can be implemented and tested.

SPARC uses a collocated (*i.e.* non-staggered) cell-centered finite-volume method with second or fourth order central differences in space, and is block-structured with multigrid capabilities. Thus the solution domain is divided into computational grid cells to which the conservation equations are applied, and since it is cell-centered

the flow quantities are computed at the center of each cell (contrary to many incompressible codes, the grid is non-staggered, so the same point is used for velocity and pressure computations), while the values at the surface, when needed, are interpolated from the cell-centered values.

A semi-discrete method discretizes the governing equations into algebraic equations which can be solved using linear algebra techniques and CFD solution schemes. SPARC has many features and allows the user to chose among different solution methodologies — including, but not limited to, explicit 4th order time resolution and implicit dual time stepping; JST, SLIP, HCUSP, AUSM and Matrix Dissipation numerical dissipation schemes; $1^{st}$, $2^{nd}$ and $4^{th}$ order space discretization; Runge-Kutta explicit and LU-SSOR implicit schemes in space. We shall limit ourselves to describing those features that are employed in this study.

The flow is taken to be compressible, viscous, and turbulent, the turbulence models or subgrid-scale models used being the ones previously presented. No preconditioning is required since the flow Mach number is set to 0.2, so that compressibility effects remain low — in practice any flow below Mach 0.3 is usually considered incompressible — but the code remains relatively stable — compared to Mach numbers around 0.01 to 0.1 which require preconditioning. Thus the fully compressible Navier-Stokes equations in Favre-average form as presented in section 2.1.5 are solved.

### 2.5.2 Solvers and Discretization Algorithms

As mentioned earlier, a semi-discrete method is used in order to discretize the equations, which is done in two steps. First, discretization is carried out in space using the finite volume method with $2^{nd}$ order central difference, which yields a system of ordinary differential equations in time (the spatial elements having been transformed into an algebraic expression). Second, time discretization is done using dual time stepping. The result is an algebraic equation which can be solved numerically using

mathematical techniques such as linear algebra decompositions.

### Space Discretization

Discretization is done using the finite volume method, so the conservation equation for any quantity $\phi$ is considered in integral form as

$$\frac{\partial}{\partial t}\int\int\int_{\mathcal{V}} \rho\phi d\mathcal{V} + \int\int_{\mathcal{S}} \rho\phi\vec{V}\cdot\vec{n}d\mathcal{S} = \int\int_{\mathcal{S}} \Gamma\nabla\phi\cdot\vec{n}d\mathcal{S} + \int\int\int_{\mathcal{V}} q_\phi d\mathcal{V} \qquad (2.89)$$

where $\vec{V}$ is the flow velocity relative to the grid, $\Gamma$ is the diffusion coefficient, and $q_\phi$ is the source of $\phi$. The field is divided by means of a computational grid into control volumes over which the integrals need to be approximated. The first integral on the left-hand-side represents the rate of change of the quantity $\phi$ inside the control volume, and the second integral represents the flux of $\phi$ through the surfaces of the control volume due to convection (transport by velocity); the right-hand-side totals the creation/desctruction of the property, for instance net force exerted on the control volume with the surface integral corresponding to forces applied to the surfaces of the control volume (such as pressure or viscous forces), while the volume integral represents body forces (such as gravity or electromagnetic forces). In the case of the continuity equation, $\phi = \rho$, the right-hand side vanishes for non-reacting flows (mass is nor created nor destroyed), and in the case of the energy equation we account for work done by surface and by body forces.

Derivatives are approximated by the central-difference rule, which again is second order accurate. Second order accuracy in space is maintained by using the midpoint rule, such that volume and surface integrals are approximated as a product of the integrand and the volume or surface area, respectively. For the volume integrals, $\mathcal{V}$, the integrand is assumed constant over the control volume and is simply multiplied by the volume. For surface integrals, $\mathcal{S}$, the approximation is done in terms of integrands at one or more locations on the cell faces, these ones being obtained by interpolation

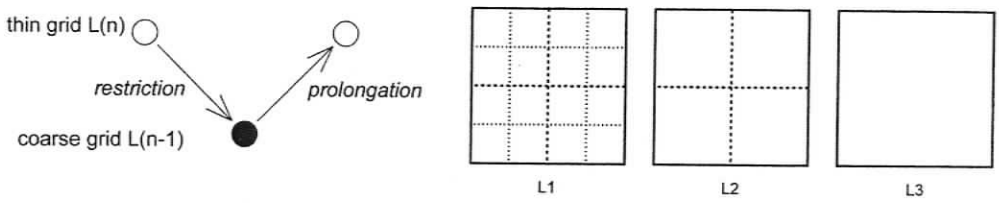


Figure 2.2: Illustration of (left) grid coarsening and (right) multigrid restriction-prolongation process.

from the nodal integrand values since the code is cell-centered.

The use of fourth order accurate methods in space was discarded since the resulting quantities would be only slightly different from the ones obtained with second order accuracy using an adequate grid, and yet the computational coast is much higher. In other words, for the problems considered here, it was inferred that the disadvantages of a fourth order discretization would outweigh its advantages over a second order one.

### Multigrid

Proposed by Federenko (1964), and first applied by Martinelli (1987) for viscous flow computations, the multigrid acceleration technique combines efficiency on coarse grids with accuracy on fine grids. The idea is to transfer some of the task of tracking the evolution of the system to a sequence of successively coarser meshes [Jameson (1986)]. In a multigrid technique, different error modes which add up to the total error (as in a Fourier series representation) are damped on different grids by aliasing (*i.e.* a short-wavelength wave on a fine grid is represented by a long-wavelength wave on a coarser grid).

A coarser grid, level L(n-1), is obtained by deleting every other line in the three directions, $i$, $j$, $k$, from a certain grid level L(n). A V-cycle, as illustrated in Figure 2.2, is used to move between grid levels with the following steps:

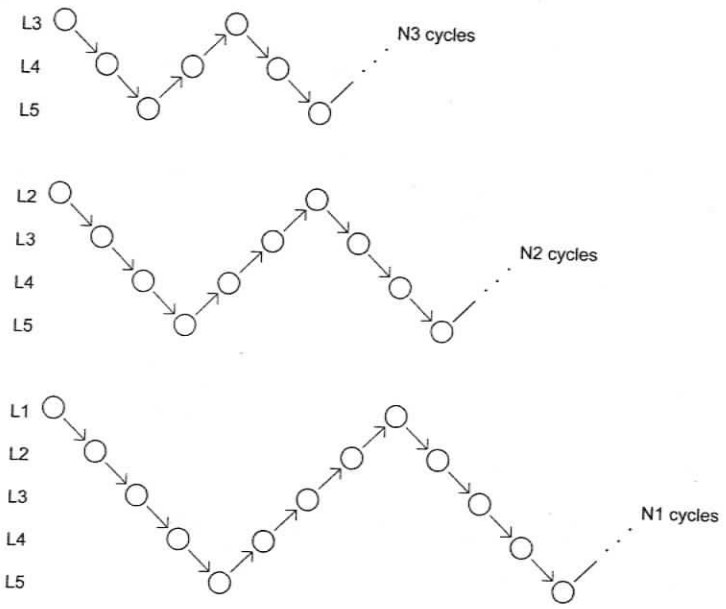


Figure 2.3: Full Multigrid (FMG) technique over a grid with five levels.

- error *smoothing* on fine grid (*i.e.* elimination of the high-frequency, short-wavelength, components of the error);

- *restriction*: transfer of the solution and residuals to a coarser grid, and solving on coarser grid;

- *prolongation*: transfer back the corrections (difference between transferred solution on finer grid and solution on coarser grid) to finer grid using interpolation;

- the new solution on the fine grid is the sum of the coarse-grid corrections and the fine-grid solution.

SPARC uses a Full Multigrid (FMG) technique, in which converged solutions on intermediate grids are used as initialization of the finest grid. Consider Figure 2.3 which illustrates the FMG technique on a grid with five levels, *i.e.* each block of the block-structured grid is coarsened four times. Let us call L1 the finest grid, and L5 the coarsest one. Multigrid operations will be done on levels L3, L4, and L5, and a number N3 of V-cycles will be performed on these levels to obtain the solution on

grid L3. Then the solution on L3 is interpolated to the grid L2, and N2 V-cycles are performed on the four grids L2, L3, L4, L5. Finally the solution on L2 is interpolated to L1 and N1 V-cycles are carried out on the full five-grid system, after which the final solution on the finest grid L1 is obtained.

The computational cost per time step is lower on coarser grids, while the use of large control volumes in coarse grids tracks the flow evolution on a larger scale so global equilibrium is more rapidly reached. Thus multigrid methods increase the convergence rate by a factor of 4 to 20 compared to single-grid methods, while they increase the computational cost by a factor of 2, which results in an overall reduction in computational time by a factor of 2 to 10 [Magagnato (2000)].

### Dual Time Stepping

Dual time stepping uses an implicit solver and allows for the use of larger time steps, compared to explicit techniques which are subject to stability limits linked to the Courant-Friedrichs-Lewy (CFL) number. Within a time step, a non-physical pseudo-time is introduced in order to make use of implicit solvers and their associated acceleration techniques.

In this dual step process, first a time-dependent source term is added to the residual which will control the solution's time accuracy; then the residual is driven to zero while keeping the physical time constant — iterations are carried out within a time step, similarly to the implicit convergence of a steady state problem. In pseudo-time, *i.e.* within each time step, an explicit Runge-Kutta five-stage method with standard coefficients and with pseudo-CFL of 5 is used. Note that the CFL can be as large as allowed by numerical stability since the precise resolution of the pseudo-time is unimportant and has no physical meaning, contrary to a real time that could induce a lack of accuracy if too large compared to the time scales of the flow to be resolved. In the dual time stepping, the time step is set by the user with the only restriction

being the temporal resolution of the flow scales.

The detailed procedure of dual time stepping is presented in Jameson (1991), of which we shall state here the main points. By applying the finite volume method over a cell with volume $\mathcal{V}$, a set of ordinary differential equations of the form

$$\frac{d(w\mathcal{V})}{dt} + R(w) = 0 \tag{2.90}$$

is obtained, where $R(w)$ is the residual equal to the sum of the fluxes through the cell. In order to use the multigrid scheme for a fully implicit time stepping, this equation is approximated as

$$D_t\left[w^{(n+1)}V^{(n+1)}\right] + R\left[w^{(n+1)}\right] = 0 \tag{2.91}$$

where $D_t$ is the central-difference operator and the superscript $n$ denotes the time level $n\Delta t$. Thus equation (2.90) is treated as a modified steady state problem to be solved using a multigrid method and a Runge-Kutta explicit scheme in the pseudo-time, denoted by a star, with modified residual $R^*(w)$:

$$\frac{dw}{dt^*} + R^*(w) = 0. \tag{2.92}$$

Since it is usually convenient to treat the convective and the dissipative terms of the Navier-Stokes equations in a different manner, the residual is divided as

$$R^*(w) = Q(w) + D(w) \tag{2.93}$$

for $Q(w)$ and $D(w)$ the convective and dissipative parts, respectively. Then, in an $m$

stage scheme,

$$\begin{aligned} w^{(n+1,0)} &= w^{(n)} \\ &\cdot \quad \cdot \quad \cdot \\ w^{(n+1,k)} &= w^{(n)} - \alpha_k \Delta t^* \left[ Q^{(k-1)} + D^{(k-1)} \right] \\ &\cdot \quad \cdot \quad \cdot \\ w^{(n+1)} &= w^{(n+1,m)} \end{aligned}$$

with

$$\begin{aligned} Q^{(0)} &= Q\left[w^{(n)}\right] \\ D^{(0)} &= D\left[w^{(n)}\right] \\ Q^{(k)} &= Q\left[w^{(n+1,k)}\right] \\ D^{(k)} &= \beta^{(k)} D\left[w^{(n+1,k)}\right] + \left(1 - \beta^{(k)}\right) D^{(k-1)} \end{aligned}$$

In the Runge-Kutta five-stage scheme employed in this work, $\alpha_i = (1/4\,,\, 1/6\,,\, 3/8\,,\, 1/2\,,\, 1)$ with three evaluations of dissipation $\beta_i = (1\,,0\,,\, 0.56\,,\, 0\,,\, 0.44)$ is appropriate [Jameson (1991)].

A Runge-Kutta method uses points between $t^{(n)}$ and $t^{(n+1)}$, so that only the initial condition is required. In the second order Runge-Kutta method used here, there are two steps: the first step is a half-step predictor

$$\phi^{(n+\frac{1}{2})} = \phi^{(n)} + \frac{\Delta t}{2} f(t^{(n)}, \phi^{(n)}) \tag{2.94}$$

and the second step is a midpoint rule

$$\phi^{(n+1)} = \phi^{(n)} + \Delta t\, f(t^{(n+\frac{1}{2})}, \phi^{(n+\frac{1}{2})}). \tag{2.95}$$

More details on the dual time stepping method can be found in Jameson (1983), Jameson (1991), De Palma *et al.* (2001), Breuer (1993) and Arnone *et al.* (1995).

Even while the dual-time stepping procedure requires a longer computational time to advance each time step than a single stepping process, the use of a larger time step compared to explicit methods will outweigh the increase in computational cost per time step and be finally faster, in general, to reach a given physical time.

### Numerical Dissipation Scheme

The use of discrete methods to solve complex flows cannot resolve all the scales of motion since any motion smaller than the grid characteristic size will not be captured; in other words, higher frequencies are harder to resolve numerically. Two waves with different frequencies interact through product terms (such as the non-linear terms in the momentum equation) to form a wave of higher frequency which is the sum of the original two, and a wave of lower frequency which amount to the difference. The generation of higher and higher frequencies, which is physically manifested by the presence of shocks or viscous dissipation, must be dealt with in the numerical technique to avoid inaccuracy and numerical instability.

A numerical dissipation scheme must be able to properly dissipate unresolved frequencies while having the least possible numerical impact on the accuracy of the simulation, *i.e.* minimum amount of artificial dissipation required for stability [Swanson *et al.* (1997)], and the lowest computational coast.

Many numerical dissipation schemes that introduce artificial dissipation into spatial discretization methods have been proposed, such as

- the scalar Jameson-Schmidt-Turkel (JST) scheme by Jameson *et al.* (1981);
- the Convective Upstream Split Pressure (CUSP) scheme by Jameson (1995*a*) and Jameson (1995*b*);

- the Symmetric LImited Positive (SLIP) scheme by Jameson (1985);
- the Advection Upstream Splitting Method (AUSM) scheme by Liou & Steffen (1993);
- and the Matrix Dissipation (MATD) scheme by Swanson & Turkel (1992).

Among these, the JST scheme has a simple pressure switch for shock detection and each wave is dissipated with the maximum eigenvalue of the inviscid flux Jacobian matrix, so it tends to be over-dissipative especially in boundary layers [Allmaras (1993)]. The others are high-resolution schemes which provide improved shock capturing with less artificial dissipation.

For this study, where one of the main goals is to assess the accuracy of turbulence modeling techniques applied to the vortex shedding behind circular cylinders, the selection of a numerical scheme is mainly driven by the pursuit of accuracy. As in Zingg *et al.* (1999), "we would like the numerical error to be significantly less than the physical model error, thus permitting accurate assessment of the physical model error". Hence for this study we chose a Matrix Dissipation scheme in which "the dissipative terms of each discrete equation are scaled by the appropriate eigenvalues of the flux Jacobian matrix rather than by the spectral radii [maximum eigenvalue], as in the JST scheme" [Swanson *et al.* (1997)]. It is based on the SPLIT scheme in the form proposed by Swanson & Turkel (1992), and has a very low numerical impact as concluded by several studies while being cost-effective in terms of computational requirements. Comparison of different schemes can be found in Swanson *et al.* (1997), Swanson *et al.* (1998), Zingg *et al.* (1999).

### 2.5.3 Boundary Conditions and Initialization

Fluxes through control-volume faces that lie on a boundary require special treatment, since their value cannot be approximated anymore by applying the midpoint rule to

nodes on either side of that particular face. Thus, these fluxes need to be either set, or be expressed in terms of interior and boundary values: values at the boundaries can be given, or gradients specified.

In the simulation of the flow around a cylinder, four different boundary conditions are used: no-slip for walls, farfield for the inlet and top and bottom surfaces of the computational domain, pressure outlet, and periodic in the direction of homogeneity (spanwise).

The no-slip condition is appropriate for walls in viscous calculations and imposes the wall velocity (zero when stationary, non-zero if moving) to the cells on the wall surface. This guaranties continuity between the solid region and the fluid, which results from viscous effects. The energy equation also requires a boundary condition, which is taken to be a zero heat flux at the wall.

The farfield boundary condition imposes a "free-stream" value to the velocity components, density, temperature, as well as a turbulence level $Tu = u_{rms}/U_0$ (where $U_0$ is the magnitude of the free-stream velocity and $u_{rms}$ the fluctuating magnitude) and an eddy viscosity ratio $\mu_t/\mu$. This boundary condition is based on the Riemann invariants normal to the boundary: if the flow exits, the tangential velocity components and energy are extrapolated from the interior of the domain, and if the flow enters they are set to the free-stream values. Any farfield boundary condition is located far from solid object and from significant perturbation, because the farfield should not significantly influence the interior of the domain and "perturbations" cannot exit through this fixed-property boundary.

The pressure outlet condition simply sets the static pressure and total temperature at the outlet to a fixed value, for which we take the ones corresponding to the inflow conditions set in the farfield boundary. The outlet is placed far from obstacles and an important buffer region with very large cells is placed adjacent to the outlet so as to dissipate any flow structures and keep the flow in most of the computational domain

undisturbed by the outlet.

Finally, a periodic boundary condition of translational type is used in the spanwise direction to simulate an infinitely wide domain. When two faces are defined to be periodic, the same values of all quantities (velocity, pressure, density, temperature, energy) are imposed on both faces. Thus, all the cells on a face linked to another by periodicity see the related face cells as neighbors.

Initialization is done by specifying the velocity components, density, temperature, turbulence level, and eddy viscosity ratio at all the grid points to the values corresponding to the inlet conditions.

## 2.6 Summary

In this chapter, the theory background for the simulation of a compressible, viscous, unsteady turbulent flow has been presented. The governing equations in Favre-average form are derived and the need for turbulence modeling techniques explained.

All the turbulence models and subgrid-scale models that are used for this study were introduced: the URANS Spalart & Allmaras (1994) model and $k$-$\tau$ model by Speziale *et al.* (1992), the Smagorinsky-Lilly and the dynamic mixed [Zang *et al.* (1993)] subgrid-scale models for LES, and the adaptive $k$-$\tau$ model by Magagnato & Gabi (2002) for VLES.

For the simulations that are presented next, the finite-volume, cell-centered, computational code SPARC is used, unless otherwise specified, with the compressible viscous solver, second order central-difference in space and second order dual time stepping in conjunction with the matrix dissipation scheme.

# Chapter 3

# Flow Around a Circular Cylinder

The results of the simulations of a stationary circular cylinder in uniform flow at a Reynolds number $Re_D = 3900$ and of a transversely oscillating circular cylinder at $Re_D = 3600$ are presented in this chapter. First, the problem setup is discussed together with the choice of computational grid and time step. For the problem of a stationary cylinder, a comparison of the results obtained with two different time steps is given, as well as a comparison between two- and three-dimensional simulations using the URANS $k$-$\tau$ model by Speziale *et al.* (1992). Then a detailed comparison of the data obtained with the different turbulence modeling techniques is carried out. The analysis of the results is done mainly in terms of average quantities (density, velocity, pressure, vorticity, drag coefficient, Strouhal number, *etc.*), but some instantaneous fields and profiles are also shown.

The results of the flow around a cylinder oscillating transversally at $Re_D = 3600$ are presented, for the two-dimensional simulations with URANS $k$-$\tau$ model by Speziale *et al.* (1992). The analysis focuses on the lock-in phenomena.

The numerical simulations were carried out on two computational clusters: Poseidon from the Department of Mechanical Engineering of the University of Victoria, which is a 30 processors (22 AMD Athlon 3200 32bit and 8 AMD Opteron 64bit)

machine running Red Hat Workstation 3; and mainly on Minerva from the Research Computing Facility at the University of Victoria, an IBM SP2 with 128 RS/6000 processors (375MHz 64bit).

For clarity, the following abbreviations are used to refer to the different turbulence modeling techniques used in this study

- **SA** or **Spalart-Allmaras** refers to the URANS turbulence model by Spalart & Allmaras (1994);
- **SP** or $k$-$\tau$ **Speziale** refers to the two-equation turbulence model for URANS closure by Speziale *et al.* (1992);
- **LES** or **Smagorinsky** refers to the LES with Smagorinsky-Lilly subgrid-scale model;
- **VLES** or **adaptive** $k$-$\tau$ refers to the subgrid-scale model for VLES by Magagnato & Gabi (2002).

## 3.1 Problem Setup and Computational Grid

The computational domain can be seen in the mesh image of Figure 3.1. The inlet boundary on the left-hand side of the figure is located 17 diameters upstream of the cylinder to allow the inflow to settle down before reaching the cylinder and to observe the influence of the presence of the obstacle on the incoming flow; the boundary condition is far-field and hence the velocity components are imposed to be $u = U_0 = 68.63\,m/s$, and $v = w = 0$, while the turbulence level $Tu = u_{rms}/U_0$ is set to 0.3%, and the ratio of eddy to molecular viscosity $\mu_t/\mu$ to unity. Table 3.1 summarizes the flow conditions.

The upper and lower boundaries are also set to far-field and are located at a distance of $20D$ from the center of the cylinder, where $D$ is the cylinder diameter;

Table 3.1: Summary of the free-stream flow conditions and cylinder dimensions for the study of the stationary cylinder in uniform flow.

| **Description** | **Symbol** | **Value** |
|---|---|---|
| Cylinder Diameter | $D$ | 1 m |
| Velocity | $U_0$ | 68.63 m/s |
| Density | $\rho_0$ | 0.0010301 kg/m$^3$ |
| Temperature | $T_0$ | 293 K = 20° C |
| Molecular Viscosity | $\mu$ | $1.812688 \times 10^{-5}$ kg/m·s |
| Ratio of Turbulent to Molecular Viscosity | $\mu_t/\mu$ | 1 |
| Turbulence level | $Tu$ | 0.3% |
| Static Pressure | $p_{ref}$ | 86.6221 Pa |
| Total Pressure | $p_{ref_0}$ | 89.0724 Pa |
| Total Temperature | $T_{ref_0}$ | 295.344 K |
| Mach Number | $M_0$ | 0.2 |
| Reynolds Number | $Re_D$ | 3900 |

this corresponds to a blockage (ratio of cylinder diameter to domain height) of 2.5%, which is significantly lower than the 20% needed to avoid blockage effects, according to the studies by Anagnostopoulos *et al.* (1996) and Anagnostopoulos & Minear (2004).

The outlet is placed 35 diameters downstream from the center of the cylinder. This is farther than most numerical studies for two reasons: first, we intend to observe not only the near wake but also the far wake, and second the pressure outlet boundary condition is of a reflecting kind. Hence the grid cells are significantly stretched near the outlet in order to dissipate any flow structures and make sure the outlet does not influence the regions of the domain that are studied.

Finally, for the three-dimensional computations, the span length is set to $\pi D$ since this size was shown to be sufficient in previous numerical simulations at the same Reynolds number as explained in the introductory chapter. Furthermore, this better justifies the comparison with numerical results that use this span length. Periodic boundary conditions are chosen to simulate an infinitely wide domain and allow for proper formation of three-dimensional structures, which would be disturbed by a

symmetry type condition for instance.

As indicated previously, the computational code SPARC uses a multi-block structured mesh. The same grids are used in Fluent, only converted to unstructured. Also, for two-dimensional computations, SPARC requires a three-dimensional computational grid with a single cell in the third direction. After a thorough grid study, the two computational grids shown in Figure 3.1 were selected: one for the URANS type simulations and VLES, hereafter called Grid A, and another for the LES studies, Grid B. The structure of both grids are the same, with an o-grid surrounding the cylinder. In the spanwise z-direction, both grids have 33 nodes, while on the x-y planes Grid B is the result of a refinement of Grid A (each edge being divided in two, thus transforming any x-y cell into four cells). The detailed characteristics of both grids are given in Table 3.2. The domain is split into 108 blocks in order to speed up the computation using up to 30 processors with a load balancing between 80% and 100%.

The size of the cells along the cylinder wall in the circumferential direction correspond to a wall value of $c^+$ smaller than 8 for Grid A and smaller than 4 for Grid B, as can be seen in Table 3.2. This value, chosen on the basis of the grid study, is relatively small since even in a LES it can be taken to be close to 20 (usually it is $x^+$ in a purely rectangular geometry); this fact reflects the sensitivity of the average results (in particular drag coefficient and back pressure coefficient) upon which the grid study is based, to the proper resolution of the separation point. The value of $r^+$ (usually $y^+$) is also small and definitely less than unity, which is needed to resolve the boundary layer in its integrity; indeed, some of the turbulence modeling techniques used do not employ a wall model. Finally, the value of $z^+$ is also conservative, since in LES one can usually take 15 and URANS simulations up to 30. Of course all these reference values for the cell sizes in wall variables are empirical and no exact theory determines them, except for the one in the direction perpendicular to the wall and determined by the resolution of the boundary layer.

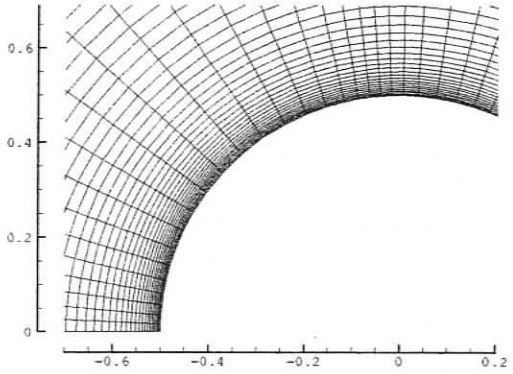


(a) Zoom on Grid A

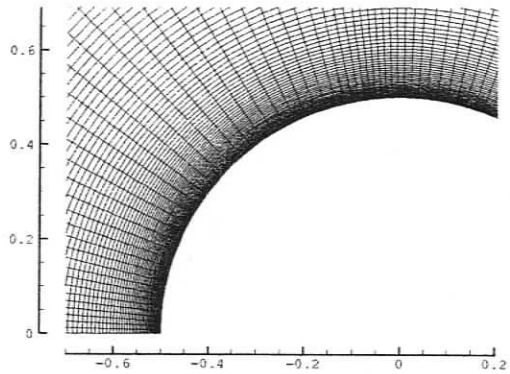


(b) Zoom on Grid B

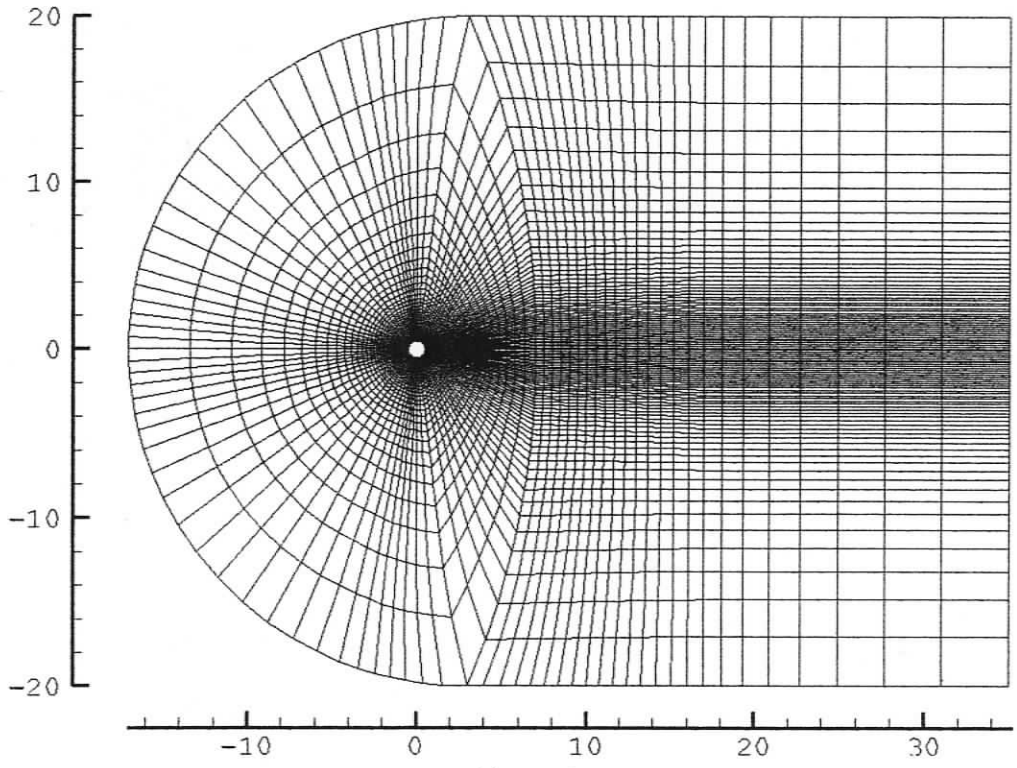


(c) x-y plane

Figure 3.1: Computational grids: x-y planes. Grid A is used for URANS type simulation and VLES, while Grid B is used for LES; both have the same structure on an x-y plane except that Grid B is the result of a refinement of Grid A.

Table 3.2: Characteristics of the computational grids: Grid A for URANS type simulations, Grid B for LES and VLES; $r$ stands for radial, *i.e.* perpendicular to the cylinder wall, and $c$ stands for circumferential, *i.e.* along the cylinder wall.

| **Parameter** | **Grid A 2D** | **Grid A 3D** | **Grid B** |
|---|---|---|---|
| Radial Nodes in O-Section $N_r$ | 65 | | 127 |
| Circumferential Nodes along wall $N_c$ | 145 | | 289 |
| Streamwise Nodes Upstream $N_{x_1}$ | 33 | | 65 |
| Streamwise Nodes Downstream $N_{x_2}$ | 89 | | 177 |
| Transverse Nodes $N_y$ | 97 | | 193 |
| Spanwise Nodes $N_z$ | 2 | 33 | |
| Cells in x-y Plane | 11,520 | | 46,080 |
| Total Cells | 11,520 | 184,320 | 1,474,560 |
| $\Delta c$ along wall $(10^{-3}m)$ | 6.21 - 43.0 | | 3.16 - 21.5 |
| $c^+$ along wall | 0.0902 - 7.446 | | 0.0451 - 3.723 |
| $\Delta r$ at 1st wall cell $(10^{-3}m)$ | 1.953 - 1.97 | | 0.976 - 0.985 |
| $r^+$ at 1st wall cell | 0.028 - 0.340 | | 0.014 - 0.170 |
| $\Delta z$ $(10^{-3}m)$ | *NA* | 98.175 | |
| $z^+$ | *NA* | 1.402 - 17.02 | |

## 3.2 Important Parameters

As indicated in the introduction, the main parameter that characterizes vortex shedding is the Strouhal number defined by

$$St \equiv \frac{f\,D}{U_0} \tag{3.1}$$

where $D = 1$ m is the cylinder diameter, $f$ the shedding frequency in Hertz, and $U_0 = 68.63$ m/s the free-stream velocity. In this study, the Stouhal number is always obtained using the dominant frequency of the Fast Fourier Transform (FFT) of the lift coefficient.

The drag and lift coefficients are probably the two most important parameters used in external flows and are defined by normalizing the drag and lift forces, $\mathcal{D}rag$

and $\mathcal{L}ift$, using the dynamic pressure, which gives the expressions for drag and lift coefficients as

$$c_D \equiv \frac{\mathcal{D}rag}{\frac{1}{2}\rho_0 U_0^2 S} \tag{3.2}$$

and

$$c_L \equiv \frac{\mathcal{L}ift}{\frac{1}{2}\rho_0 U_0^2 S} \tag{3.3}$$

respectively. The denominator is simply the free-stream dynamic pressure $q_0 = \frac{1}{2}\rho_0 U_0^2$ multiplied by the cross-sectional area, $S = LD$, of the cylinder whose length is $L = \pi$. In general, the dynamic pressure is obtained from

$$q \equiv \frac{1}{2}\rho\left(u^2 + v^2 + w^2\right) \tag{3.4}$$

where $\rho$ is the fluid density at the location considered, while $u$, $v$, and $w$ are the velocity components in the streamwise x-direction, transverse y-direction, and spanwise z-direction, respectively.

Because we are running compressible simulation, the results are given in terms of density and energy, and hence a relation is needed to obtain the pressure. The total specific energy, $e$, is the sum of internal energy, which for a calorically perfect gas can be expressed as $u = c_v T$ (where $c_v$ is the specific heat at constant volume), and of the kinetic energy per volume $\frac{1}{2}V^2$ where $V$ is the velocity magnitude, that is

$$e \equiv c_v T + \frac{1}{2}V^2$$

and hence

$$T = \frac{e - \frac{1}{2}V^2}{c_v}.$$

Thus, the ideal gas law $p = \rho R T$ can be written

$$p = \rho R \frac{e - \frac{1}{2}V^2}{c_v}.$$

and hence the pressure can be computed from the total energy and the density through

$$p = (\gamma - 1)\,\rho\left(e - \frac{1}{2}V^2\right). \tag{3.5}$$

where $\gamma = c_p/c_v$ is the ratio of specific heats.

In incompressible flows, the pressure coefficient is set to be unity for the free-stream, and hence is computed from the free-stream and local static pressures, $p_0$ and $p$, as

$$c_{p_{incomp}} \equiv \frac{p - p_0}{\frac{1}{2}\rho_0 U_0^2}. \tag{3.6}$$

Since the flow is compressible in the present simulations, the pressure coefficient is not unity at stagnation: the non-dimensionalisation of the pressure difference is made with respect to the free-stream dynamic pressure, while the density at stagnation will not be equal to the free-stream density. Thus the computation of the pressure coefficient from equation (3.8) does not take into account compressibility effects. We use the Prandlt-Glauert compressibility correction factor $\sqrt{1 - M_0^2}$, where $M_0$ is the free-stream Mach number, to compute the pressure coefficient that would be obtained in a compressible experiment from incompressible measurements through

$$c_{p_{comp}} \equiv \frac{c_{p_{incomp}}}{\sqrt{1 - M_0^2}}. \tag{3.7}$$

In order to be able to compare our compressible simulation results with the incompressible data available in the literature, the pressure coefficient in this study will be computed by

$$c_p \equiv \frac{p - p_0}{\frac{1}{2}\rho_0 U_0^2}\sqrt{1 - M_0^2}. \tag{3.8}$$

The back pressure coefficient, $c_{p_b}$, is the value of the pressure coefficient at the back of the cylinder, *i.e.* the point on the cylinder that is diametrically opposite to the furthest upstream point on the cylinder, this latter being the stagnation point, as illustrated in Figure 3.2.

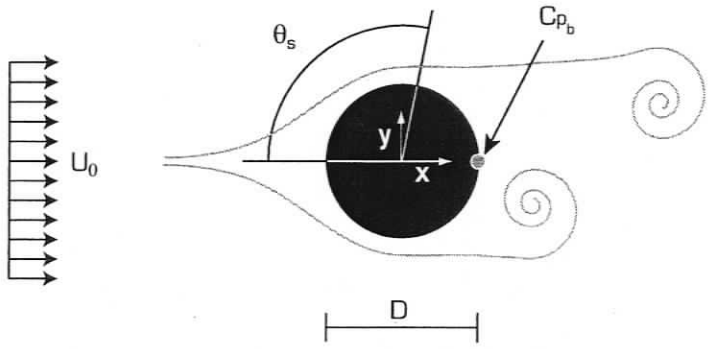


Figure 3.2: Cylinder flow: the separation angle is defined with respect to the negative-x direction. (Image from Gonçalo Pedro, Ph.D. Thesis 2005, University of Victoria, reproduced with permission)

The separation angle, $\theta_s$ is defined as the angle with respect to the negative streamwise direction at which the flow separates from the surface of the cylinder, as illustrated in Figure 3.2. The separation point is the point on the surface of the cylinder where the wall shear stress vanishes, which for our geometry can be written as

$$\theta_s \equiv \left\{ \theta : \mu \left( \frac{\partial u}{\partial y} + \frac{\partial v}{\partial x} \right) = 0 \right\} . \tag{3.9}$$

where the column means "such that".

Another interesting quantity is the vorticity vector $\vec{\omega} = \text{curl}\, \vec{V} = \nabla \times \vec{V}$ which is defined as the curl of the velocity vector $\vec{V} = u\hat{i} + v\hat{j} + w\hat{k}$ and hence has the following components

$$\omega_x = \frac{1}{2}\left( \frac{\partial w}{\partial y} - \frac{\partial v}{\partial z} \right) , \; \omega_y = \frac{1}{2}\left( \frac{\partial u}{\partial z} - \frac{\partial w}{\partial x} \right) , \; \omega_z = \frac{1}{2}\left( \frac{\partial v}{\partial x} - \frac{\partial u}{\partial y} \right) \tag{3.10}$$

of which the out-of-plane, or spanwise, vorticity $\omega_z$ is of particular interest to us.

Finally, the results are given in terms of a non-dimensional time which we define

as

$$t^* \equiv t\,U_0/D. \tag{3.11}$$

where $t$ is the physical time. Non-dimensional quantities are also introduced for the velocity components

$$u^* \equiv u/U_0 \ , \ v^* \equiv v/U_0 \ , \ w^* \equiv w/U_0\,, \tag{3.12}$$

for the density

$$\rho^* \equiv \rho/\rho_0\,, \tag{3.13}$$

for the dynamic pressure

$$q^* \equiv q/q_0\,, \tag{3.14}$$

and the vorticity components

$$\omega_x^* \equiv \omega_x\,D/U_0 \ , \ \omega_y^* \equiv \omega_y\,D/U_0 \ , \ \omega_z^* \equiv \omega_z\,D/U_0\,. \tag{3.15}$$

In a statistical approach, the resolved velocity component in any direction, say for instance $\widetilde{u}$, is decomposed into its time average, $<\widetilde{u}>$, and its time fluctuations, $\widetilde{u}'''$, that is

$$\widetilde{u} = <\widetilde{u}> + \widetilde{u}'''.$$

Then we have

$$\begin{aligned}
<\widetilde{u}^2> &= <(<\widetilde{u}> + \widetilde{u}''')(<\widetilde{u}> + \widetilde{u}''')> \\
&= <<\widetilde{u}>^2 + 2<\widetilde{u}>\widetilde{u}''' + \widetilde{u}'''\widetilde{u}'''> \\
&= <<\widetilde{u}>^2> + <2<\widetilde{u}>\widetilde{u}'''> + <\widetilde{u}'''\widetilde{u}'''> \\
&= <\widetilde{u}>^2 + 2<\widetilde{u}><\widetilde{u}'''> + <\widetilde{u}'''\widetilde{u}'''>
\end{aligned}$$

but

$$< \widetilde{u}'''\widetilde{u}''' >=< \widetilde{u} - < \widetilde{u} >>=< \widetilde{u} > - << \widetilde{u} >>=< \widetilde{u} > - < \widetilde{u} >= 0$$

so

$$< \widetilde{u}^2 >=< \widetilde{u} >^2 + < \widetilde{u}'''\widetilde{u}''' >$$

or equivalently

$$< \widetilde{u}'''\widetilde{u}''' >=< \widetilde{u}^2 > - < \widetilde{u} >^2 .$$

The left-hand side can be computed from the resolved field $\widetilde{u}$, and is simply the square of what is commonly called the *root-mean square* value of $\widetilde{u}$, that is

$$\widetilde{u}^2_{rms} =< \widetilde{u}^2 > - < \widetilde{u} >^2 . \tag{3.16}$$

In the presentation of the results we use the non-dimensionalization

$$U^{*2}_{rms} = \frac{\widetilde{u}^2_{rms}}{U_0^2}. \tag{3.17}$$

In the figures of this chapter, the experimental data `Exp L&S` represented by triangles is from Lourenco & Shih (1993), `Exp G&W` with circles from a private communication of R. Govardhan and C. Williamson (found in Ma *et al.* (2000)) , and `Exp O&W` with squares from Ong & Wallace (1996); the DNS data is from Ma *et al.* (2000), unless otherwise specified. The mean profiles of pressure coefficient and velocity components, and any other x-y fields, are taken at an x-y plane located in the middle of the computational domain.

## 3.3 Influence of Time Step on Stationary Cylinder Simulations

### 3.3.1 Implicit Time Step Selection

In an implicit dual time stepping, the user has to set up the time step by making sure that it remains small compared to the characteristic time scales of the flow motions and that it yields good resolution of the time signals. In order to determine the time step for this study, the following procedure was followed. First, a Runge-Kutta $4^{\text{th}}$ order explicit computation with CFL of unity was carried out on Grid B (the finer to be used) in LES using the Smagorinsky-Lilly model, and explicit time step recorded to be around $\Delta t_{expl} = 4 \times 10^{-6}$.

Now the CFL in a compressible flow is related to the propagation of pressure waves which travel at the local speed of sound, $c$, and hence is given by

$$CFL = \frac{\Delta l}{(|u| + c)\,\Delta t_{expl}} \tag{3.18}$$

where $\Delta l$ is the grid size, $|u|$ the local velocity magnitude, and $\Delta t_{expl}$ the time step; we use the velocity components $u$ only for simplicity, but the relevant direction may be another one. Thus

$$\Delta t_{expl} = \frac{\Delta l}{(|u| + c)\,CFL} \tag{3.19}$$

or, for $CFL = 1$,

$$\Delta t_{expl} = \frac{\Delta l}{|u| + c}. \tag{3.20}$$

The explicit time step for the computation is then the smallest value of $\Delta t_{expl}$ for which the above equation is true at all the cells of the domain, of size $\Delta l$, and in all directions.

In the problem we are considering, the minimum of $\Delta l/(|u| + c)$ occurs on the

cells adjacent to the walls because:

(i) the smallest cells sizes, $\Delta l$, occur at the cylinder wall;

(ii) the flow velocity is reduced near the walls and the inflow Mach number is set to 0.2, such that $|u|$ is at least 5 orders of magnitude smaller than $c$ anywhere in the domain, and hence the value of denominator in (3.20) is always very close to c.

Therefore, the nominator (3.20) determines the location of the minimum. In other word, the value of the time step is determined on the cells near the wall where the flow velocity $|u|$ is small with respect to the local speed of sound $c$, and hence where the incompressible definition

$$CFL = \frac{\Delta l}{|u|\,\Delta t_{expl}},$$

of the CFL number would be more appropriate. Thus one could determine the time step by taking $\Delta t_{expl} = \Delta l/|u|$, such that the determination of $\Delta t_{expl}$ through (3.20) is too small by a factor of $(|u| + c)/|u| = 1 + c/|u| < 6$.

Furthermore, since the flow fluctuations are negligible in the viscous sub-layer which goes up to $n^+ = 5$ (for $n$ the direction perpendicular to the wall), and the first node adjacent to the wall is located at $n^+ \approx 1$, the time step $\Delta t_{expl}$ is too large by a factor of 5. Thus, overall, the time explicit time step for $CFL = 1$ can be multiplied by $6 \times 5 = 30$ without compromising accuracy.

In order to be conservative, it was decided for the present study to multiply $\Delta t_{expl}$ by around 20, and hence the time step chosen for the computations is $\Delta t = 2 \times 10^{-5}$ s $= 0.02$ ms which corresponds to a non-dimensional time step $\Delta t^* = \Delta t\, U_0/D = 1.3726 \times 10^{-3}$.

Table 3.3: Comparison of values for the Strouhal number $St$, average drag coefficient $< c_D >$, back pressure coefficient $< c_{p_b} >$, and separation angle $< \theta_s >$, for two different time steps from three-dimensional simulations using the URANS $k$-$\tau$ Speziale model. The DNS Tremblay results are from Tremblay *et al.* (2000), and the DNS Ma from Ma *et al.* (2000).

| Case | $St$ | $< c_D >$ | $< c_{p_b} >$ | $< \theta_s >$ |
|---|---|---|---|---|
| 0.6 ms | 0.1928 | 1.0038 | −0.7457 | 98.7° |
| 0.02 ms | 0.1967 | 0.9990 | −0.7274 | 98.7° |
| DNS Ma | 0.219 | — | −0.84 | — |
| DNS Tremblay | 0.220 | 1.03 | −0.92 | 94.3° |
| 0.6 ms *w.r.t.* 0.02 ms | −2.0% | 0.5% | 2.5% | 0% |
| 0.6 ms *w.r.t.* DNS Tremblay | −12.3% | −2.5% | 18.9% | −4.7% |
| 0.02 ms *w.r.t.* DNS Tremblay | −10.6% | −3.0% | 20.9% | −4.7% |

### 3.3.2 Effect of Time Step on URANS Simulations

In order to investigate the influence of the time step on the numerical results, three-dimensional URANS simulations with the $k$-$\tau$ Speziale model were carried out both with the selected time step of 0.02 ms ($\Delta t^* = 1.3726 \times 10^{-3}$ when non-dimensionlized) and with a larger time step of 0.6 ms ($\Delta t^* = 41.178 \times 10^{-3}$).

Figure 3.3 shows the lift and drag coefficient signals, $c_L$ and $c_D$, versus non-dimensional time, $t^*$. The finer lines represent the signals for the larger time step, and the difference in lift coefficient is relatively small, the percent difference being maximum at the peaks where it reaches 6%, while the means both vanish. The vanishing of the time-averaged lift is due to the symmetry of both the geometry — hence the flow — and the grid. On the other hand, the drag coefficient is not very sensitive to the time step with a mean difference of 0.5%, the instantaneous difference in signals being also 0.5% between peaks. This percent error is not significant, since much lower than the scatter in data available in the literature, both experimental and numerical.

The Stouhal number is obtained from the dominant frequency of the Fast Fourier

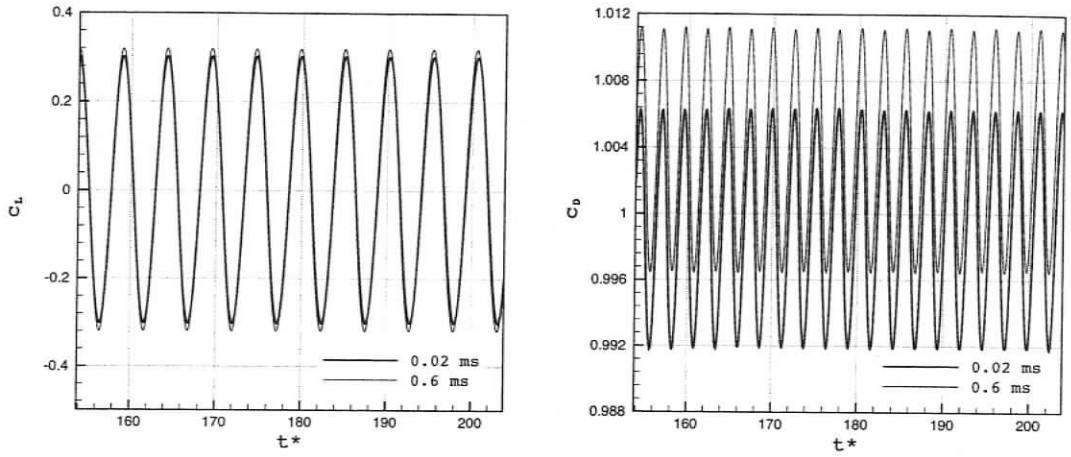


(a) lift coefficient

(b) drag coefficient

Figure 3.3: Lift and drag coefficients versus time for different time steps with the three-dimensional simulations using the URANS $k$-$\tau$ Speziale model. Note: the vertical axis scale is offset between the two signals for increased resolution.

Transform (FFT) of the lift coefficient, which gives $St = 0.1928$ for the larger time step of 0.6 ms and $St = 0.1967$ for the smaller step of 0.02 ms, while the DNS results of Tremblay *et al.* (2000) give $St = 0.220$ and the DNS of Ma *et al.* (2000) yield $St = 0.203$. Hence the error in Strouhal number made when increasing the time step from 0.02 ms to 0.6 ms is only 2%, which is smaller than the 8% difference between the two DNS results. Table 3.3 gathers the average quantities and percent differences.

The difference in mean back pressure coefficient, $< c_{p_b} >$, between the results of the two time steps is of only 2.5%, while the difference in average separation angle, $< \theta_s >$ is indistinguishable. Contrary to the Stouhal number, these two quantities are very sensitive to the resolution of the boundary layer separation and resulting vortex shedding, and yet they reveal only small differences between simulations with the different time steps studied and with DNS and experimental data, as can be seen from the percent differences in Table 3.3.

Thus, changing the time step from 0.02 ms to 0.6 ms in the URANS $k$-$\tau$ Speziale simulation has a negligible influence on the Strouhal number, average drag coeffi-

cient, back pressure coefficient, and the separation angle, which is consistent with the principle behind URANS type simulations, and the associated turbulence models, in which average quantities are usually resolved quite satisfactorily.

It is important to note that the frequency of the lift coefficient is half that of the drag coefficient, because of the physics of vortex shedding, both lift and drag resulting from the transfer of momentum to the shed vortices. However, two vortices are shed per cycle, and the shedding of each one of these vortices contributes to a positive drag, while one vortex shedding contributes to a negative lift (the one shed from the upper surface) and the other gives a positive lift (the one shed from the lower surface). Thus, during a lift period, at the maximum lift a vortex is shed from the lower surface and this gives a maximum drag; and at the minimum lift a vortex is shed from the lower surface giving another maximum in drag.

More sensitive is the average pressure coefficient on the cylinder wall, which is shown in Figure 3.4. The maximum error with respect to the DNS data for the simulations at the two time steps considered is 12.5% for 0.6 ms and 6% for 0.002 ms, while the two time steps results differ by 6% — this maximum difference always occur at the minimum pressure and hence at separation. Yet the integration of the pressure coefficient yields lift and drag average values that are very similar for the two time steps. However, the shape of the pressure coefficient curves on the cylinder wall are not the same: the 0.02 ms curve (solid line in the figure) is flatter at the back of the cylinder ($\theta = 180°$) and hence closer in shape to that from the DNS by Ma *et al.* (2000). On the other hand, the curve for 0.6 ms has a relatively important peak at cylinder back, the difference between the peak value at $\theta = 180°$ and the flat part at $\theta = 145°$ being of 11%; this indicates that the simulation carried out with the larger time step is unable to properly capture all the unsteady separation phenomena and recirculation. Furthermore, the results with the larger time step undershoot the $< c_p >$ DNS data at the separation points depicted by the differences in minima of the curves around $\theta = 80°$: 12.5% difference in the 0.6 ms results and 6% in the 0.02

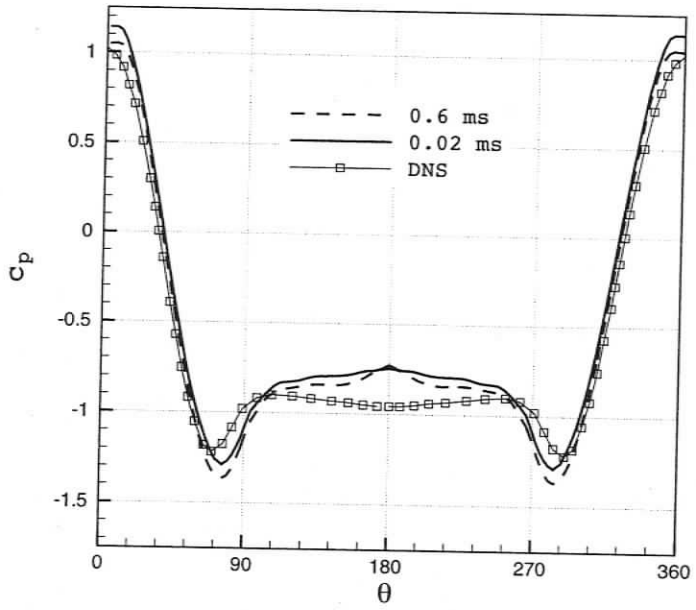


Figure 3.4: Average pressure coefficient on the cylinder surface with two different time steps for the three-dimensional simulations using the URANS $k$-$\tau$ Speziale model. The DNS data is from Ma *et al.* (2000).

ms results with respect to the DNS data. Thus, in spite of the small differences, the 0.02 ms for the dual time step is a better choice than 0.6 ms.

Figure 3.5 shows the evolution of the mean longitudinal velocity, $U^* = < u > /U_0$, along the centerline $y = 0$. The comparison of centerline velocity components is seldom presented in the literature, and depicts the largest differences in velocity — since as the reader can see in the velocity profiles of the following figures, the largest scatter in data always occurs at the centerline. Three experimental sets (triangles `Exp L&S` by Lourenco & Shih (1993), circles `Exp G&W` from a private communication of R. Govardhan and C. Williamson (found in Ma *et al.* (2000)), squares `Exp O&W` by Ong & Wallace (1996)) as well as the DNS data by Ma *et al.* (2000) are shown, together with the results from the two time steps under consideration.

The differences within experimental results and between experimental and DNS

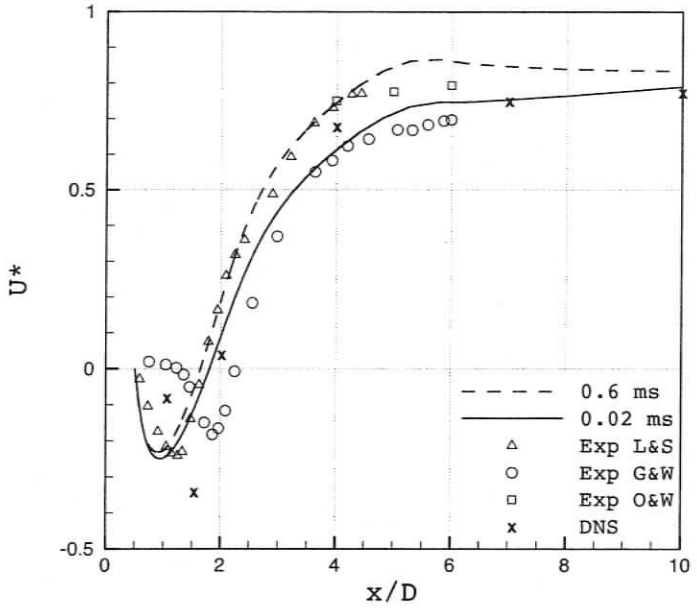


Figure 3.5: Average streamwise velocity component $U^* =< u > /U_0$ along the centerline $y = 0$ with two different time steps for the three-dimensional simulations using the URANS $k$-$\tau$ Speziale model; triangles `Exp L&S` by Lourenco & Shih (1993); circles `Exp G&W` from a private communication of R. Govardhan and C. Williamson (found in Ma *et al.* (2000)); squares `Exp O&W` by Ong & Wallace (1996); DNS data by Ma *et al.* (2000).

data is often larger than the differences between the two simulations, which makes it hard to conclude, only from the longitudinal velocity, which time step is more appropriate. Nevertheless, one can venture to consider the lower time step to be better for the following three reasons, in addition to the indications from the pressure coefficient. First, the minimum in $U^*$ is lower for the smaller time step and closer to the DNS and Lourenco & Shih (1993) experimental minima. Second, the 0.6 ms results definitely overshoot all other data, while the 0.02 ms results seem to be located in between extreme experimental data. Third, the smaller time step gives a smoother curve, while the curve for the larger time step depicts a change from increasing to decreasing around $x/D = 5.5$ which is not visible in any of the other data set.

The longitudinal velocity from the smaller time step is larger than the one from the smaller time step all along the wake. This can be explained as follows: a larger time step resolves fewer frequencies and hence the total energy, which is conserved, is spread among fewer modes; the dominant modes that are resolved carry out a relatively larger amount of energy when the time step is larger, thus larger momentum *i.e.* larger average velocity.

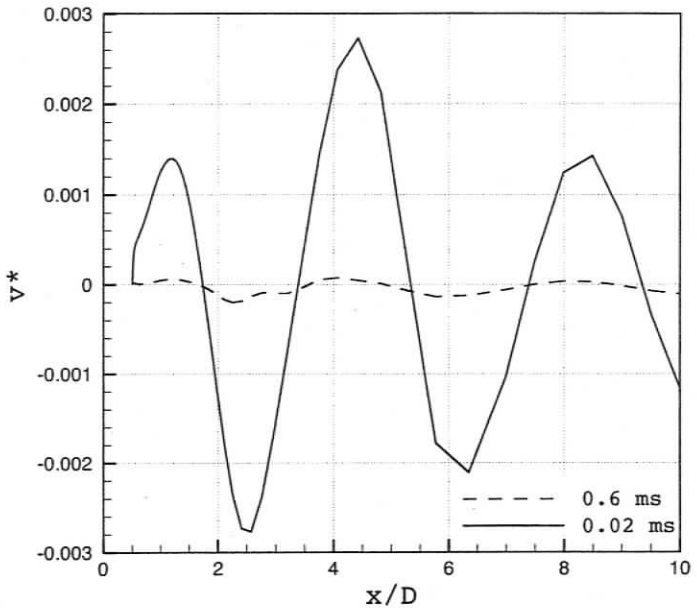


Figure 3.6: Average transversal velocity component $V^* =< v > /U_0$ along the centerline $y = 0$ with two different time steps for the three-dimensional simulations using the URANS $k$-$\tau$ Speziale model.

With respect to the transversal velocity, $V^* =< v > /U_0$, along the centerline shown in Figure 3.6, one can note that the amplitude of the component from the simulation with the smaller time step is much larger than the one obtained using the larger time step. A larger time step tends to be more dissipative, similarly to a coarser grid, and hence smaller variations in the transversal component are obtained. Yet, the transversal velocity component normalized by the longitudinal free-stream

velocity is quite small (lower than 0.3%) in any case, and the two curves undulate in a similar manner.

Figure 3.7 shows the longitudinal velocity profiles at different streamwise locations along the wake. Overall, the smaller time step is closer to the dynamics seen in the experimental and DNS data, even though the amplitude of the differences are not of the same order of magnitude at all the locations. In the very near wake, at $x/D = 1.06$, both time steps results are very close to the experimental data, with differences of less than 12%, but relatively far from the DNS results. As we move farther downstream, the curve for 0.02 ms gets closer and closer to the experimental and DNS ones while the one for the larger time step keeps higher centerline values.

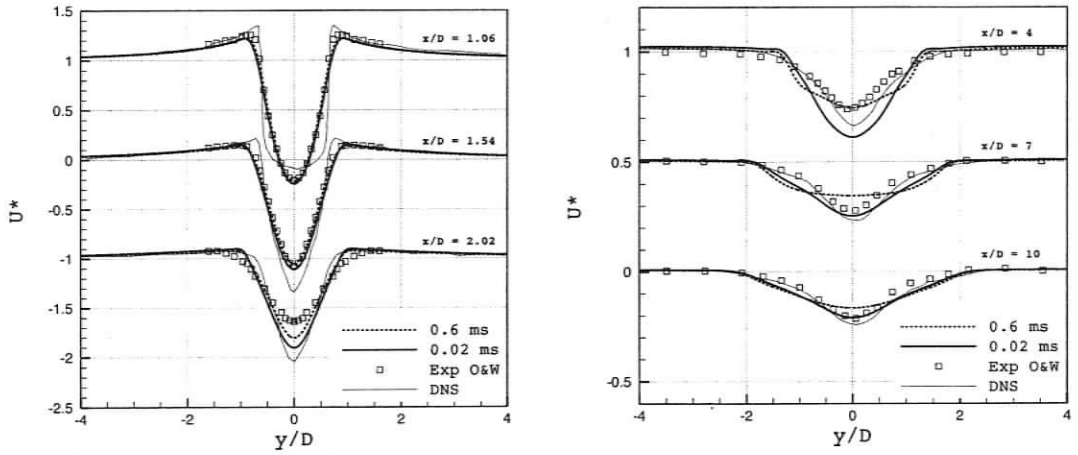


(a) (b)

Figure 3.7: Profiles of average streamwise velocity component $U^* =< u > /U_0$ at different streamwise locations, with two different time steps for the three-dimensional simulations using the URANS $k$-$\tau$ Speziale model.

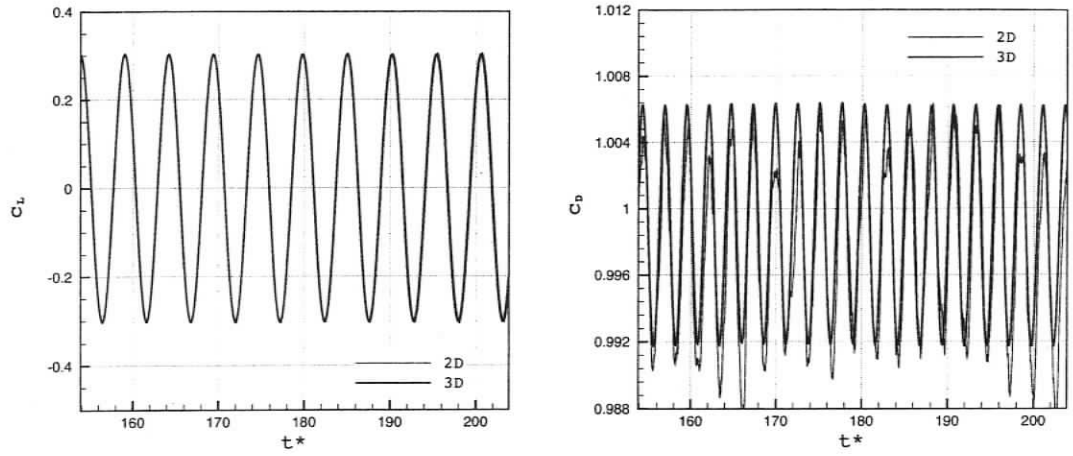


(a) lift coefficient

(b) drag coefficient

Figure 3.8: Lift and drag coefficients versus time for two- and three-dimensional simulations using the URANS $k$-$\tau$ Speziale model.

## 3.4 Two- Versus Three-Dimensional URANS Simulations

In this section we shall examine the differences between two- and three- dimensional simulations using the URANS $k$-$\tau$ Speziale model with a time step of 0.02 ms, for the simulation of the flow around a stationary cylinder at $Re_D = 3900$.

The difference in lift coefficient between two- and three-dimensional simulations is almost negligible, the maximum difference of the 2D with respect to the 3D being only 0.1%. This can be seen in Figure 3.8. On the other hand, the drag signal of the 2D simulation retains periodicity but is very irregular in amplitude and shape, which is rather unexpected from a URANS type simulation and suggests that the 2D computation has difficulties resolving the average motion properly, especially given the fact that such a behavior in not observed in the 3D case.

In spite of this, the Strouhal number, the average drag and back pressure coefficients, and the separation angle obtained from 2D and 3D simulations differ by

Table 3.4: Comparison of average values for the Strouhal number $St$, drag coefficient $< c_D >$, back pressure coefficient $< c_{p_b} >$, and separation angle $< \theta_s >$, for two- and three-dimensional simulations using the URANS $k$-$\tau$ Speziale model. The DNS Tremblay results are from Tremblay *et al.* (2000), and the DNS Ma from Ma *et al.* (2000).

| Case | $St$ | $< c_D >$ | $< c_{p_b} >$ | $< \theta_s >$ |
|---|---|---|---|---|
| 2D | 0.1914 | 1.0013 | −0.7419 | 98.7° |
| 3D | 0.1928 | 1.0038 | −0.7274 | 98.7° |
| DNS Ma | 0.219 | — | −0.84 | — |
| DNS Tremblay | 0.220 | 1.03 | −0.92 | 94.3° |
| 2D *w.r.t.* 3D | −0.7% | −0.2% | −2.0% | 0% |
| 2D *w.r.t.* DNS Tremblay | −1.3% | −2.8% | −19.4% | −4.7% |
| 3D *w.r.t.* DNS Tremblay | −12.4% | −2.5% | 20.9% | −4.7% |

less than 2% and are accurate when compared to experimental and DNS results, with an error smaller than 20%, as detailed in Table 3.4. This confirms the relative insensitivity of these average parameters to three dimensional resolution.

The variation of average pressure coefficient, $< c_p >$, reveals a more important difference between 2D and 3D simulations. There is a clear overshoot of $\overline{c_p}$ on the back of the cylinder in the 2D simulations, along with a peak (discontinuous slope) at the centerline, which is not present in the 3D results nor in the DNS data. As it was the case for too large a time step, the 2D simulations appears unable to properly capture the dynamics of the flow at the centerline, even though average quantities such as Stouhal number and average drag coefficient are quite accurate even in 2D.

The difference between 2D and 3D simulations in the evolution of streamwise velocity component along the centerline is less important than what it was between the two time steps considered in the previous section, the relative difference being smaller than the scatter between experimental data and between numerical and experimental results: there is as much as 25% difference between the experimental data by Lourenco & Shih (1993) and that by R. Govardhan and C. Williamson (found in Ma *et al.*

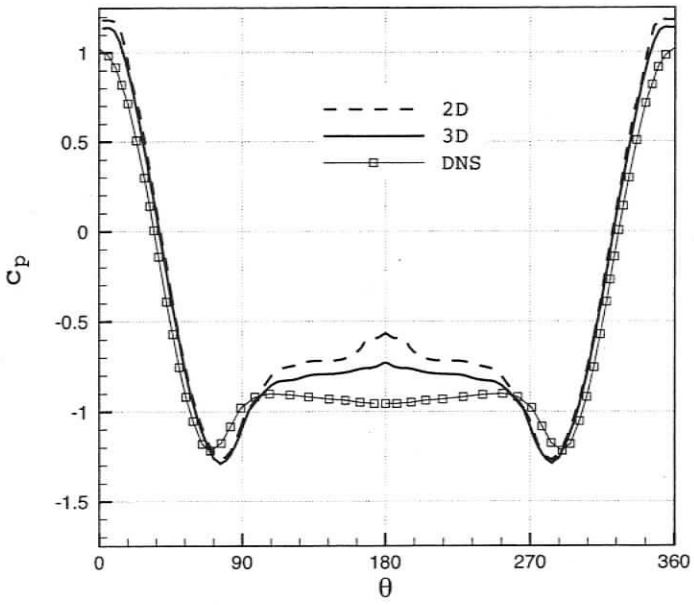


Figure 3.9: Average pressure coefficient on the cylinder surface for two- and three-dimensional simulations using the URANS $k$-$\tau$ Speziale model. The DNS data is from Ma *et al.* (2000).

(2000)). As was seen in the comparison of the two time steps, the curve for the 2D results changes from increasing to decreasing around $x/D = 5.5$ back to increasing again close to $x/D = 7$, while the other curves do not exhibit any change in slope sign after the one occurring in the very near wake close to $x/D = 1$ at the border of the recirculation zone.

The average transverse velocity component, $V^* =< v > /U_0$, exhibits important variations along the centerline for both 2D and 3D simulations, but the variation in the 3D data is much more important than the one in the 2D results, with a difference in amplitude between the two of around 56%. However, the amplitudes remain below 0.3% of the free-stream velocity.

Since the differences between two- and three-dimensional computations seem to

be significant even in URANS simulations, the comparison between the different turbulence modeling technique will be done using only three-dimensional simulations.

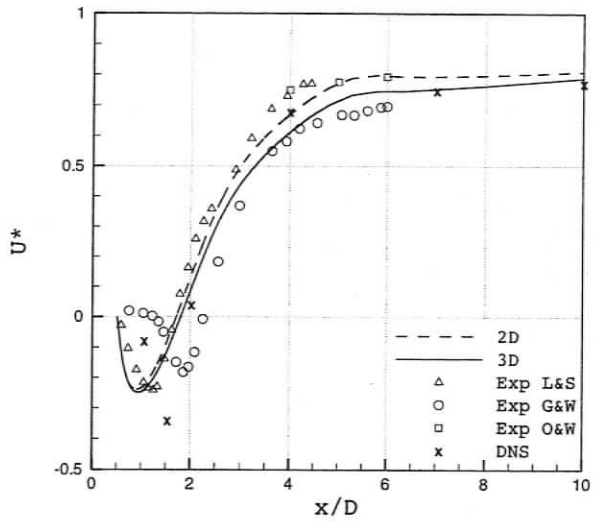


Figure 3.10: Average streamwise velocity component $U^* = < u > /U_0$ along the centerline $y = 0$ for two- and three-dimensional simulations using the URANS $k$-$\tau$ Speziale model.

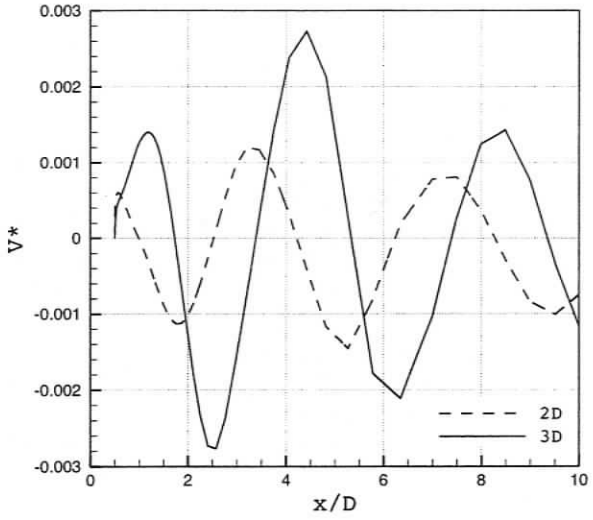


Figure 3.11: Average transversal velocity component $v^* =< v > /U_0$ along the centerline $y = 0$ for two- and three-dimensional simulations using the URANS $k$-$\tau$ Speziale model.

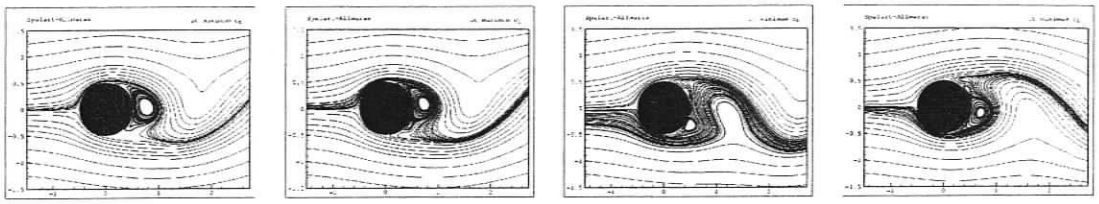

(a) SA at max $c_D$ (b) SA at max $c_L$ (c) SA at min $c_D$ (d) SA at min $c_L$

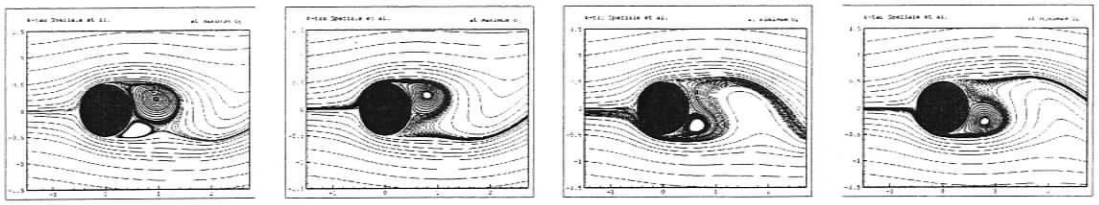

(e) Sp at max $c_D$ (f) Sp at max $c_L$ (g) Sp at min $c_D$ (h) Sp at min $c_L$

Figure 3.12: Instantaneous streamlines past a static circular cylinder at $Re_D = 3900$: comparison of URANS models Spalart-Almaras (left) and k-$\tau$ Speziale et al. (right).

## 3.5 Influence of Turbulence Modeling Technique on Stationary Cylinder Simulations

### 3.5.1 URANS Simulations

As previously, the figures of this section are taken at the x-y plane located in the middle of the computational domain, and the experimental data `Exp L&S` is from Lourenco & Shih (1993) and represented by triangles, `Exp G&W` with circles from a private communication of R. Govardhan and C. Williamson (found in Ma *et al.* (2000)) , and `Exp O&W` with squares from Ong & Wallace (1996); the DNS data is from Ma *et al.* (2000), unless otherwise specified

#### Instantaneous Fields

The instantaneous streamlines of Figure 3.12 show the flow at times of maximum and minimum drag and lift. The maximum drag and lift images are very close in time, and show the growth of the vortex that develops from the upper surface. On the

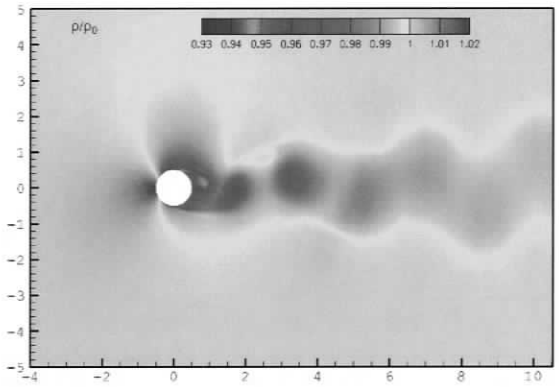


(a) SA $\rho/\rho_0$ at max $c_D$

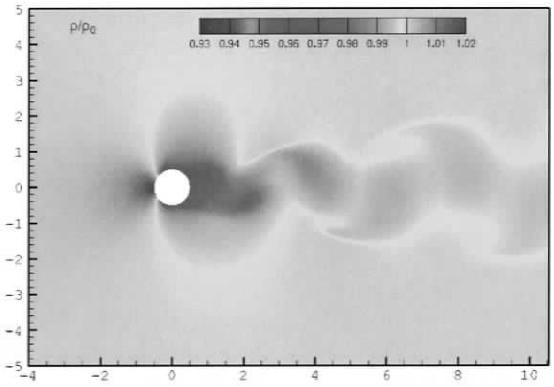


(b) Sp $\rho/\rho_0$ at max $c_D$

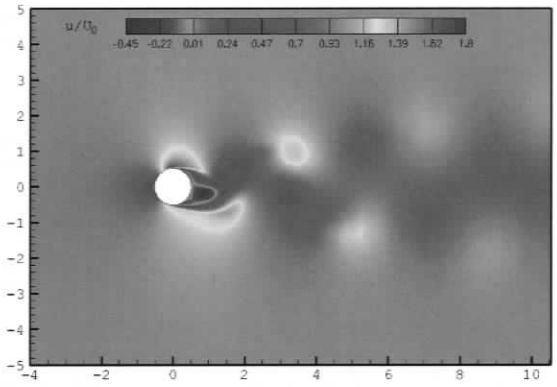


(c) SA $u/U_0$ at max $c_D$

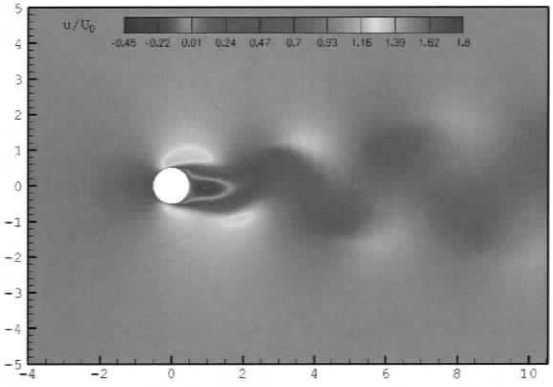


(d) Sp $u/U_0$ at max $c_D$

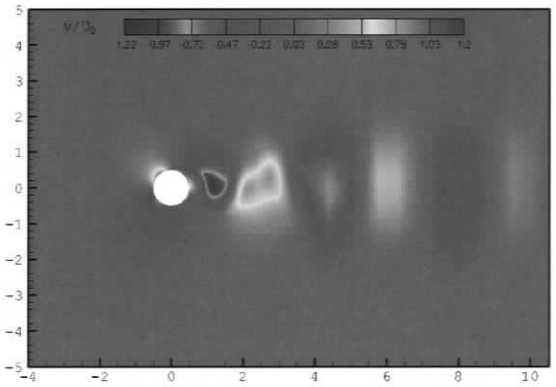


(e) SA $v/U_0$ at max $c_D$

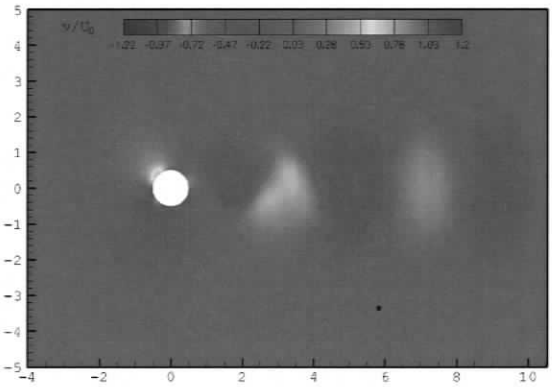


(f) Sp $v/U_0$ at max $c_D$

Figure 3.13: Instantaneous non-dimensional density, longitudinal and normal velocity components for the flow past a static circular cylinder at $Re_D = 3900$ at time corresponding to a local maximum in $c_D$: comparison of URANS models Spalart-Almaras (left) and k-$\tau$ Speziale et al. (right).

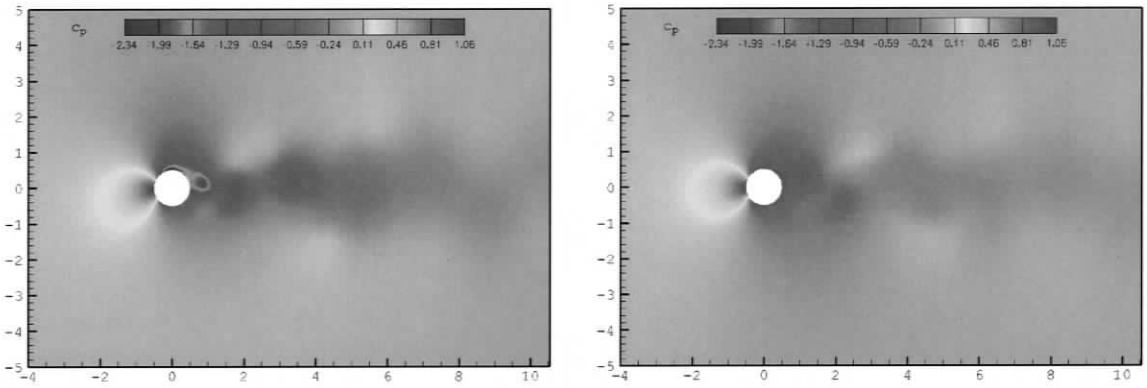

(a) SA $c_p$ at max $c_D$



(b) Sp $c_p$ at max $c_D$

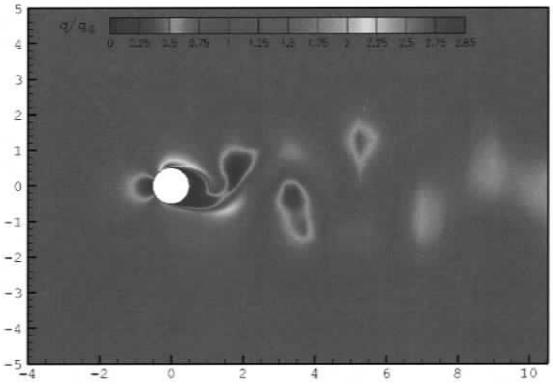

(c) SA $q/q_0$ at max $c_D$

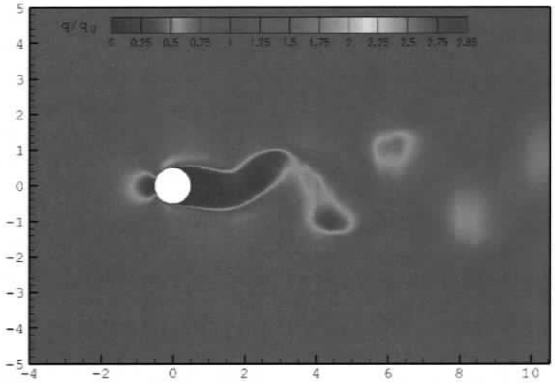

(d) Sp $q/q_0$ at max $c_D$

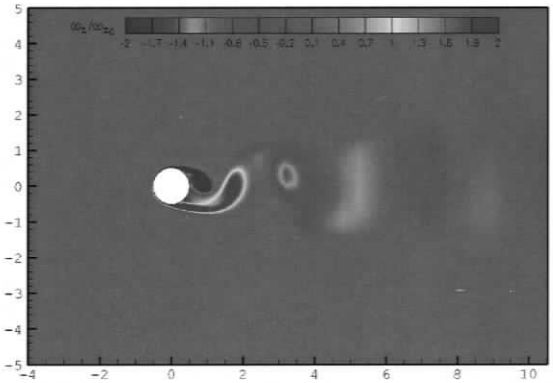

(e) SA $\omega_z D/U_0$ at max $c_D$

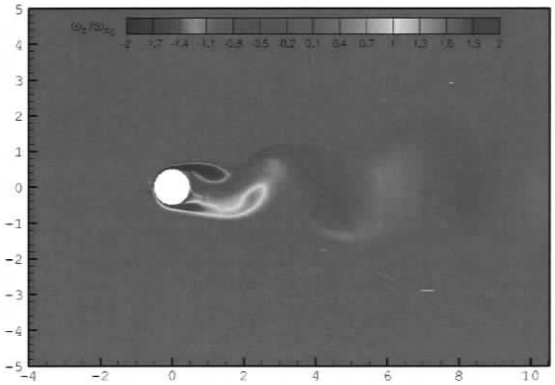

(f) Sp $\omega_z D/U_0$ at max $c_D$

Figure 3.14: Instantaneous pressure coefficient and non-dimensional dynamic pressure for the flow past a static circular cylinder at $Re_D = 3900$ at the time corresponding to a local maximum in $c_D$: comparison of URANS models Spalart-Almaras (left) and k-$\tau$ Speziale et al. (right).

other hand, during minimum drag and lift, the lower vortex is growing.

Figures 3.13 and 3.14 show the instantaneous fields of density, streamwise and transversal velocities, pressure coefficient, dynamic pressure, and out-of-plane vorticity at the time corresponding to maximum drag.

The density field shows a 7% maximum variation with respect to the free-stream density, and as expected the maximum change in density occurs in the boundary layer where density decreases due to important velocity gradients caused by viscous effects. This fact prohibits the use of incompressible turbulence models for this flow — even though the Mach number is low enough that in practice the flow can be considered incompressible — since the modeling is very important in regions where the density changes need to be taken into account, *i.e.* boundary and shear layers.

On the other hand, the largest increase in density occurs at the stagnation point where the increase reaches 2%. In an ideal compressible gas, the change in density is due to pressure and temperature variations: from the pressure and temperature fields of Figure 3.15 for the $k$-$\tau$ model, for instance at the stagnation point, both pressure and temperature changes are of 1%, and add up to a change in density of 2%. This is in agreement with the energy equation of an ideal gas which states that, for an isentropic flow and hence along the streamline upstream of the cylinder until the stagnation point

$$c_p T + \frac{1}{2} V^2 = constant; \tag{3.21}$$

thus at the stagnation point where the velocity vanishes,

$$c_p T_0 + \frac{1}{2} U_0^2 = c_p T_{stag}; \tag{3.22}$$

where the subscript 0 denotes free-stream values; then

$$\frac{T_{stag}}{T_0} = 1 + \frac{1}{2} \frac{U_0^2}{c_p T_0} \approx 1.01; \tag{3.23}$$

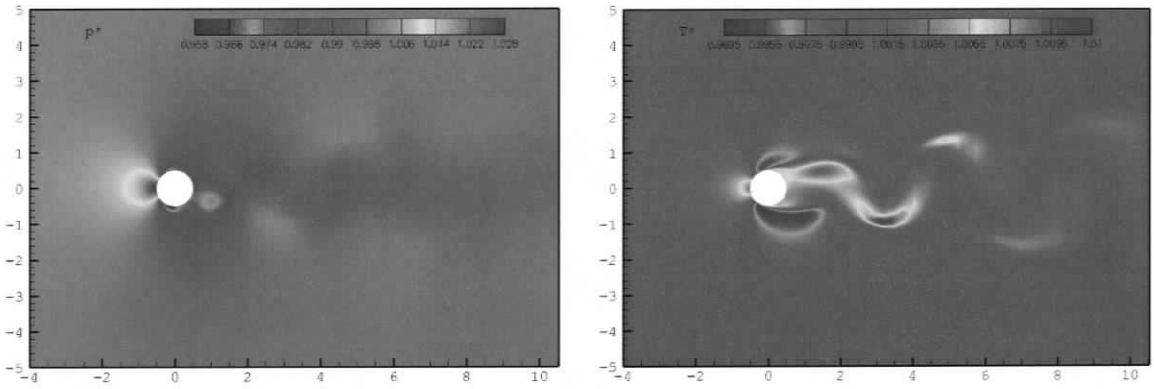

(a) $p^* = p/p_0$ (b) $T^* = T/T_0$

Figure 3.15: Instantaneous non-dimensional pressure and temperature fields, $p^* = p/p_0$ and $T^* = T/T_0$ for the simulation with the $k$-$\tau$ Speziale model.

and hence indeed the variation in temperature at the stagnation point represents 1% of the free-stream temperature.

The distinctive pattern of alternating vorticity generation and shedding is clearly illustrated in Figure 3.13 with negative vorticity and clock-wise rotating vortex on the upper surface, and positive vorticity with counter-clockwise rotation on the lower surface. The vortex that develops on the upper surface of the cylinder is growing while the vortex from the lower surface is being shed.

### Time Averaged Fields

The time averaged streamlines for the two URANS simulations are shown in Figure 3.16. The most obvious difference between the two models is the difference in recirculation length: the Spalart-Allmaras model predicts a recirculation length $L_r/D = 0.97$, while the $k$-$\tau$ Speziale model gives $L_r/D = 1.64$. For comparison, the recirculation length is 1.59 in the DNS by Ma *et al.* (2000) and 1.30 in the one by Tremblay *et al.* (2000). Hence, the $k$-$\tau$ Speziale model gives a recirculation length that differs by only 3% with respect to the DNS data from Ma *et al.* (2000). On the other hand, the Spalart-Allmaras is tailored for aerodynamic flows where separation

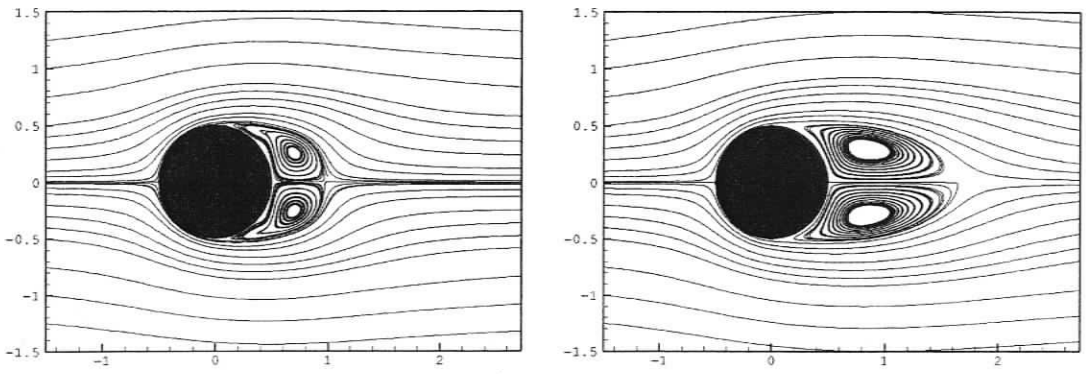

(a) Spalart-Allmaras (b) $k-\tau$ Speziale et al.

Figure 3.16: Average streamlines past a static circular cylinder at $Re_D = 3900$: comparison of URANS models Spalart-Almaras (left) and k-$\tau$ Speziale et al. (right).

regions are relatively small, such as in the flow past an airfoil, and hence is likely to inadequately resolve separation regions which could explains why the recirculation zone is too small. This is confirmed by the analysis of the fields from which it can be seen that the magnitudes of properties such as velocity components and density are larger than for the $k$-$\tau$ Speziale model but are dissipated faster.

This difference in recirculation lengths is consistent with the difference in separation angle between the two models: the boundary layer in the Spalart-Allmaras simulation remains attached longer to the cylinder (larger separation angle) and hence yields a smaller recirculation zone than the simulation from the $k$-$\tau$ model which predicts an earlier separation. Thus it seems that an important limitation of the Spalart-Allmaras model is that it does not predict separation properly, this fact being underlined in the paper by Spalart & Allmaras (1994) who advised against the use of their model to predict the boundary layer's transition to turbulence and separation.

Let us now look at the density field of Figure 3.17. Both URANS turbulence models studied yield a similar density field, except that the Spalart-Allmaras model predicts the existence of a larger high-density region in the front of the cylinder at the approach of the stagnation point, while the $k$-$\tau$ model yields only a circular

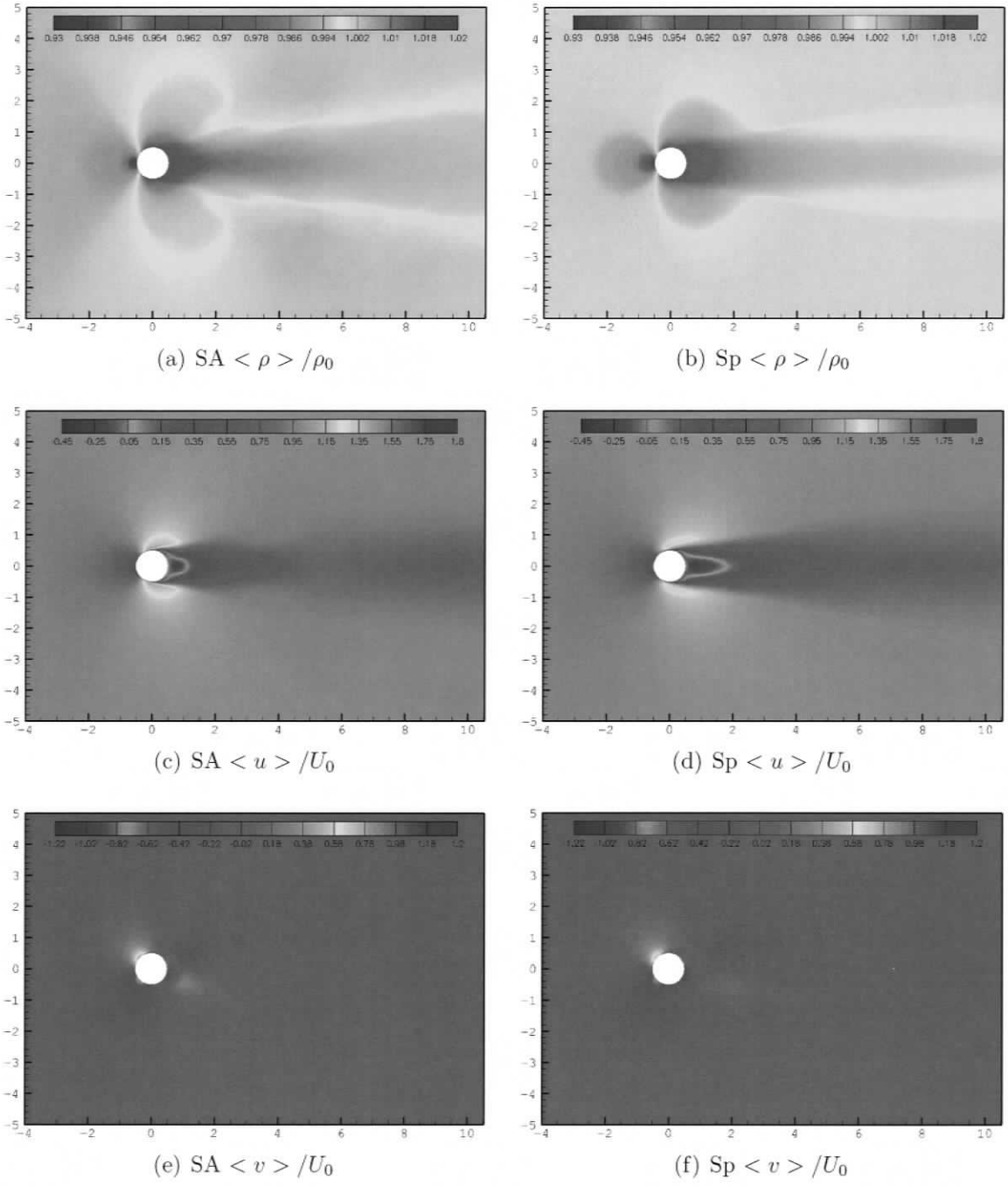

(a) SA $< \rho > /\rho_0$ (b) Sp $< \rho > /\rho_0$

(c) SA $< u > /U_0$ (d) Sp $< u > /U_0$

(e) SA $< v > /U_0$ (f) Sp $< v > /U_0$

Figure 3.17: Time average non-dimensional density, longitudinal and normal velocity components for the flow past a static circular cylinder at $Re_D = 3900$ at time corresponding to a local minimum in $c_L$: comparison of URANS models Spalart-Almaras (left) and k-$\tau$ Speziale et al. (right).

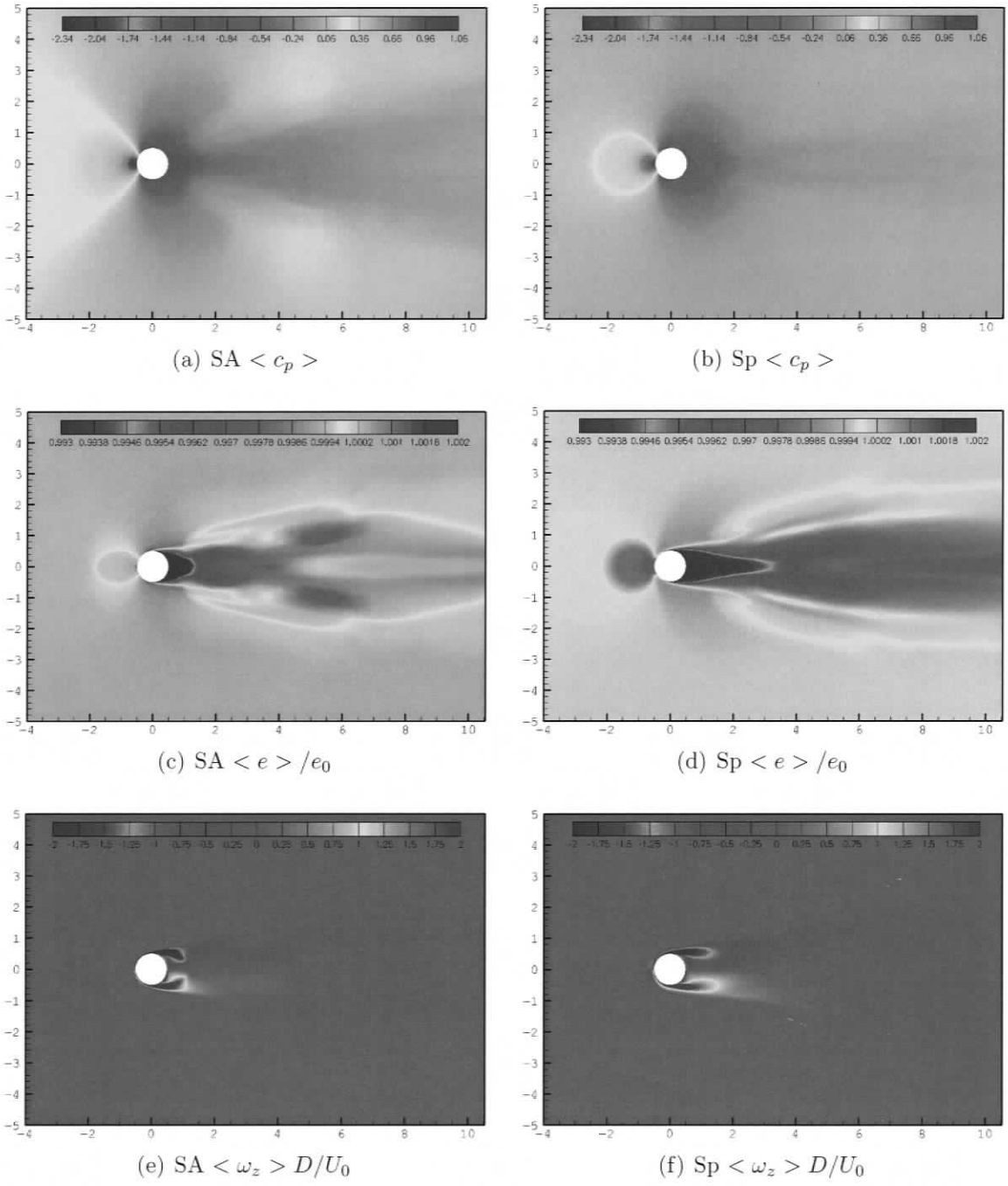

(a) SA $< c_p >$ (b) Sp $< c_p >$

(c) SA $< e > /e_0$ (d) Sp $< e > /e_0$

(e) SA $< \omega_z > D/U_0$ (f) Sp $< \omega_z > D/U_0$

Figure 3.18: Time average pressure coefficient, energy, and out-of-plane vorticity for the flow past a static circular cylinder at $Re_D = 3900$ at the time corresponding to a local minimum in $c_L$: comparison of URANS models Spalart-Almaras (left) and k-$\tau$ Speziale et al. (right).

high-density zone (dark orange and red). Furthermore, a light blue region of very low mean density is visible only in the Spalart-Allmaras results on the back of the cylinder, which may be linked to the short but intensive recirculation zone.

What seem to be due to excessive dissipation, but is in fact caused by the delay in separation of the Spalart-Allmaras model, is found again in the streamwise velocity fields, where the recirculation zone on the back of the cylinder (blue in the figure) is much smaller for the Spalart-Allmaras simulations than for the $k$-$\tau$ Speziale results, as was already observed in the streamline images. The magnitude of the velocity is larger on the sides of the cylinder for the one-equation model, so that in spite of the smaller extents the overall energy from both models is similar.

In the problem of the flow past a circular cylinder in the sub-critical regime, most of the drag comes from the pressure drag while friction drag makes only a very small contribution — which of course does not mean that viscous effects on drag are negligible; on the contrary, it is because of the viscous effects that the flow separates and the formation of the resulting low pressure zone on the back of the cylinder is responsible for most of the drag. From the observation of the pressure coefficient fields of Figure 3.18, one can readily see that the drag forces obtained with the two URANS models will be quite different, and that the Spalart-Allmaras model will yield larger drag. Indeed, in the simulations that use the Spalart-Allmaras model, an important low pressure zone on the back of the cylinder can be observed, while the high pressure zone around the stagnation point seems to be similar in the results from the two models. This will be confirmed by the pressure coefficient variation along the cylinder wall.

The energy fields are shown in Figure 3.18. The change in energy is very small (less than 0.7%) in all regions as expected, with largest deficits in the recirculation zone. Some energy is also lost near the stagnation point, while an increase in energy is observed near the front of the cylinder which is most likely due to an energy transfer coming from the stagnation region of the flow. Since the recirculation zone is smaller

in the simulation with the Spalart-Allmaras model, the low energy region of the flow is shorter than with the $k$-$\tau$ model, while the middle and far wake regions exhibiting a loss in energy are wider. Finally, the field that reaches the cylinder in the Spalart-Allmaras carries more energy (darker orange), as if the far-field 0.3% turbulence level had been dissipated less by the Spalart-Allmaras model than by the $k$-$\tau$ Speziale model.

In the average out-of-plane vorticity fields, the difference in size of the recirculation zone from the simulation with the two URANS models is once again clear. Yet, the vorticity amplitudes are similar, with the Spalart-Allmaras model resulting in an abrupt end of vorticity, while in the $k$-$\tau$ Speziale model the vorticity smoothly decreases and the high vorticity contours are rounded at the end.

### Average Quantities

Table 3.5 gives the Strouhal number of vortex shedding, the average drag and back pressure coefficients, and average separation angle obtained from the simulations using the four different turbulence modeling techniques considered here. The lift and drag signals for both URANS models in three-dimensional simulations are sinusoidal, and hence shall not be shown.

The pressure coefficient on the cylinder wall can be seen in Figure 3.19(a). Compared to the DNS data by Ma *et al.* (2000), the Spalart-Allmaras model significantly under-predicts the pressure after separation which is also reflected in the low value of the back pressure coefficient in Table 3.5; thus, the Spalart-Allmaras model over-predicts drag by 25%. The lower back pressure is consistent with the significantly shorter mean recirculation bubble in Figure 3.16. On the contrary, the $k$-$\tau$ Speziale over-predicts pressure past separation. In spite of this, the curve for the $k$-$\tau$ Speziale model remains relatively close to the DNS one, and hence when integrated the resulted drag coefficient is accurate to 3%, slightly under-predicted due to the over-prediction

Table 3.5: Comparison of the simulation results from the different models used, for the case of a static cylinder at $Re_D = 3900$. The percents represent errors with respect to the DNS results by Tremblay *et al.* (2000).

| **Type** | **Model** | $St$ | $< c_D >$ | $< c_{p_b} >$ | $< \theta_s >$ |
|---|---|---|---|---|---|
| DNS | none | 0.220 | 1.03 | $-0.92$ | 94.3° |
| URANS | Spalart-Allmaras | 0.2183 | 1.2922 | $-1.2404$ | 103.5° |
| | | (-0.8%) | (25.5%) | (-34.8%) | (9.8%) |
| URANS | $k-\tau$ Speziale | 0.1967 | 0.9990 | $-0.7274$ | 98.7° |
| | | ($-10.6\%$) | ($-3.0\%$) | (20.9%) | (4.7%) |
| LES | Smagorinsky-Lilly | 0.1967 | 1.3302 | $-1.4087$ | 92.5° |
| | | ($-10.6\%$) | (29.1%) | ($-53.1\%$) | (-1.9%) |
| VLES | adaptive $k-\tau$ | 0.2113 | 1.3287 | $-1.3706$ | 100.0° |
| | | ($-3.9\%$) | (29.0%) | ($-49.0\%$) | (6.0%) |

of negative back pressure.

In the front of the cylinder, both models give similar pressure coefficients. Thus, the excessive drag predicted by the Spalart-Allmaras model comes from an underestimation of the pressure on the back of the cylinder and not from an overestimation of the pressure on the front. The reader is reminded that the pressure coefficient is not unity at stagnation because of the compressibility effects.

While the pressure coefficient explains the difference in drag, the friction coefficient will determine the location of the separation point and be a good indication of the ability of the model to capture the dynamics of the boundary layer and recirculation regions. Both URANS models significantly over-estimate the friction coefficient with respect to the LES simulation with the dynamic model by Breuer (1998). Before separation, this can be explained as an inability of both URANS models to properly resolve the boundary layer physiscs, which is confirmed by the fact that the difference with Breuer becomes less significant past the separation point. Because the boundary layer on the cylinder remains laminar and since the Spalart-Allmaras model is based on the boundary layer logarithmic law, this one-equation models seems to perform

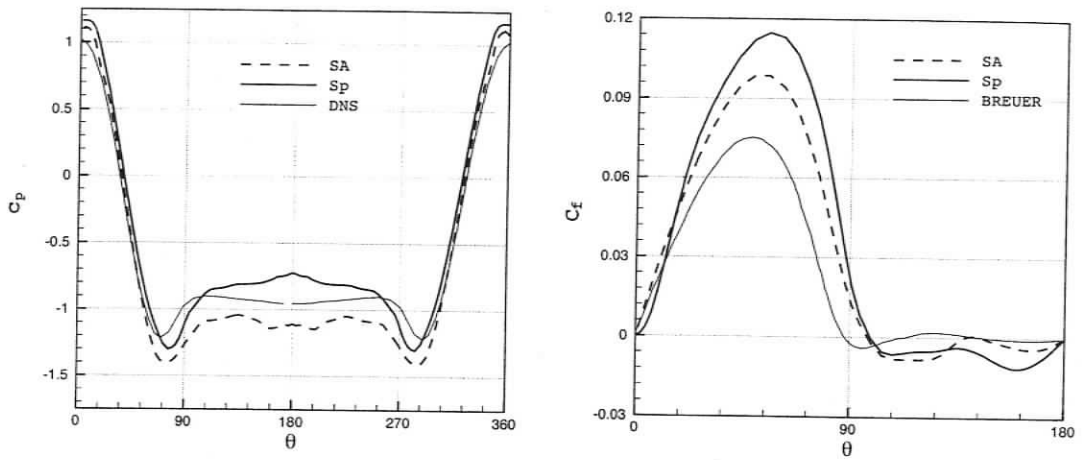


(a) $< c_p >$ (b) $< C_f >$

Figure 3.19: Average pressure coefficient on the cylinder surface for three-dimensional simulations. DNS data is from Ma *et al.* (2000) and BREUER is a LES with the dynamic Smagorinsky model from Breuer (1998).

better than the $k$-$\tau$ Speziale model.

When comparing the streamwise velocity profiles, which are shown in Figure 3.20, each model performs better than the other in different regions, and contrary to the DNS data all the profiles observed here have a V-shape. Inside the recirculation zone, at $x/D = 1.06$ and 1.54, the profiles from the $k$-$\tau$ Speziale model are very close to the experimental data, contrary to the curves for the Spalart-Allmaras model: this confirms the conclusion that the Spalart-Allmaras model is unable to properly model the separated flow in the recirculation region, while the two equation $k$-$\tau$ model seems to perform very well. At $x/D = 1.54$, the velocity profile from the Spalart-Allmaras model does not exhibit an increased velocity around $y/D = 1$ as do the other curves, and a less important deficit in momentum can be seen close to the centerline. As we move downstream, the two simulation curves get closer and closer to each other.

When looking at the transversal velocity profiles of Figure 3.21, both models perform similarly at $x/D = 1.54$ and 2.02, but again the Spalart-Allmaras model results are relatively far from the magnitudes seen in experiments and DNS data at

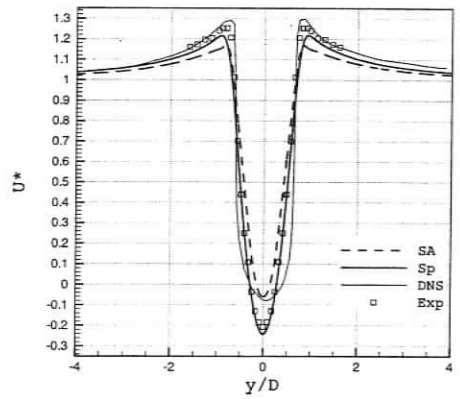


(a) x/D = 1.06

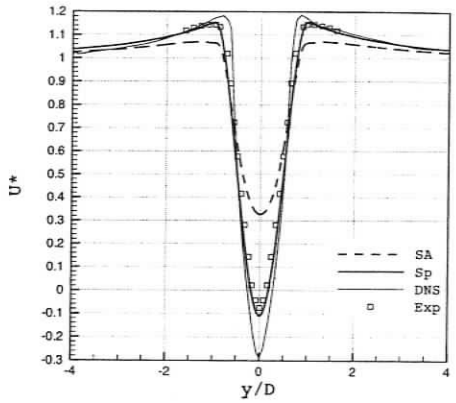


(b) x/D = 1.54

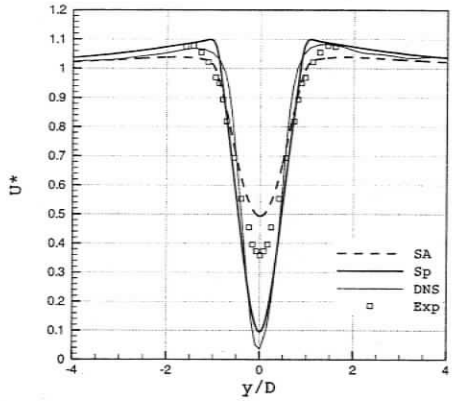


(c) x/D = 2.02

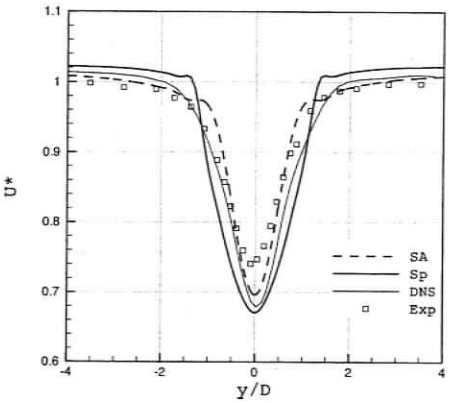


(d) x/D = 4

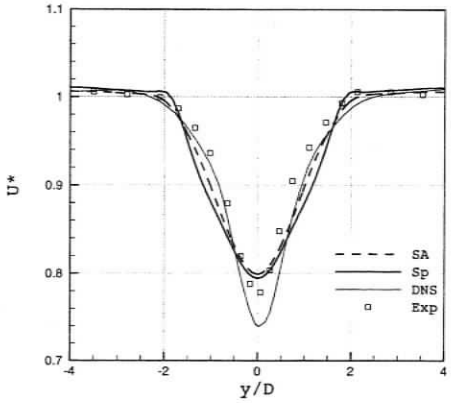


(e) x/D = 7

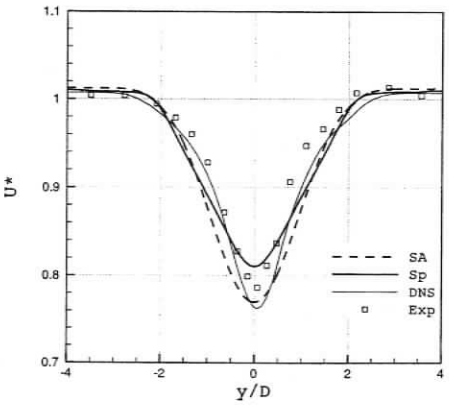


(f) x/D = 10

Figure 3.20: Mean longitudinal velocity profiles at different streamwise locations: comparison between URANS simulations.

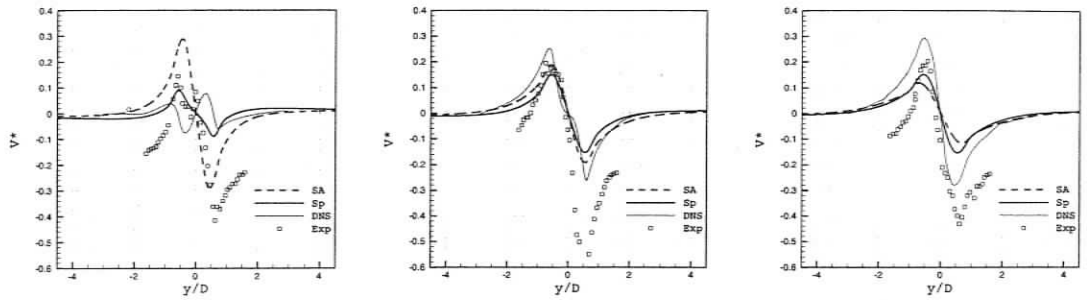


(a) x/D = 1.06 (b) x/D = 1.54 (c) x/D = 2.02

Figure 3.21: Mean transversal velocity profiles at $x/D = 1.06$, 1.54, and 2.02: comparison between URANS simulations. The DNS data is from Ma *et al.* (2000) and experiment by Lourenco & Shih (1993).

$x/D = 1.06$, where the large magnitudes in $V^*$ on the back of the cylinder can be seen as an excessive vertical flow motion that closes the recirculation zone too fast, since the boundary layer remains attached at locations where the cylinder tangential direction is getting closer and closer to the vertical direction.

The average longitudinal and fluctuating velocities, $U^{*2}_{rms} = u^2_{rms}/U^2_0$ and $V^{*2}_{rms} = v_{rms}/U^2_0$, are shown in Figure 3.22. The curves for the Spalart-Allmaras model are very close to the experimental and DNS data, both in magnitude and in shape, even in the very near wake, which suggests that this URANS model appropriately represents fluctuating velocities.

On the other hand, the magnitudes of the fluctuations from the $k$-$\tau$ Speziale model are much smaller than expected. This does not necessarily represent a lack of accuracy and can be explained as follows. What is plotted in Figure 3.22 are the velocity fluctuations computed by $\langle u_i'' u_i'' \rangle = \langle u_i^2 \rangle - \langle \widetilde{u}_i^{\,2} \rangle$, where $\widetilde{u}_i$ is the velocity field computed in the simulation, and is non-dimensionalized. Since the $k$-$\tau$ model uses a transport equation for the *unresolved* turbulent kinetic energy

$$k = \frac{1}{2}\widetilde{u_i'' u_i''} \tag{3.24}$$

the velocity fields that are resolved by the simulation do not contain all the fluctuations, and hence what is plotted in the figures is actually $< u_i'' u_i'' > |_{resolved} =< u_i'' u_i'' > - < u_i'' u_i'' > |_{modeled}$. The other models do not involve an equation for the turbulent kinetic energy and hence the expression $\langle u''u'' \rangle = \langle u^2 \rangle - \langle \widetilde{u}^2 \rangle$ gives all the fluctuating velocity; this is also true in the DNS and experimental. Thus, the curves for $< U^*_{rms} >$ and $< V^*_{rms} >$ with the $k$-$\tau$ model do not contain all the fluctuations, but only the contributions from the scales resolved through the computational grid.

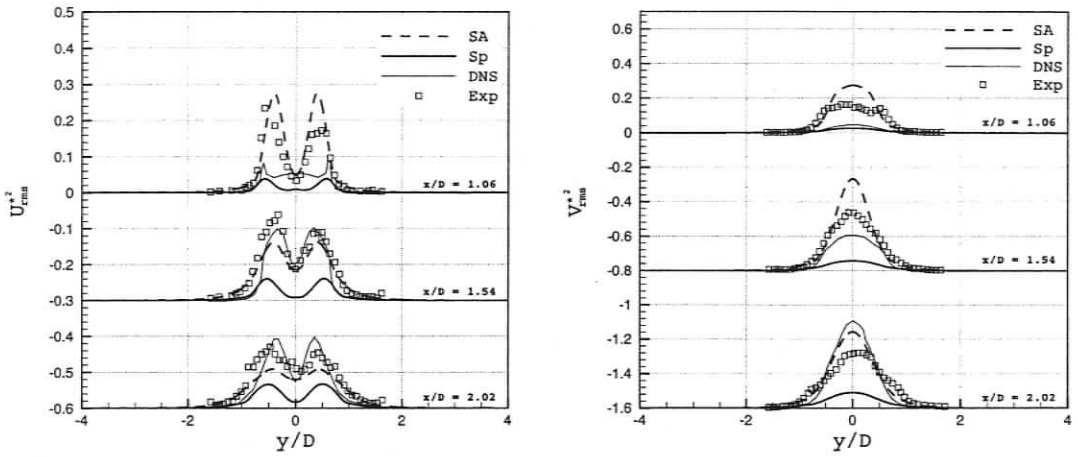


(a) $U^{*2}_{rms} = u^2_{rms}/U^2_0$ (b) $V^{*2}_{rms} = v^2_{rms}/U^2_0$

Figure 3.22: Streamwise and transversal fluctuating URANS velocity profiles, $U^{*2}_{rms} = u^2_{rms}/U^2_0$ and $V^{*2}_{rms} = v^2_{rms}/U^2_0$. The DNS data is from Ma *et al.* (2000) and the experimental squares from Lourenco & Shih (1993).

### 3.5.2 Large and Very Large Eddy Simulations

This section presents results from the Large Eddy Simulations (LES) using the Smagorinsky-Lilly model with constant coefficient and from the Very Large Eddy Simulation (VLES) using the adaptive $k$-$\tau$ model. In these types of simulations, time averaging of the results needs to be carried out over a very large number of shedding periods, at least 200 according to Franke & Frank (2002). Because of time constraints, the simulations had to be stopped and the averaging was only done over around 10 periods; thus the average results presented here need to be analyzed with caution. However, the main features of the characteristics of these simulations and subgrid-scale models can be observed.

The VLES is carried out on the same grid as URANS simulations, Grid A, while LES make use of Grid B.

Figure 3.23 shows the lift and drag coefficients, $c_L$ and $c_D$, versus non-dimensional time, $t^*$. Contrarily to the URANS signals, the curves for LES and VLES are not smooth sinusoidal curves from the main frequency of the vortex shedding scales and reveal the resolution of more frequencies.

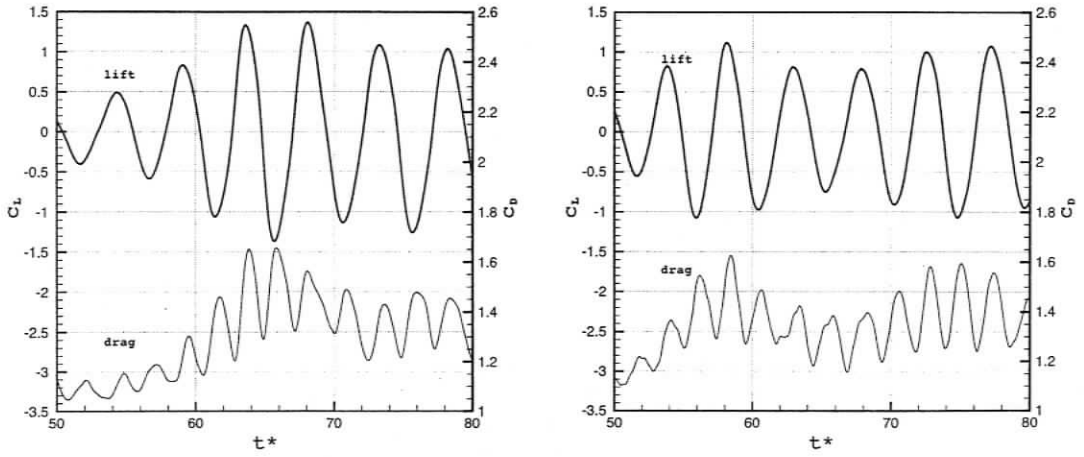


(a) LES (b) VLES

Figure 3.23: Lift and drag coefficients versus time from LES and VLES.

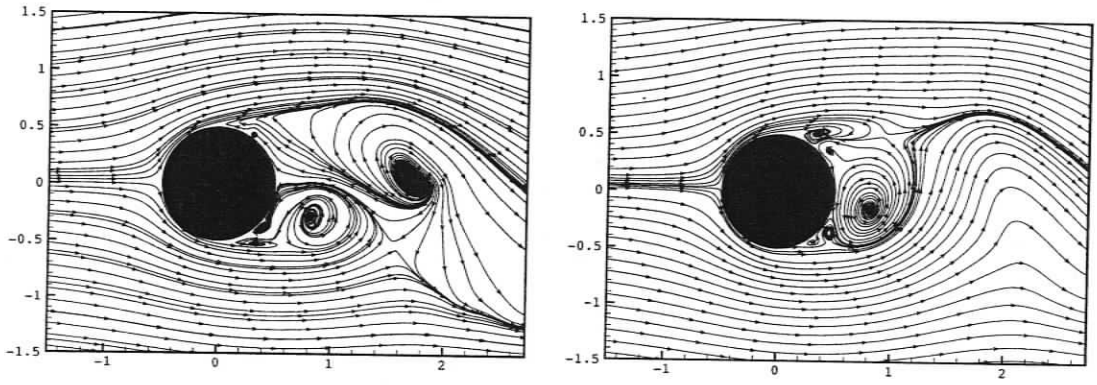


(a) LES (b) VLES

Figure 3.24: Instantaneous streamlines past a static circular cylinder at $Re_D = 3900$: comparison of LES and VLES results.

### Instantaneous Fields

Figure 3.24 shows the instantaneous streamlines from the LES and VLES. Note that both images are not taken at the same physical time nor at the same place within the period. Contrarily to the URANS simulations, the large and very large eddy simulations reveal small eddies in addition to the large vortices being shed. As expected, there are more structures in the LES fields than in the VLES ones.

The streamlines from the VLES reveal the formation of a vortex on the upper surface, while the large one from the lower surface is about to be shed. Furthermore, one can observe two small eddies near the lower back surface, and a secondary one on the upper surface. In the LES figure, two small eddies can be seen on the lower back surface in addition to the main vortex that is growing from the lower surface, while a very small eddy is seen on the upper back surface. It is interesting to note that small eddies are present next to the separation points on top and bottom walls.

Instantaneous fields of density, longitudinal and transversal velocity components, pressure coefficient, energy and spanwise vorticity are shown in Figures 3.25 and 3.26. Again, the LES yields more structures, but the differences between LES and VLES are not as important as they were between URANS models and both LES and VLES

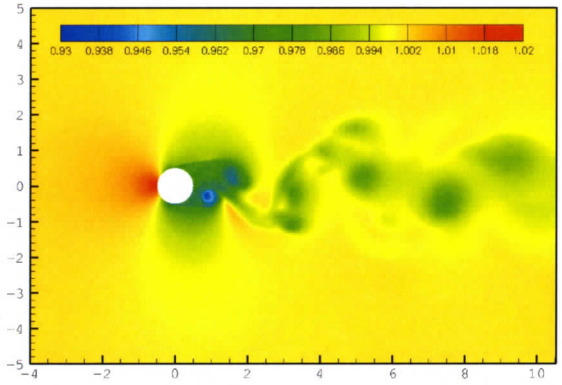


(a) LES $\rho/\rho_0$ at max $c_D$

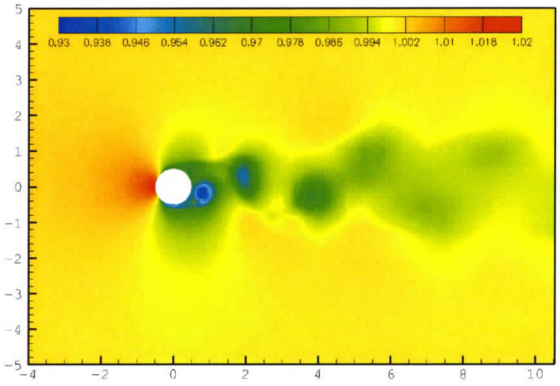


(b) VLES $\rho/\rho_0$ at max $c_D$

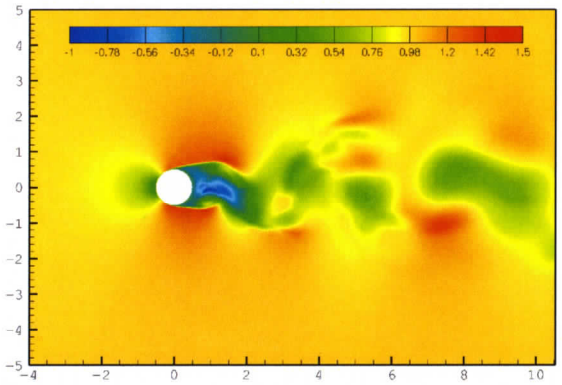


(c) LES $u/U_0$ at max $c_D$

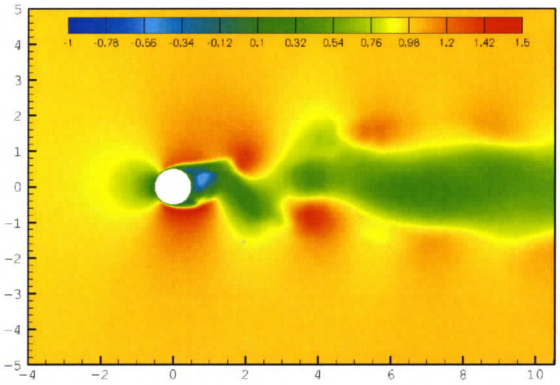


(d) VLES $u/U_0$ at max $c_D$

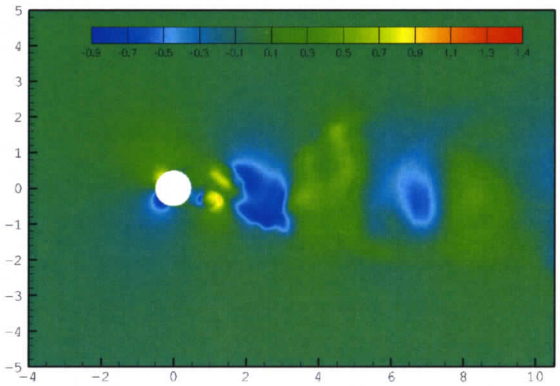

(e) LES $v/U_0$ at max $c_D$

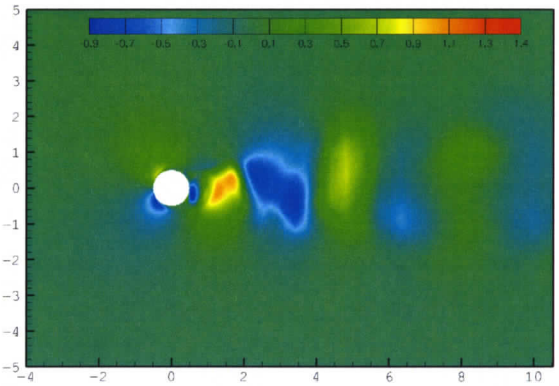

(f) VLES $v/U_0$ at max $c_D$

Figure 3.25: Instantaneous non-dimensional density, longitudinal and normal velocity components for the flow past a static circular cylinder at $Re_D = 3900$: comparison of LES (right) and VLES (left) results.

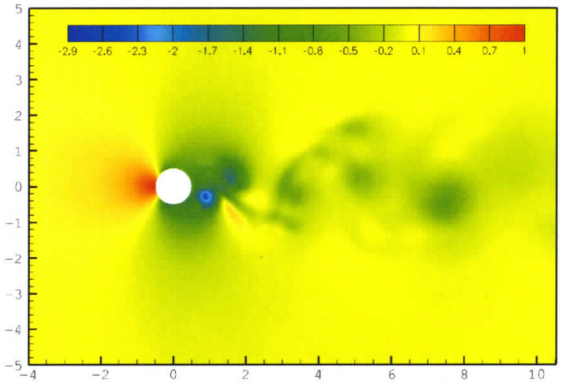


(a) LES $c_p$ at max $c_D$

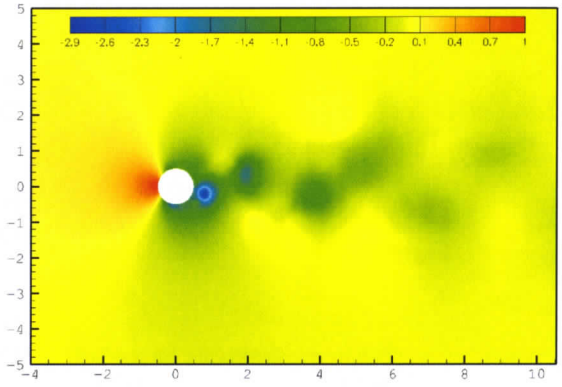


(b) VLES $c_p$ at max $c_D$

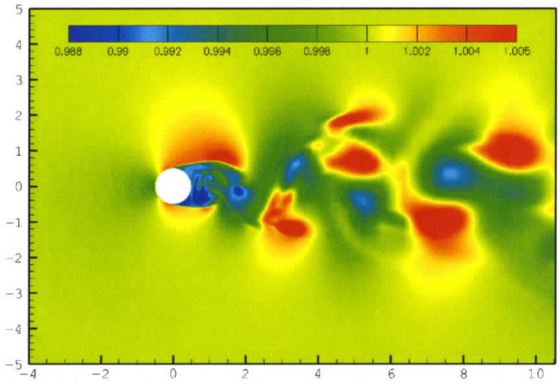


(c) LES $e/e_0$ at max $c_D$

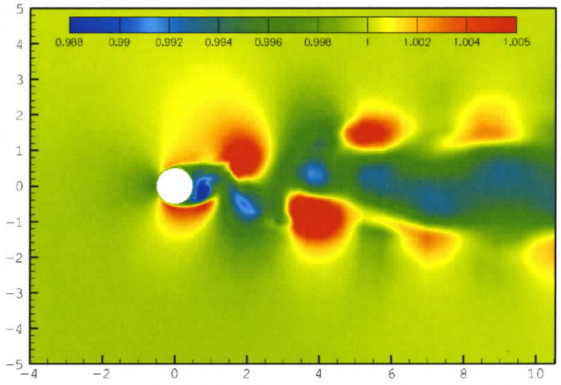


(d) VLES $e/e_0$ at max $c_D$

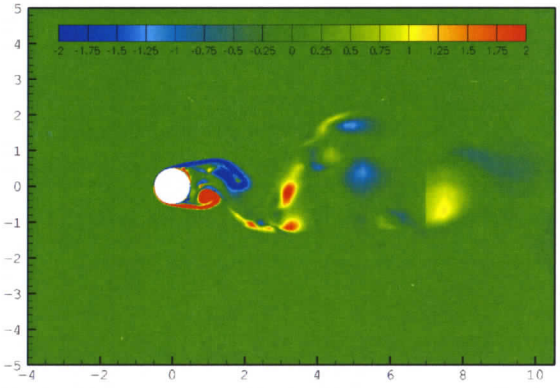


(e) LES $\omega_z D/U_0$ at max $c_D$

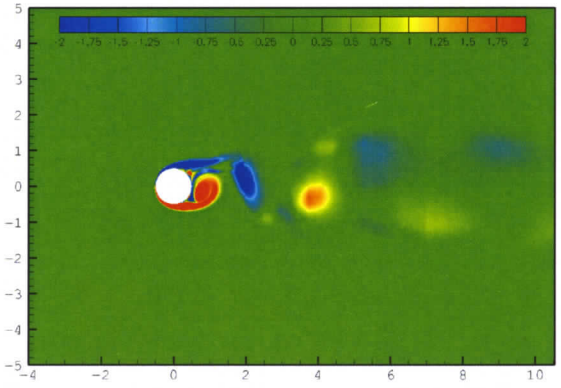


(f) VLES $\omega_z D/U_0$ at max $c_D$

Figure 3.26: Instantaneous pressure coefficient, energy, and out-of-plane vorticity for the flow past a static circular cylinder at $Re_D = 3900$: comparison of LES (right) and VLES (left) results.

seem to resolve more or less the same eddies. One can observe the most noticeable differences in the energy and vorticity fields, which show that the formation of the counter-clockwise rotating lower vortex is accompanied by small clockwise rotating scales in the recirculation zone. Furthermore, the LES shows that there is no shedding of a single large vortex, but rather that what seem to be a single large structure in URANS and VLES is actually a group of medium- and small-size eddies that move together.

Instantaneous iso-surfaces of longitudinal and transveral velocity components, as well as energy, are shown in Figure 3.27 for results from three-dimensional URANS $k$-$\tau$ simulations and LES. The main difference between the two types of simulations is the presence in the LES data of more three-dimensional effects in the velocity fields: most iso-surfaces in the URANS results look like flat ribbons, while the LES shows significant variations along the spanwise direction in the wake region. Where three-dimensionality is most visible is in the energy iso-surfaces which are far from being flat even in the URANS simulations.

### Time Averaged Fields

As stated previously, because of time constraints, the simulations had to be stopped and the averaging was only done over around 10 periods, which is far from sufficient in large and very large eddy simulations; thus the average results presented here need to be analyzed with caution, but the main features of the characteristics of these simulations and subgrid-scale models can be observed which justifies their presence here.

In the images of the average streamlines that can be seen in Figure 3.28, even though not enough average has been done, the recirculation length of both simulations seems to be very close. The two large structures on the back of the cylinder that were observed in the URANS average results are present, but we also observe smaller eddies

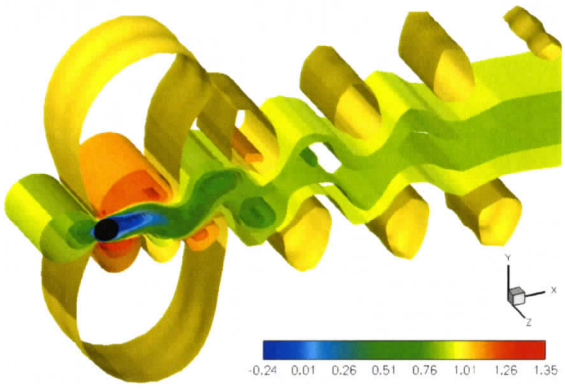


(a) $u/U_0$ URANS $k$-$\tau$

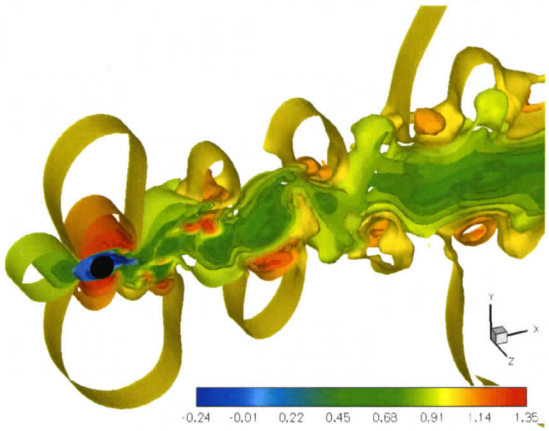


(b) $u/U_0$ LES

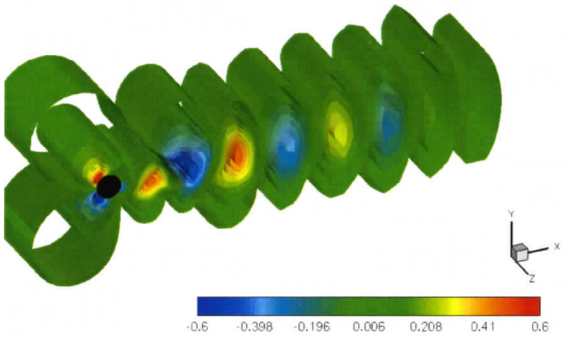


(c) $v/U_0$ URANS $k$-$\tau$

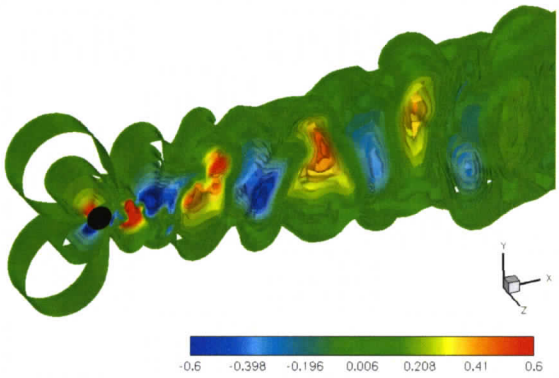


(d) $v/U_0$ LES

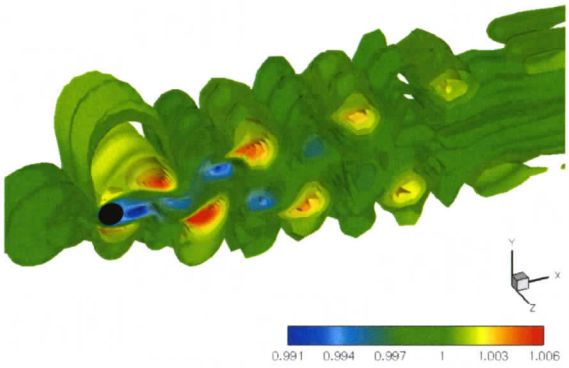


(e) $e/e_0$ URANS $k$-$\tau$

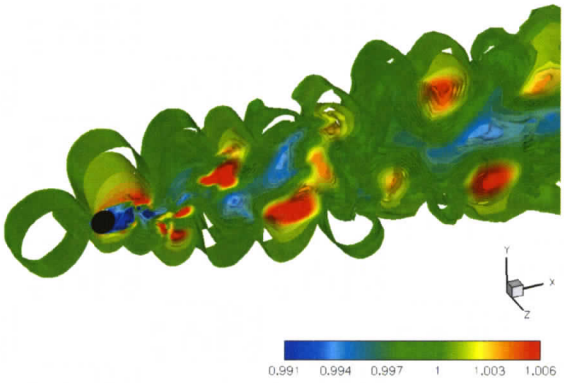


(f) $e/e_0$ LES

Figure 3.27: Instantaneous iso-surfaces of longitudinal and transveral velocity components, and energy for the flow past a static circular cylinder at $Re_D = 3900$: comparison of three-dimensionality in URANS $k$-$\tau$ Speziale (right) and LES (left) results.

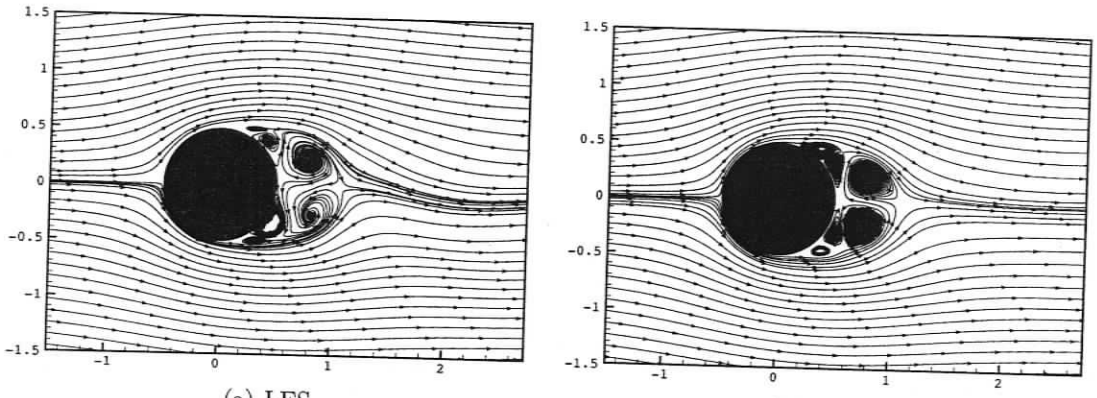


(a) LES (b) VLES

Figure 3.28: Average streamlines past a static circular cylinder at $Re_D = 3900$: comparison of LES (right) and VLES (left) results.

attached to the back of the cylinder. In the author's opinion, even after the statistics will have been computed over a large enough time, two small eddies at the average separation points will remain in addition to the large scales in the recirculation zone.

The average fields for density, longitudinal and transversal velocity components, pressure coefficient, energy and spanwise vorticity can be seen in Figures 3.29 and 3.30. Again, the differences between LES and VLES are much less important than the differences between URANS models or between LES/VLES and URANS Spalart-Allmaras results.

The average fields of the VLES are closer to being symmetric than the ones from the LES, which suggests that the average is closer to a statistically steady value for the VLES than for the LES, which is in accordance with the fact that there are fewer small high frequancy scales in the VLES and hence a smaller averaging time is required. The density in the fields varies between -7% and +2% with respect to the free-stream density, which is not different to what was observed in the URANS simulations. Both LES and VLES yield similar longitudinal and transversal velocities, which is confirmed by the velocity profiles along the wake. A slightly wider range of scales can be seen in the pressure coefficient and in the energy average fields of the

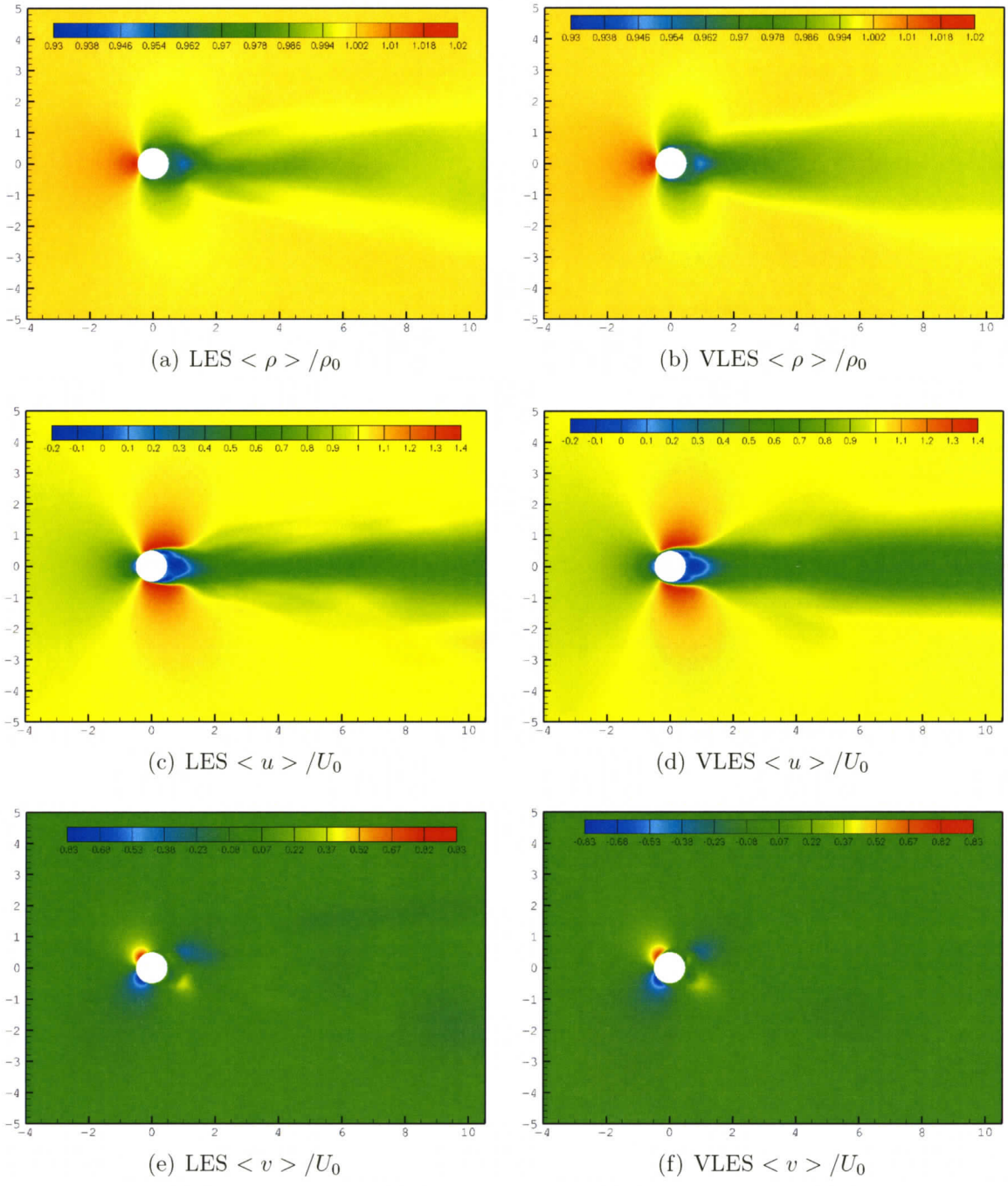

(a) LES $< \rho > /\rho_0$ (b) VLES $< \rho > /\rho_0$

(c) LES $< u > /U_0$ (d) VLES $< u > /U_0$

(e) LES $< v > /U_0$ (f) VLES $< v > /U_0$

Figure 3.29: Time average non-dimensional density, longitudinal and normal velocity components for the flow past a static circular cylinder at $Re_D = 3900$: comparison of LES (right) and VLES (left) results.

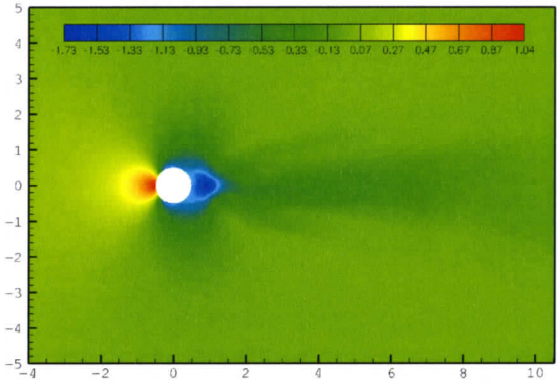

(a) LES $< c_p >$

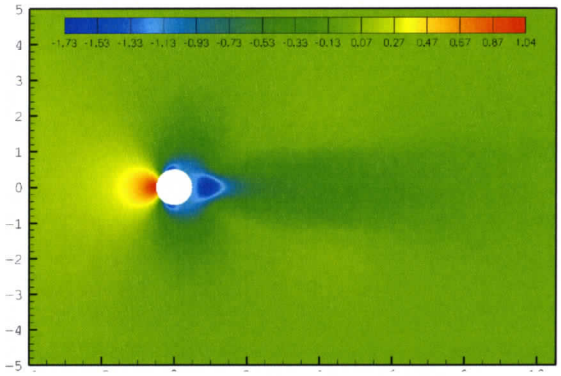

(b) VLES $< c_p >$

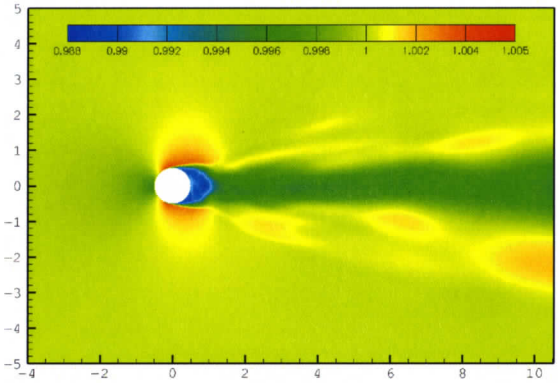

(c) LES $< e > /e_0$

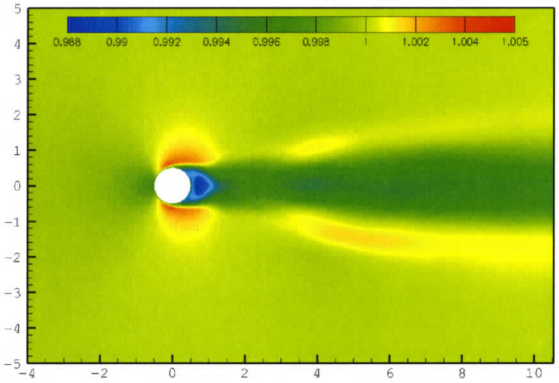

(d) VLES $< e > /e_0$

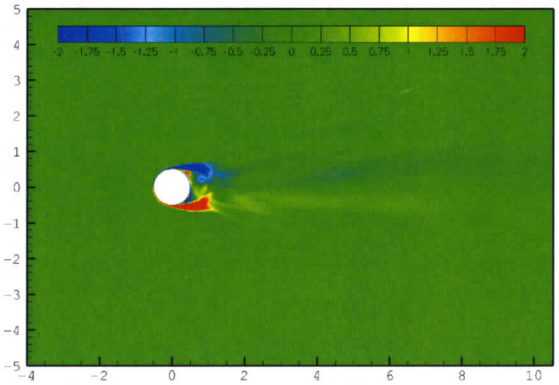

(e) LES $< \omega_z > D/U_0$

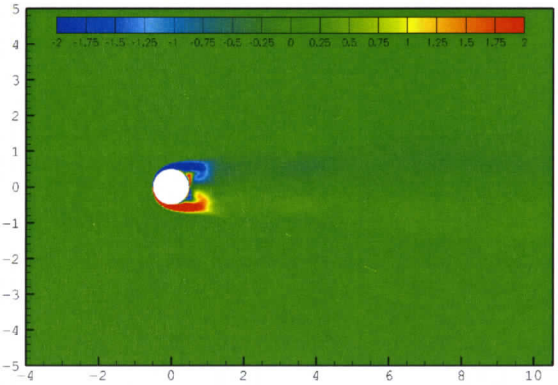

(f) VLES $< \omega_z > D/U_0$

Figure 3.30: Time average pressure coefficient, energy, and out-of-plane vorticity for the flow past a static circular cylinder at $Re_D = 3900$: comparison of LES (right) and VLES (left) results.

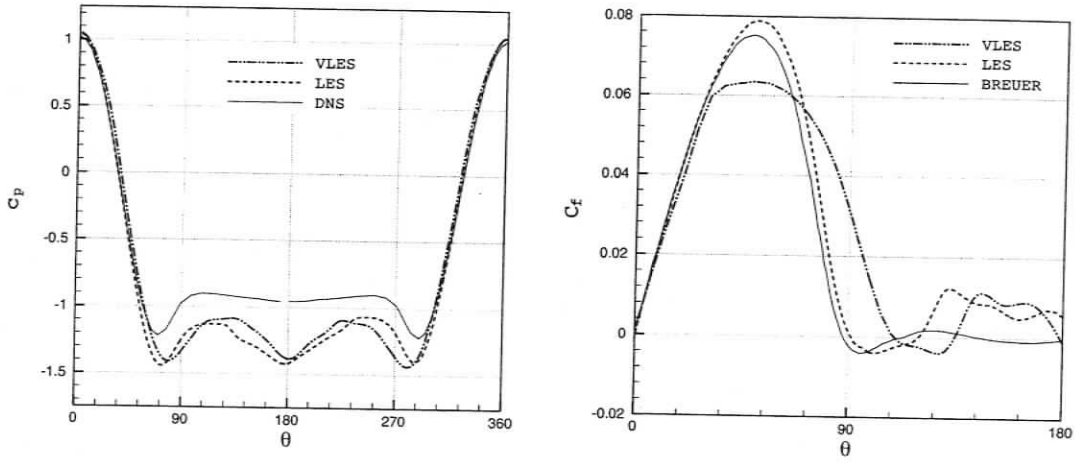


(a) $< c_p >$ (b) $< C_f >$

Figure 3.31: Average pressure coefficient on the cylinder surface for three-dimensional large and very large eddy simulations. DNS data is from Ma *et al.* (2000) and BREUER is a LES with the dynamic Smagorinsky model from Breuer (1998).

LES compared to the VLES. Finally, in the vorticity fields, the recirculation length is again confirmed to be close to equal in LES and VLES results and we observe that next to each one of the large eddies there is a small eddy closer to the centerline that rotates in the inverse direction.

### Average Quantities

The pressure and skin friction coefficients on the cylinder wall can be seen in Figure 3.31. It is very clear from the $c_p$ curve that the average is not yet satisfactory: both curves are far from being flat on the back of the cylinder, where the largest fluctuations occur due to the presence of small structures in the recirculation zone and hence larger where averaging times are needed. In particular, the LES curve is not symmetric with respect to the back at 180°, and averages should be the same on the upper and lower sides of the cylinder since the geometry and problem setup are symmetric. On the other hand, before separation the boundary layer remains laminar and contains no fluctuations so even an averaging over a small number of periods is

sufficient, and indeed both LES and VLES pressure coefficient curves are very close to the Breuer (1998) LES one down until close to the separation points. The LES and VLES pressure distribution are very similar and their minima largely underestimates the DNS value.

Concerning the skin friction, again past separation the averaging is not satisfactory and it is hard to conclude with respect to the accuracy of the simulations in the recirculation region. Yet one can see that the LES $C_f$ results are in very good agreement with the Breuer data until close to 110°, which shows that a LES with a simple constant-coefficient subgrid-scale model can properly capture the dynamics in the boundary layer region and even past separation, at least as well as a dynamic subgrid-scale model used by Breuer (1998) — the curve shape after 115° being the results of inappropriate statistics. On the contrary, the VLES does not seem to be accurate in solving the wall friction, which can be explained by the fact that it uses a coarser grid and its adaptive model certainly becomes, in this region, similar to a URANS type simulation.

The similarity of the LES and VLES results is noticeable in the longitudinal and transversal velocity profiles of Figures 3.32 and 3.33, at least in the near wake until $x/D = 4$. The LES and VLES curves are almost indistinguishable at $x/D = 1.06$ and remain very close at $x/D = 1.54$, 2.02 and 4, the difference being mostly due to better statistics of the VLES data than of the LES results. Down to $x/D = 2.02$, our results over-predict the DNS and experimental data, in particular close to the centerline. From $x/D = 4$ on, the present large and very large eddy simulations yield smaller magnitudes of longitudinal velocity than other data in the literature, but since statistics need to be improved one cannot conclude with certainty on the accuracy of the subgrid-scale models employed. The transversal velocity is in much better agreement with the experimental results than the longitudinal component, at least along the positions $x/D = 1.06$, 1.54, and 2.02 given in Figure 3.33.

Profiles for the fluctuating velocity components, $U^{*2}_{rms} = u^2_{rms}/U^2_0$ and $V^{*2}_{rms} =$

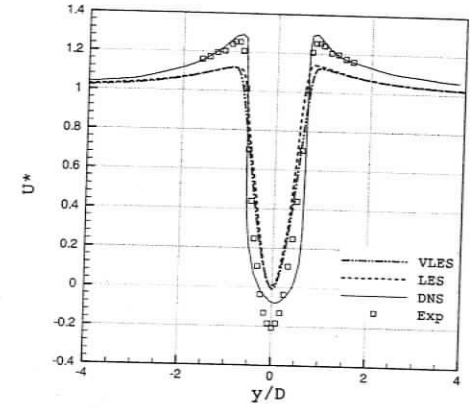


(a) x/D = 1.06

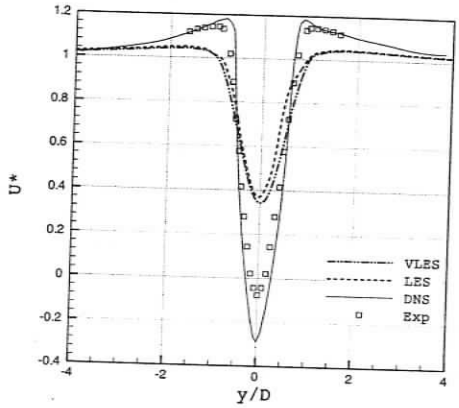


(b) x/D = 1.54

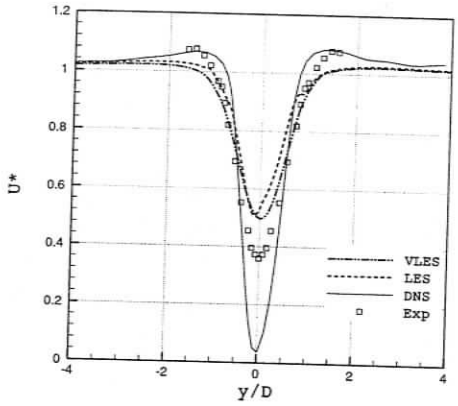


(c) x/D = 2.02

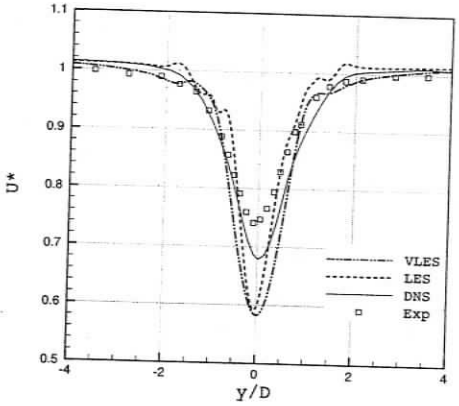


(d) x/D = 4

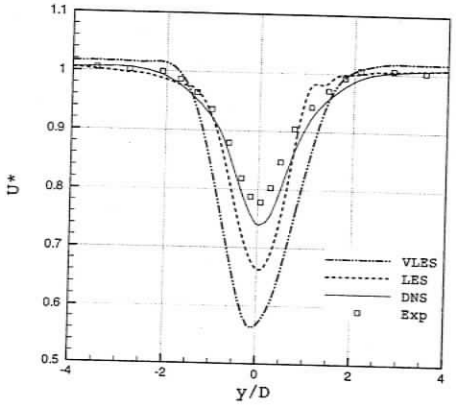


(e) x/D = 7

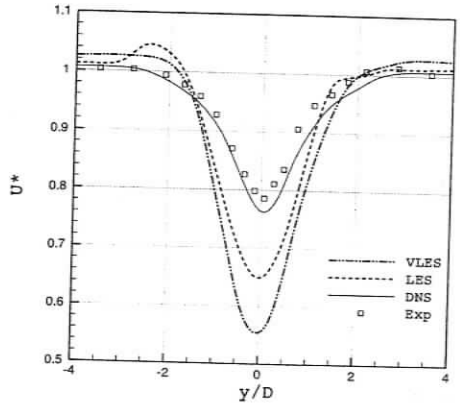


(f) x/D = 10

Figure 3.32: Mean longitudinal velocity profiles at different streamwise locations: comparison between large and very large eddy simulations.

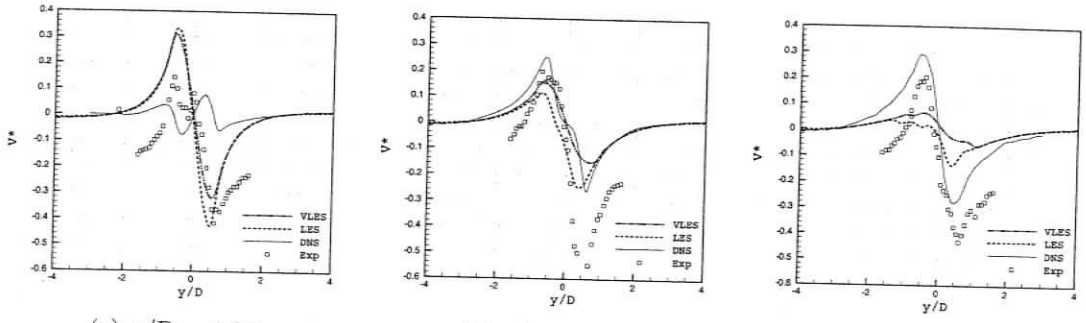


(a) x/D = 1.06 (b) x/D = 1.54 (c) x/D = 2.02

Figure 3.33: Mean transversal velocity profiles at $x/D = 1.06$, 1.54, and 2.02: comparison between large and very large eddy simulations. The DNS data is from Ma *et al.* (2000) and experiment by Lourenco & Shih (1993).

$v^2_{rms}/U^2_0$, can be seen in Figure 3.34. Transversal fluctuations are very similar for LES and VLES results, but differ significantly from the DNS and experimental data. The longitudinal fluctuations seem to be in better agreement with the experimental results on the three locations considered, and with the DNS data except at $x/D = 1.06$ where the DNS results carry much less energy than any other data set considered here — which was also observed when URANS simulation results were analyzed. The fluctuation being characterized by smaller frequencies than the average motions, the use of averaging over a large time is crucial, and before better statistics are obtained the author only ventures to say that both LES and VLES results seem to be accurate in resolving fluctuating motions, as expected from such type of simulations and as confirmed by the presence of small eddies in the instantaneous fields of Figures 3.25 and 3.26.

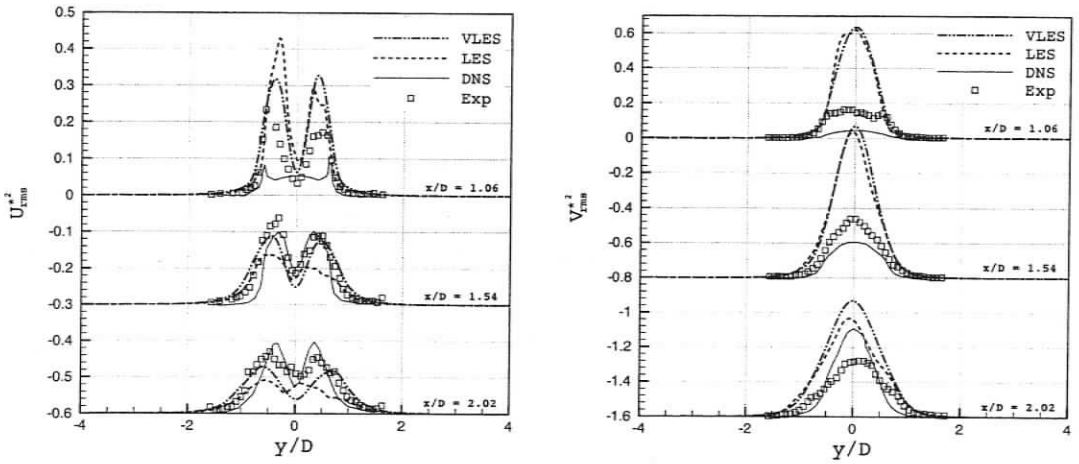


(a) $U^{*2}_{rms} = u^2_{rms}/U^2_0$ (b) $V^{*2}_{rms} = v^2_{rms}/U^2_0$

Figure 3.34: Streamwise and transversal fluctuating velocity profiles, $U^{*2}_{rms} = u^2_{rms}/U^2_0$ and $V^{*2}_{rms} = v^2_{rms}/U^2_0$: comparison between large and very large eddy simulations. The DNS data is from Ma *et al.* (2000) and the experimental squares from Lourenco & Shih (1993).

## 3.6 Fluent Simulations with Spalart-Allmaras Turbulence Model

The commercial CFD code Fluent is used in order to investigate the difference in results with the code SPARC, when both programs use the Spalart-Allmaras model (with the same model coefficients), on the same grid and with the same boundary conditions. The setup is the same as in SPARC, namely compressible, viscous, ideal gas flow with segregated solvers in an implicit $2^{nd}$ order formulation, and same time step of 0.02 ms.

Images of the instantaneous fields for longitudinal and transversal velocity components, pressure coefficient and spamwise vorticity can be seen in Figure 3.35 and the averages fields in Figure 3.35: they are undistinguishable from the fields of given by the SPARC simulations.

However, a detailed look at the pressure coefficient on the cylinder wall and at

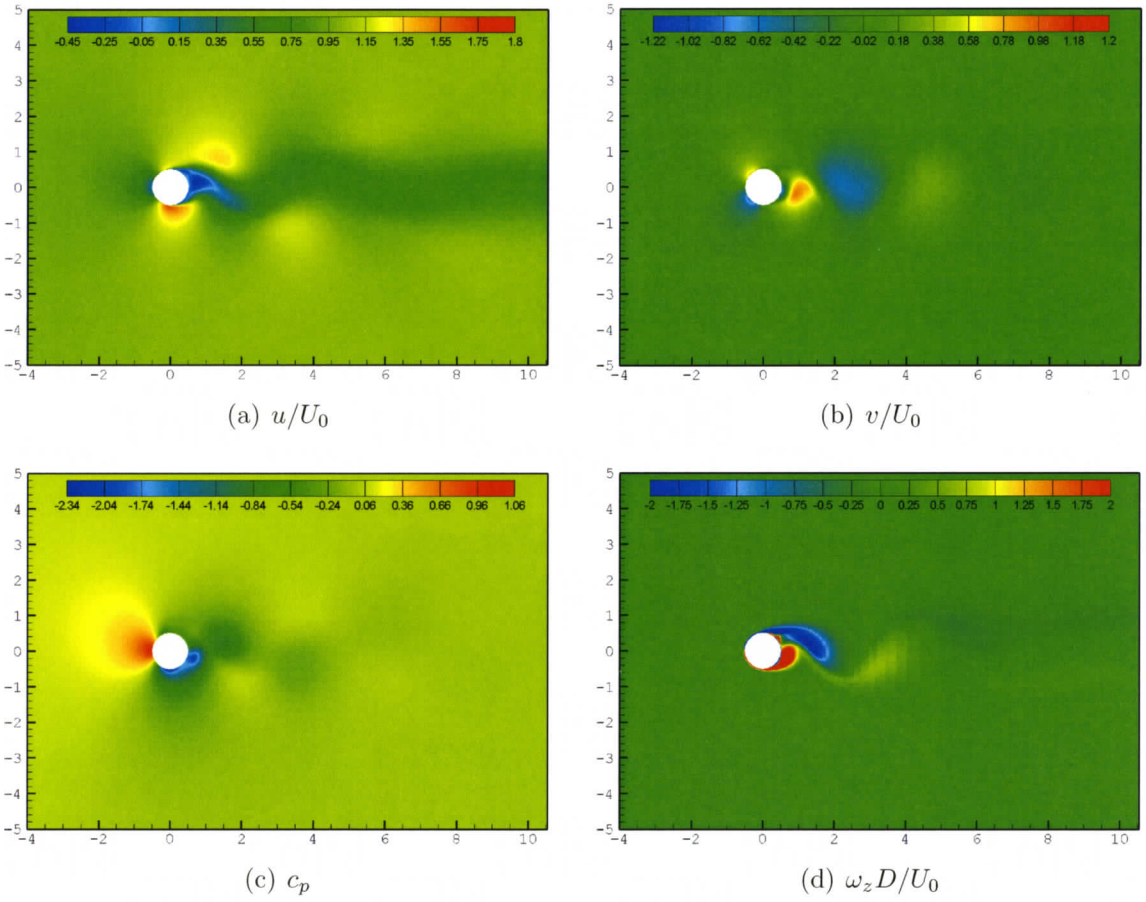


(a) $u/U_0$ (b) $v/U_0$

(c) $c_p$ (d) $\omega_z D/U_0$

Figure 3.35: Instantaneous non-dimensional longitudinal and normal velocity components, pressure coefficient, and out-of-plane vorticity for the flow past a static circular cylinder at $Re_D = 3900$ using Fluent with the Spalart-Allmaras turbulence model.

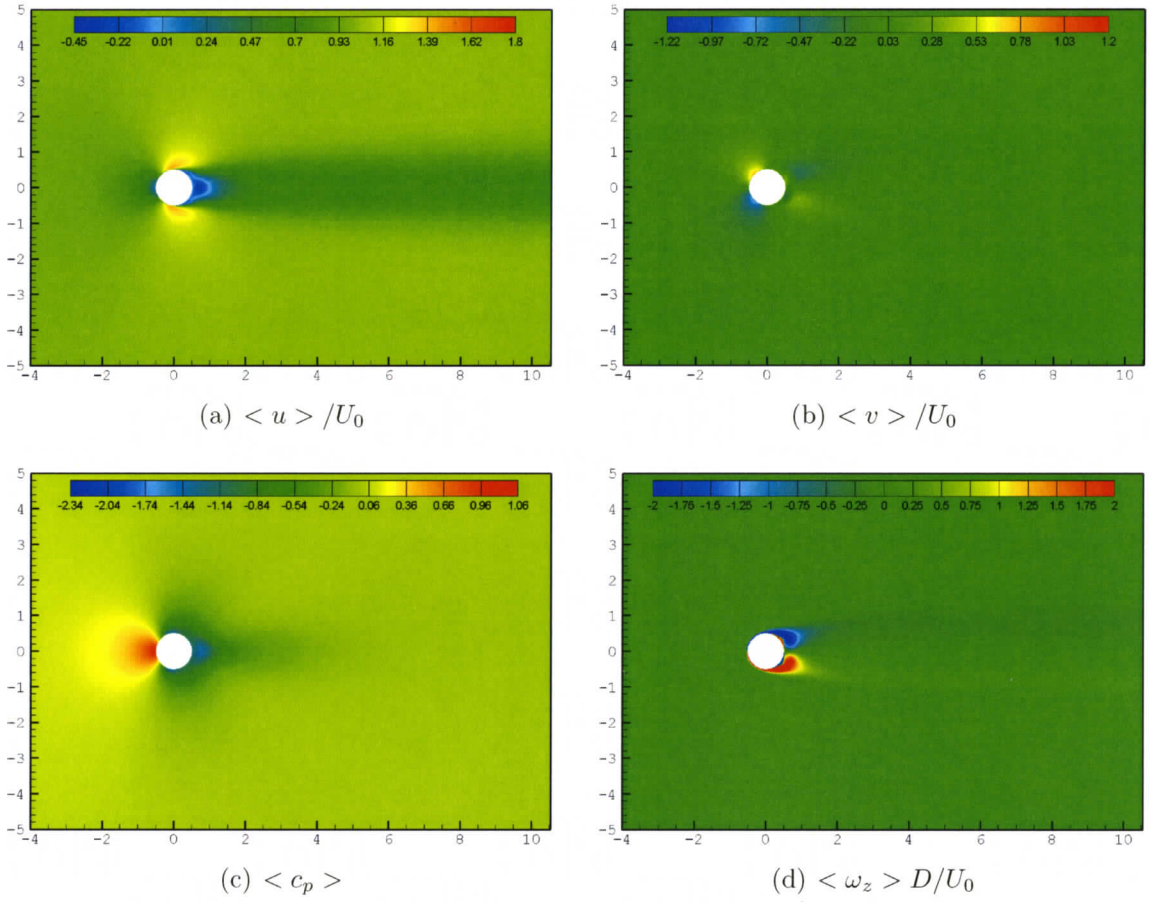


(a) $< u > /U_0$ (b) $< v > /U_0$

(c) $< c_p >$ (d) $< \omega_z > D/U_0$

Figure 3.36: Time average non-dimensional longitudinal and normal velocity components, pressure coefficient, and out-of-plane vorticity for the flow past a static circular cylinder at $Re_D = 3900$ using Fluent with the Spalart-Allmaras turbulence model.

the velocity profiles along the wake reveals significant differences. As can be seen in Figure 3.37, the values of $< c_p >$ from the Fluent results is even lower than that from SPARC, and farther from the DNS values, in particular near and around the minimum. Furthermore, the SPARC curve is flatter on the back of the cylinder which suggests that, independently of the model, Fluent has more difficulties resolving the sensitive motions in the recirculation zone and in particular in the middle of the region $y = 0$, the back pressure coefficient being largely under-estimated compared to the DNS one.

Another important difference is revealed by the curve of longitudinal velocity along the centerline of Figure 3.37. Overall, the curves from SPARC and Fluent results are similar except for two important differences. First, while both minima occur at more or less the same location close to $x/D = 0.7$, the value of the minimum is quite different, and it seems that the Fluent one is lower than any other data set. Second, the Fluent curve becomes flat very fast past $x/D = 3$, while the rest of the data sets available show a variation of mean streamwise velocity at the centerline even after $x/D = 5$, but it doesn't show the somewhat unexpected behavior of the SPARC curve (SA Sparc) which changes slope sign and has a crest around $x/D = 5.5$.

If one looks at the longitudinal velocity profiles of Figure 3.38, the Fluent and SPARC curves keep more or less the same shape and separation between each other, and both show higher velocities than the DNS and experimental data sets at $x/D =$ 1.06, 1.54 and 2.02. The two curves of Fluent and SPARC are very close together at $x/D = 7$ and very far at $x/D = 10$. Overall, whether Fluent or SPARC are used, the Spalart-Allmaras turbulence model seems less accurate in predicting the dynamics of the vortex shedding. The difference between Fluent and SPARC simulation results is even less visible in the transversal velocity profiles of Figure 3.39.

Fluctuating longitudinal and transversal velocity components as represented by the r.m.s. profiles of Figure 3.40 reveal significant differences between the Fluent and SPARC simulations. Both codes capture quite properly the shape of these profiles,

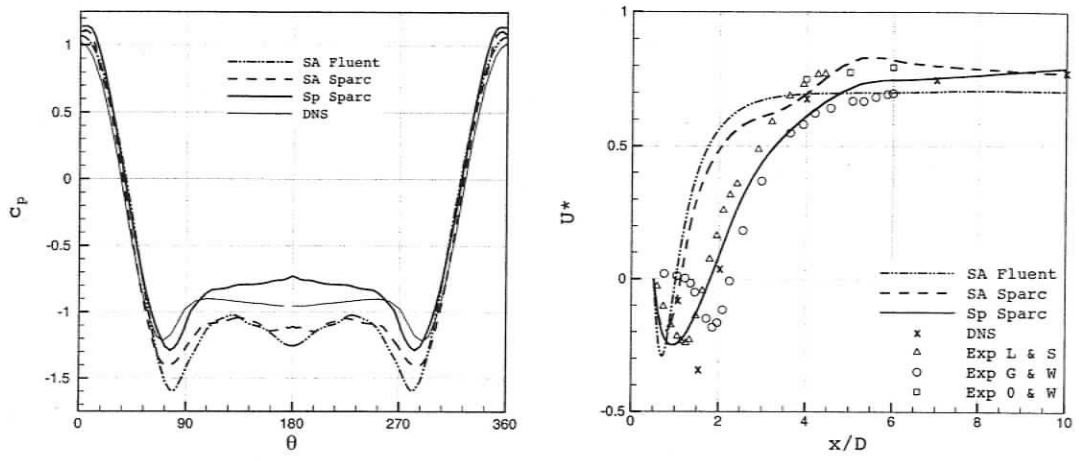


(a) $< c_p >$ (b) $U^* =< u > /U_0$

Figure 3.37: Average pressure coefficient on the cylinder wall and streamwise velocity components, $U^* =< u > /U_0$ and $V^* =< v > /U_0$, along the centerline $y = 0$ for SPARC and Fluent simulations using the Spalart-Allmaras turbulence model; triangles `Exp L&S` by Lourenco & Shih (1993); circles `Exp G&W` from a private communication of R. Govardhan and C. Williamson (found in Ma *et al.* (2000)); squares `Exp O&W` by Ong & Wallace (1996); DNS data by Ma *et al.* (2000).

but the Fluent computations yield less accurate longitudinal profiles (compared to the experimental results by Lourenco & Shih (1993)) at $x/D = 1.54$ and 2.02 when the Fluent curves flatten too fast. The transversal fluctuations given by Fluent seem to perform quite well except very close to the cylinder at $x/D = 1.06$ where the amplitudes seem over-estimated by Fluent even more than what they are by SPARC.

The vortex shedding Strouhal number, mean drag and back pressure coefficients, and mean separation angle for Fluent and SPARC using the Spalart-Allmaras turbulence model are given in Table 3.6. The error with respect to the DNS data by Tremblay *et al.* (2000) is larger for the Fluent than for the SPARC simulation results, but only significantly more important for the Strouhal number. Thus, overall, the inaccuracy in drag, pressure coefficient, and separation angle can be assumed to come from the inability of the Spalart-Allmaras model to properly resolve the flow past a cylinder in the sub-critical regime, and not to the solution and discretization

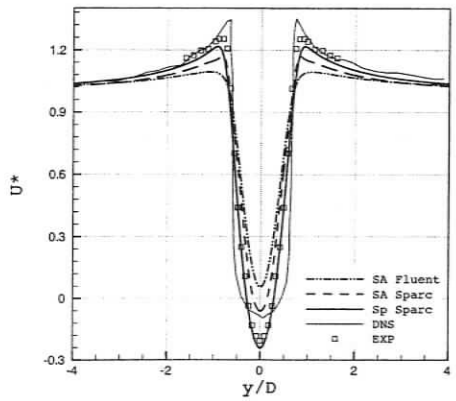


(a) x/D = 1.06

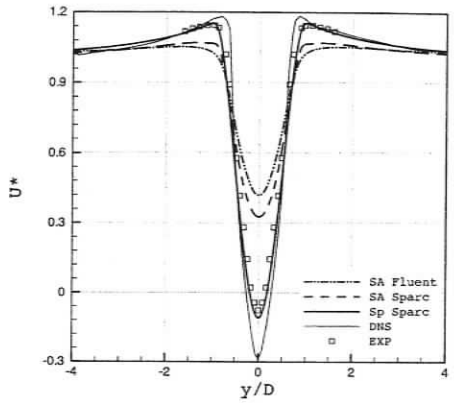


(b) x/D = 1.54

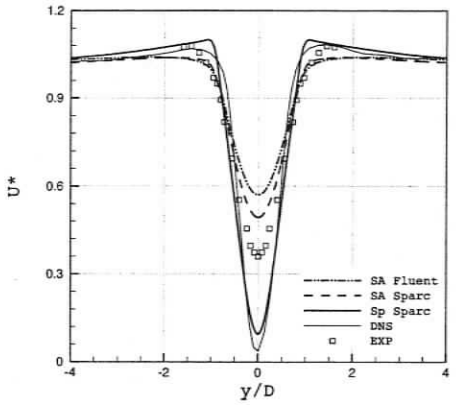


(c) x/D = 2.02

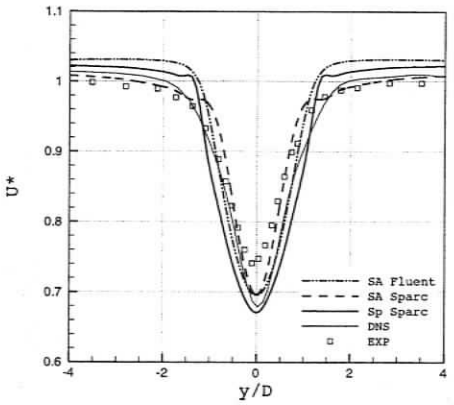


(d) x/D = 4

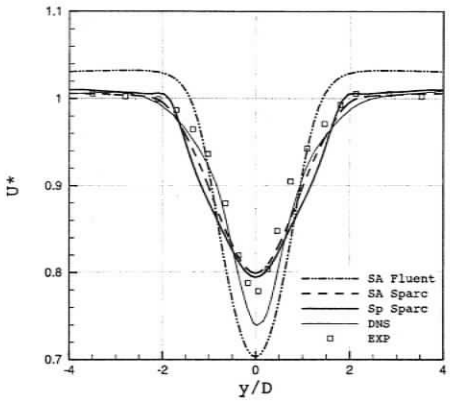


(e) x/D = 7

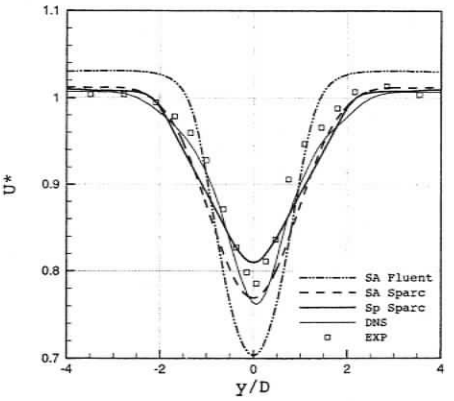


(f) x/D = 10

Figure 3.38: Average longitudinal velocity profiles, $U^* =< u > /U_0$, at different streamwise locations: comparison between for SPARC and Fluent simulations using the Spalart-Allmaras turbulence model.

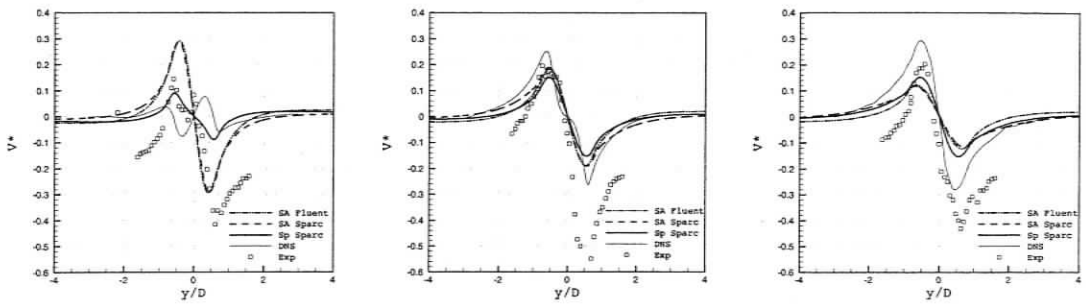


(a) x/D = 1.06 (b) x/D = 1.54 (c) x/D = 2.02

Figure 3.39: Average longitudinal velocity profiles, $U^* =< u > /U_0$, at different streamwise locations: comparison between for SPARC and Fluent simulations using the Spalart-Allmaras turbulence model.

methodology. On the other hand, discrepancies between SPARC and Fluent simulation results may be due to the difference in dissipation and numerical schemes, which cannot be chosen or controlled in the commercial package.

Table 3.6: Comparison of the simulation results using Fluent and SPARC with the Spalart-Allmaras turbulence model, for the case of a static cylinder at $Re_D = 3900$. The percents represent errors with respect to the DNS results by Tremblay *et al.* (2000).

| **Solver** | $St$ | $< c_D >$ | $< c_{p_b} >$ | $< \theta_s >$ |
|---|---|---|---|---|
| DNS | 0.220 | 1.03 | −0.92 | 94.3° |
| SPARC | 0.2183 | 1.2922 | −1.2404 | 103.5° |
| | (-0.8%) | (25.5%) | (-34.8%) | (9.8%) |
| Fluent | 0.1819 | 1.3133 | −1.3430 | 103.5 |
| | (−17.3%) | (27.5%) | (-46.0%) | (−5.1%) |
| Fluent w.r.t. SPARC | −16.7% | 1.6% | 7.6% | 0% |

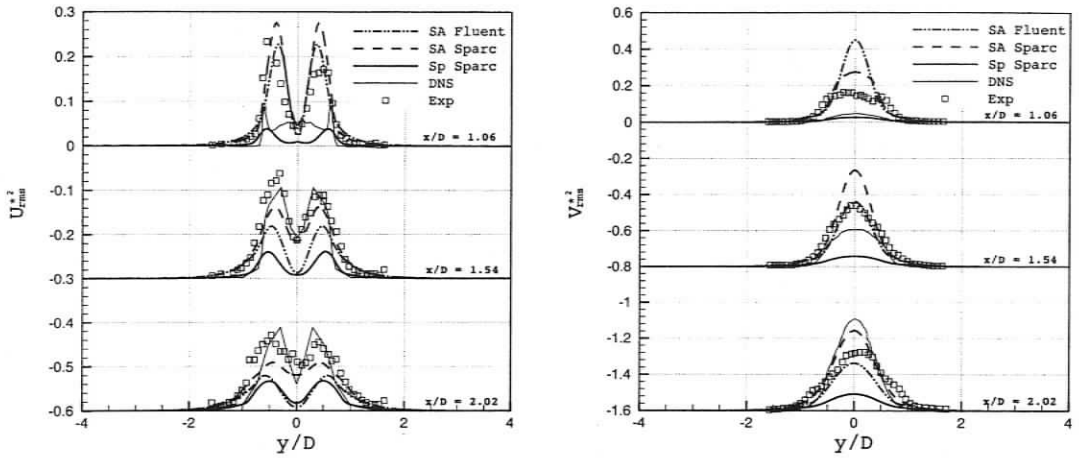


(a) $U^{*2}_{rms} = u^2_{rms}/U^2_0$ (b) $V^{*2}_{rms} = v^2_{rms}/U^2_0$

Figure 3.40: Streamwise and transversal fluctuating velocity profiles, $U^{*2}_{rms} = u^2_{rms}/U^2_0$ and $V^{*2}_{rms} = v^2_{rms}/U^2_0$: comparison between for SPARC and Fluent simulations using the Spalart-Allmaras turbulence model. The DNS data is from Ma *et al.* (2000) and the experimental squares from Lourenco & Shih (1993).

## 3.7 URANS Simulations of Oscillating Cylinder

After the turbulence modeling techniques considered in this study were applied to the flow around a stationary cylinder, we turned out attention to the problem of a cylinder oscillating transversely — *i.e.* perpendicularly to the uniform free-strea — at a Reynolds number of $Re_D = 3600$ which is simulated with the URANS $k$-$\tau$ Speziale turbulence model. Due to a lack of sufficient computational resources, the simulations performed for the oscillatory motion are two-dimensional. The $k$-$\tau$ Speziale model is used because it yields accurate results in the case of the stationary cylinder at a relatively low computational cost and because it can be used in a two-dimensional simulation without loosing too much accuracy in the mean results, contrary to a LES or a VLES which need to be performed using a three-dimensional solver.

Some authors present their results in terms of Strouhal number, but here they are given in terms of frequency rather since a proper Strouhal number would need to be computed based on the wake width which is not easy to determine. The frequencies

Table 3.7: Oscillating cylinder results from two-dimensional simulations using the $k$-$\tau$ Speziale turbulence model at $Re_D = 3600$. The experimental results are from Stansby (1976).

| Case | I | II | III | IV | V | VI |
|---|---|---|---|---|---|---|
| $f_c/f_0$ | 0.523 | 0.608 | 0.638 | 0.800 | 1.079 | 1.274 |
| $f_s/f_0$ Stansby (1976) | 1.005 | 1.021 | 0.639 | 0.801 | 0.780 | 0.817 |
| $f_s/f_0$ | 0.539 | 0.616 | 0.655 | 0.809 | 1.271 | 1.078 |
| Difference | −46.4% | −39.7% | 2.4% | −0.9% | 62.9% | 32.0% |

are non-dimensionalized with respect to the frequency, $f_0$, of vortex shedding past the stationary cylinder at the same Reynolds number of 3600, which is found to be $f_0 = 12.983$ from a numerical simulation performed to this purpose — this would correspond to a Strouhal number based on cylinder diameter of 0.1892.

Five simulations are performed at an oscillating amplitude of $A/D = 0.3$ and different cylinder motion frequencies $f_c/f_0 \in \{0.523, 0.608, 0.800, 1.079, 1.274\}$, and the resulting vortex shedding frequencies relative to the cylinder motion, $f_s/f_c$, are summarized in Table 3.7. and plotted in Figure 3.41. The transversal motion of the cylinder follows the sinusoidal relation

$$\frac{y(t)}{D} = \frac{A}{D}\sin(2\pi f_c t). \tag{3.25}$$

In the experiments of Stansby (1976) at the same oscillating amplitude $A/D = 0.3$, lock-in of the vortex shedding frequency on the motion frequency was observed for $f_c/f_0$ on the interval [0.638, 1.071], as seen by the straight line of slope unity in Figure 3.41. In the present simulations, lock-in occurs as early as $f_c/f_0 = 0.523$ as the Case I simulation reveals, and is still present in Case IV for $f_c/f_0 = 0.8$. Then the shedding frequency increases past the motion frequency — which was never observed by Stansby — for Case V before finally decreasing in Case VI. The limited number of motion frequencies simulated do not allow us to verify how the decrease in shedding

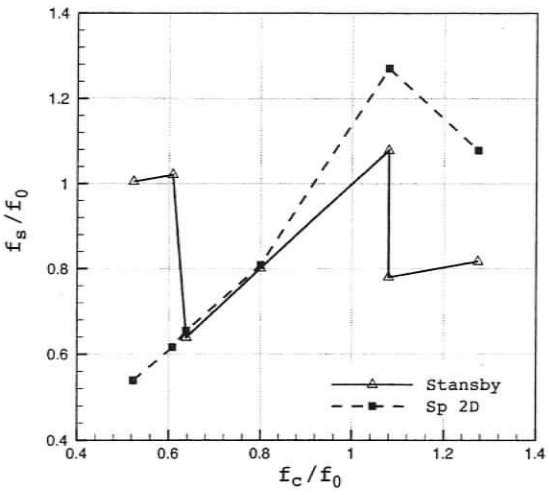


Figure 3.41: Vortex shedding frequency, $f_s/f_0$, versus cylinder motion frequency, $f_c/f_c$, from the two-dimensional URANS simulation with the $k$-$\tau$ Speziale model. The experimental data is from Stansby (1976).

frequency takes place past the lock-in region, and a couple of other cases between V and VI are required.

The fact that lock-in is observed as early as Case I is unexpected and can be due to several reasons. First, the subtle physical phenomena that is responsible for lock-in, and vortex shedding in general, can be hard to capture numerically in particular in the sub-critical regime of transition. A numerical simulations may not contain enough instabilities in order to trigger the change in vortex shedding frequency from the forced motion one, or it may take a long physical time for it to happen. The simulations were stopped since the shedding had become perfectly periodic, but it may still bifurcate into another regime.

Second, the numerical simulations are two-dimensional, and even tough the vortex shedding due to forced motion is two-dimensional, the phenomena that triggers the shedding at a particular frequency may be three-dimensional, and due to small motions in the third direction. Furthermore, if the triggering is indeed, as it seems,

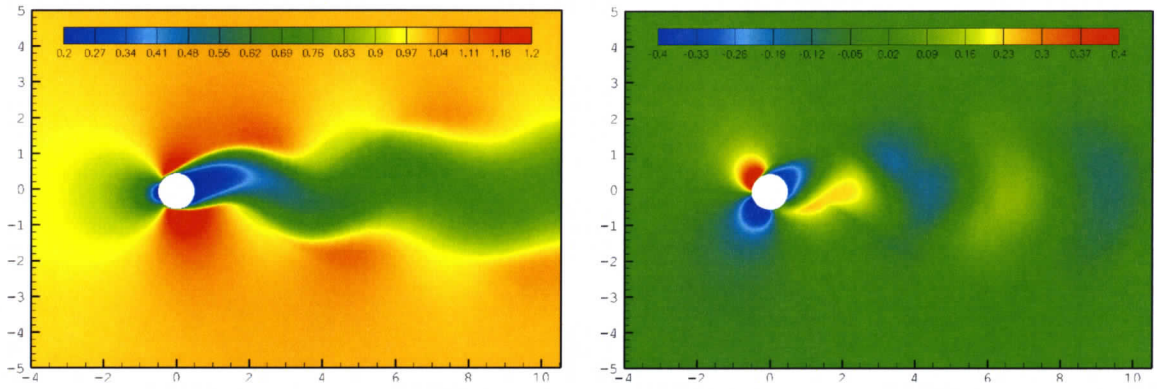

(a) $u/U_0$ (b) $v/U_0$

(c) $e/e_0$ (d) $\omega_z D/U_0$

Figure 3.42: Instantaneous non-dimensional longitudinal and normal velocity components, energy, and out-of-plane vorticity for the flow past an oscillating circular cylinder at $Re_D = 3600$, case IV; the cylinder is traveling downwards.

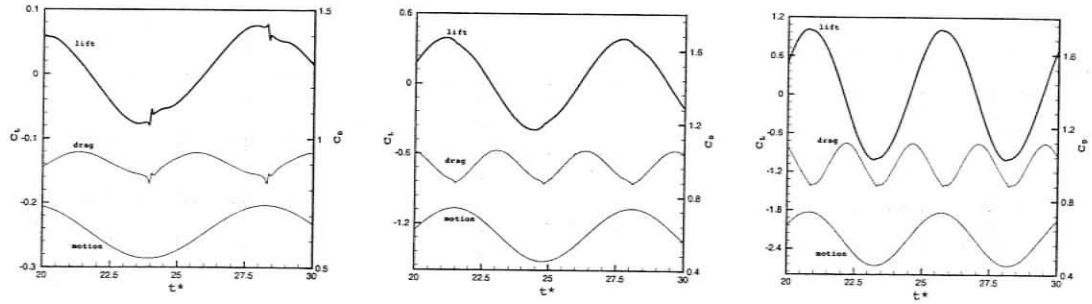


(a) Case II (b) Case IV (c) Case V

Figure 3.43: Lift and drag coefficient versus non-dimensional time for the flow past an oscillating circular cylinder at $Re_D = 3600$: case II, IV, and V.

due to small motions with high frequencies, the time step may have a strong influence on the shedding motion: for instance if the time step is such that the ephemeral triggering phenomena are skipped between two time steps, the shedding characteristics may strongly be affected. This may happen even if the time step is small enough the capture all the physics of the phenomena once the shedding motion has been established. Thus, again, it may take a very long time for the simulations to reach the final bifurcation of a periodically steady shedding. Since no numerical simulations close to this Reynolds number of 3600 are available in the literature, it remains hard to conclude on the behavior observed in the present study, and further investigation is required.

Figure 3.42 shows instantaneous fields of longitudinal and transversal velocity components, energy, and spanwise vorticity for Case IV, at a time when the cylinder is traveling downwards. Compared to the static cylinder fields, the wake in the forced motion ones is wider and propagates farther downstream with fewer dissipation. A look at the streamlines shows that there are no eddies as the ones seen in the static case.

According to Stansby (1976), the phase jump occurs at $f_c/f_0 = 0.86$, so between cases IV and V. Figure 3.43 shows the lift and drag coefficients versus non-dimensional time for cases II, IV and V. The phase shift is not observed in the present simulations,

since lift and motion stay in phase in all the cases.

## 3.8 Summary

In this chapter the differences in results obtained with different turbulence modeling techniques are analyzed. It is first shown that the use of an inadequate time step, in the particular case of a URANS simulation with the $k$-$\tau$ Speziale model, will have a small effect on global average quantities such as the Strouhal number, the average drag coefficient, and separation angle, but will be noticeable when looking at the pressure coefficient around the cylinder, or the evolution of velocity along the centerline, which reveals that a simulation with a too large time step is unable to properly resolve the recirculation zone and wake.

The comparison between two- and three-dimensional simulations using the $k$-$\tau$ Speziale model revealed again a relative insensitivity of global average quantities, but an important inability of the two-dimensional simulations to yield an accurate pressure coefficient or velocity evolution. In particular, the drag signal from a two-dimensional computation is not smooth as it should be in a URANS simulation of this flow, which shows a difficulty in resolving the sensitive flow motions that are responsible for the drag. Thus, a two-dimensional URANS type simulation may be used to resolve global quantities but not to observe the detailed scales and pressure.

Detailed analysis of the URANS simulations reveals that the Spalart-Allmaras model is unable to capture the separation point properly, the flow remaining attached for too long, which causes the recirculation zone to be too small and the velocity profiles in the near wake inaccurate. Thus, the average drag coefficient is over-estimated by 25% but the Strouhal number remains accurate and the fluctuating velocity profiles are close to the DNS data in the literature.

The $k$-$\tau$ Speziale turbulence model predicts all global quantities accurately, and

yields good velocity profiles along the wake as well as adequate pressure distribution on the cylinder wall even though the back pressure is overestimated. When analyzing the velocity fluctuation, one should be careful since the turbulent kinetic energy, $k$, which is linked to the velocity fluctuations is used as a model variable; hence the value of $k$ computed as part of the simulations contains the modeled fluctuations (not seen by the computational grid), while the value of $u_{i_{rms}}$ from the statistics contains only the resolved part of the fluctuations: one needs to add the resolved and modeled turbulent kinetic energies to obtain the total turbulent kinetic energy of the flow. Since there is no way to separate the contributions of the different velocity components from the fluctuating magnitude in the turbulent kinetic energy, one cannot obtain the individual velocity fluctuations. Thus, the isotropic turbulence models used in conjunction with the computation of the turbulent kinetic energy do not allow for a direct calculation of individual fluctuating velocities, and hence direct comparison between experiments and simulations is not possible without the use of a relation which resolves the anisotropy.

Overall, whether Fluent or SPARC are used, the Spalart-Allmaras turbulence model is somewhat inaccurate in predicting the dynamics of the vortex shedding, in particular the location of the separation point. Thus, overall, the inaccuracy in drag, pressure coefficient, and separation angle can be assumed to come from the inability of the Spalart-Allmaras model to properly resolve the flow past a cylinder in the sub-critical regime, and not to the solution and discretization methodology. In particular, the fact that the trip term of the Spalart-Allmaras model is not implemented in SPARC can not explain the inaccuracy of the results. On the other hand, discrepancies between SPARC and Fluent simulation results may be due to the difference in dissipation and numerical schemes, which cannot be chosen or controlled in the commercial package.

The application of LES and VLES to the flow around a stationary cylinder revealed, as expected, small eddies that are not visible in URANS simulation results

and are more numerous in LES than in VLES results. Furthermore, the three-dimensionality as reflected in the variation of flow properties along the spanwise direction is significantly more important in LES than in URANS simulations. Both large and very large eddy simulations revealed the formation on the upper and lower surfaces of secondary eddies in addition to the large vortices; these small structures rotate in a direction opposite to the large ones, and seem to remain visible when the flow is averaged in time. When comparing the details of pressure and skin friction coefficient, both eddy simulations are very close, but the LES is capable of better capturing the dynamics in the boundary layer as reflected by the skin friction. This trends are clear from the data considered here, but the statistics have not been carried on a long enough time for us to be able to trust the precise values of the mean quantities. These simulations are still running.

The investigation of the transversely oscillating cylinder presented here is of preliminary nature. It seems that the lock-in region starts at significantly lower motion frequencies than observed in the experimental results available in the literature. This may be due to the inherent difficulties of numerical simulations to capture the very subtle triggering phenomena which may be responsible for the establishment of vortex shedding at a frequency different from the motion one at the transitional regime of $Re_D = 3600$ simulated here, and to the fact that the simulations carried out are two-dimensional. No numerical simulations close to this Reynolds number are available in the literature, and further investigation is required.

# Chapter 4

# Conclusions and Further Work

The main purpose of this study was to compare the accuracy of turbulence modeling techniques for the simulation of vortex shedding phenomena, including turbulence models for Unsteady Reynolds-Averaged Navier-Stokes equations (URANS), as well as subgrid-scale models for large eddy simulation (LES). The investigation focuses on the flow over stationary and transversely oscillating circular cylinders, at Reynolds numbers of 3900 and 3600, respectively.

A unique contribution of this work is a comparison of results obtained with the same numerical procedure, discretization algorithms, and artificial dissipation but different turbulence modeling techniques in order to properly differentiate between errors due to numerical and to modeling aspects, which is particularly difficult in LES since the grid determines both the discretization of the governing equations and the cut off between the resolution of the equations and the sub-grid scale modeling of unresolved scales.

We carried out a thorough validation of the numerical code and discretization methods, as well as the turbulence models and subgrid-scale models considered, namely: the one-equation Spalart-Allmaras model for the solution of URANS equations [Spalart & Allmaras (1994)]; the two-equation $k$-$\tau$ model by Speziale *et al.*

(1992) for URANS closure; an LES with the Smagorinsky subgrid-scale model; and a Very-Large-Eddy Simulation (VLES) with the adaptive $k$-$\tau$ model proposed by Magagnato & Gabi (2002).

Through the study of the flow around the stationary cylinder, it is shown that the use of an inadequate time step, in the particular case of a URANS simulation with the $k$-$\tau$ Speziale model, has a small effect on global average quantities such as the Strouhal number, the average drag coefficient, and separation angle, but a noticeable impact on the pressure coefficient around the cylinder, as well as on the evolution of velocity along the centerline. This shows that simulations with too large a time step are unable to properly resolve the recirculation zone and wake.

A relative insensitivity of global average quantities to three-dimensional resolution was observed by comparing two- and three-dimensional simulations with the $k$-$\tau$ Speziale model, while the two-dimensional simulations yield an inaccurate pressure coefficient distribution and velocity profile evolution. Thus, a two-dimensional URANS type simulation may be used to resolve global quantities but not to observe the details of the scales near solid surfaces.

Detailed analysis of three-dimensional URANS simulations reveals that the Spalart-Allmaras model is unable to properly resolve the flow past a cylinder in the sub-critical regime: it does not capture the separation point properly and the flow remains attached to the cylinder for too long. This results in too small a mean recirculation zone, under-estimated back-pressure, and up to 25% over-estimation of the drag. Yet, this simple model provides an accurate Strouhal number and good fluctuating velocity profiles.

The observations concerning the Spalart-Allmaras model and drawn from the simulations carried out using the research code SPARC are confirmed by the results obtained with the commercial CFD code Fluent. The small discrepancies between SPARC and Fluent computations can be attributed to the difference in numerical

schemes and associated artificial dissipation, which cannot be chosen nor controlled in the commercial package.

The $k$-$\tau$ Speziale turbulence model predicts all global quantities accurately, and yields good velocity profiles along the wake as well as adequate pressure distribution on the cylinder wall. The isotropic turbulence models used in conjunction with the computation of the turbulent kinetic energy do not allow for a direct calculation of individual fluctuating velocities, and hence direct comparison between experiments and simulations is not possible without the use of a relation which resolves the anisotropy.

The application of LES and VLES to the flow around a stationary cylinder revealed, as expected, small eddies that are not visible in URANS simulation, with strong three-dimensionality as reflected in the variation of flow properties along the spanwise direction. The LES and VLES further revealed the formation on the upper and lower surfaces of secondary eddies in addition to the large vortices which remain visible in the time-averaged flow. The LES captures the dynamics in the laminar boundary layer as reflected in the skin friction values, even though it makes use of a constant coefficient Smagorinsky subgrid-scale model.

In the study of the transversely oscillating cylinder at $Re_D = 3600$ with two-dimensional URANS $k$-$\tau$ Speziale simulations, the lock-in region starts at significantly lower motion frequencies than observed in the experiments of Stansby (1976). This may be due to the inherent difficulties that numerical simulations have in capturing the subtle phenomena responsible for triggering vortex shedding at a frequency that is different from the motion frequency, at least in the transitional regime studied here, and to the fact that the simulations are two-dimensional. No numerical studies close to this Reynolds number are available in the literature, and further investigation is required.

Additional LES and VLES simulations are required over extended periods in order to obtain better statistics. Further work will also include LES with the dynamic

Smagorinsky model by Germano *et al.* (1991) and the dynamic mixed model by Zang *et al.* (1993), which are expected to enhance accuracy in resolving the dynamics, in particular near the wall, compared to the constant-coefficient approach. These dynamic models have already been implemented in the computational code.

The investigation of the transversely oscillating cylinder presented here is of preliminary nature, and further investigation is required using three-dimensional URANS simulations with the $k$-$\tau$ Speziale model, as well as large eddy simulations with constant-coefficient, dynamic, and dynamic-mixed subgrid-scale models.

# Appendix A

# Turbulence Models and Subgrid-Scale Models

## A.1 Spalart-Allmaras One-Equation Model

In the Spalart & Allmaras (1994) one-equation model for URANS closure, the eddy viscosity is solved through the intermediary variable $\breve{\mu}$ defined by

$$\mu_t = \breve{\mu} f_{\mu_1}(\chi)$$

where

$$\chi \equiv \frac{\breve{\mu}}{\mu}.$$

The partial differential equation for this variables reads

$$\begin{aligned} \frac{D\breve{\mu}}{Dt} &= c_{b_1}\left[1 - f_{t_2}\right]\breve{S}\breve{\mu} + \frac{1}{\sigma}\left[\nabla\cdot\left(\left(\mu+\breve{\mu}\right)\nabla\breve{\mu}\right) + c_{b_2}\left(\nabla\breve{\mu}\right)^2\right] \\ &\quad - \left[c_{w_1} f_w - \frac{c_{b_1}}{\kappa^2} f_{t_2}\right]\left[\frac{\breve{\mu}}{d}\right]^2 + f_{t_1}\Delta U^2 \end{aligned}$$

where $D/Dt \equiv \partial/\partial t + u_i \partial/\partial x_i$ is the total derivative, and

$$
\begin{aligned}
c_{b_1} &= 0.1355 \\
c_{b_2} &= 0.622 \\
c_{t_1} &= 1 \\
c_{t_2} &= 2 \\
c_{t_3} &= 1.1 \\
c_{t_4} &= 2 \\
c_{v_1} &= 7.1 \\
c_{w_1} &= \frac{c_{b_1}}{\kappa^2} + \frac{1+c_{b_2}}{\sigma} \\
c_{w_2} &= 0.3 \\
c_{w_3} &= 2 \\
f_{t_1} &= c_{t_1} g_t \exp\left[-c_{t_2} \frac{\omega_t^2}{\Delta U^2}\left(d^2 + g_t^2 d_t^2\right)\right] \\
f_{t2} &= c_{t3} \exp\left(-c_{t4}\chi^2\right) \\
f_{v1} &= \frac{\chi^3}{\chi^3 + c_{v_1}^3} \\
f_{v2} &= 1 - \frac{\chi}{1+\chi f_{v_1}} \\
f_w &= g\left[\frac{1+c_{w_3}^6}{g^6 + c_{w_3}^6}\right]^{1/6} \\
g &= r + c_{w_2}\left(r^6 - r\right) \\
g_t &\equiv \min\left(0.1, \frac{\Delta U}{\omega_t \Delta x}\right) \\
r &\equiv \frac{\breve{\mu}}{\breve{S}\kappa^2 d^2} \\
\breve{S} &\equiv S + \frac{\tilde{\mu}}{\kappa^2 d^2} f_{v_2} \\
S_{ij} &\equiv \frac{1}{2}\left(\frac{\partial \overline{u_i}}{\partial x_j} + \frac{\partial \overline{u_j}}{\partial x_i}\right) \\
\kappa &= 0.41 \\
\omega &= \sqrt{\Omega_{ij}\Omega_{ij}} \qquad \text{for} \qquad \Omega_{ij} = \frac{\partial \overline{u_i}}{\partial x_j} - \frac{\partial \overline{u_j}}{\partial x_i} \\
\sigma &= 2/3
\end{aligned}
$$

$d$ is the distance to the wall

$\Delta U$ is the norm of the difference between the trip velocity (usually zero) and the velocity of the field point under consideration

$\Delta x$ is the grid spacing along the wall at the trip

$\omega_t$ is the vorticity at the wall at the trip point

For numerical stability, limits are imposed on some of the terms as follows: the term $(-c_{t_4}\chi^2)$ in $f_{t_2}$ is limited to a minimum value of $-30$, and the function $g$ is limited to a minimum value of $10^{-5}$.

The trip term in the Spalart-Allmaras model — last term in equation (2.44) — should not significantly affect the ability of the model to predict the flows under consideration in this study since transition to turbulence does not take place in the boundary layer, and hence tripping is not implemented in the computational code.

## A.2 $k$-$\tau$ Model by Speziale *et al.*

The two-equation $k$-$\tau$ model for URANS closure by Speziale *et al.* (1992) computes the eddy viscosity as

$$\mu_t = \overline{\rho}\, C_\mu f_\mu k\tau$$

with the model equations for the turbulent kinetic energy, $k$, and turbulent time scale, $\tau$, being expressed in terms of $\nu = \mu/\overline{\rho}$ and $\nu_t = \mu_t/\overline{\rho}$ by

$$\frac{Dk}{Dt} = \tau_{ij}\frac{\partial \overline{u_i}}{\partial x_j} - \frac{k}{\tau} + \frac{\partial}{\partial x_i}\left[\left(\nu + \frac{\nu_t}{\sigma_k}\right)\frac{\partial k}{\partial x_i}\right]$$

$$\begin{aligned}\frac{D\tau}{Dt} &= (1 - C_{\epsilon_1})\frac{\tau}{k}\tau_{ij}\frac{\partial \overline{u_i}}{\partial x_j} + (C_{\epsilon_2} f_2 - 1) + \frac{2}{k}\left(\nu + \frac{\nu_t}{\sigma_{\tau 1}}\right)\frac{\partial k}{\partial x_i}\frac{\partial \tau}{\partial x_i} \\ &\quad -\frac{2}{\tau}\left(\nu + \frac{\nu_t}{\sigma_{\tau 1}}\right)\frac{\partial \tau}{\partial x_i}\frac{\partial \tau}{\partial x_i} + \frac{\partial}{\partial x_i}\left[\left(\nu + \frac{\nu_t}{\sigma_{\tau 1}}\right)\frac{\partial \tau}{\partial x_i}\right]\end{aligned}$$

where

$$\begin{aligned} C_\mu &= 0.09 \\ C_{\epsilon_1} &= 1.44 \\ C_{\epsilon_2} &= 1.83\left[1 - (2/9)\exp\left(-Re_t^2/36\right)\right] \\ f_2 &= \left[1 - \exp\left(-y^+/A_2\right)\right]^2 \end{aligned}$$

$$f_\mu = \left(1 + 3.45/\sqrt{Re_t}\right) \tanh\left(y^+/70\right)$$
$$A_2 = 4.9.$$

## A.3 Adaptive $k$-$\tau$ Model by Magagnato *et al.*

The filter length is chosen locally between the spatial filter width (determined by the grid)

$$L_s = 2\Delta = 2\left(\Delta x \times \Delta y \times \Delta_z\right)^{1/3}$$

and the temporal filter width

$$L_t = |u| \times \Delta t$$

where $\Delta x$, $\Delta y$, $\Delta z$ are the grid cell sizes in the three coordinate directions, $\Delta t$ is the simulation time step, and $|u|$ is the magnitude of the flow velocity in the considered cell. Then the filter width is taken to be

$$\Delta = \max\left(L_s\,,\, L_t\right)$$

Through this filter width, the turbulent kinetic energy, $k$, and the turbulent time scale, $\tau$, are decomposed into a resolved and an unresolved part as

$$k = \overline{k} + k' \quad \text{and} \quad \tau = \overline{\tau} + \tau'$$

The resolved time scale is determined from the turbulent kinetic energy through the relation

$$\overline{\tau} = \frac{\Delta}{\sqrt{k'}}.$$

The unresolved, or subgrid-scale, parts are modeled through the non-linear eddy

viscosity $k$-$\tau$ model by Craft *et al.* (1995), which uses the transport equation for $k$

$$\frac{\partial(\rho k')}{\partial t} + \frac{\partial(\rho u_i k')}{\partial x_i} = \frac{\partial}{\partial x_i}\left[(\mu + \mu_k)\frac{\partial k'}{\partial x_i}\right] - \rho\overline{u_i' u_j'}\frac{\partial u_i}{\partial x_j} - \rho\frac{k'\left(1 + \frac{\tau'\sqrt{k'}}{\Delta}\right)}{\tau'}$$

and the transport equation for $\tau$

$$\begin{aligned}\frac{\partial(\rho\tau')}{\partial t} + \frac{\partial(\rho u_i \tau')}{\partial x_i} &= \frac{\partial}{\partial x_i}\left[(\mu + \mu_\tau)\frac{\partial \tau'}{\partial x_i}\right] - (1 - c_{\epsilon_1})\frac{\tau'}{k'}\rho\overline{u_i' u_j'}\frac{\partial u_i}{\partial x_j} \\ &\quad + \rho\left[c_{\epsilon_2} - \left(1 + \frac{\tau'\sqrt{k'}}{\Delta}\right)\right] + \frac{2}{k'}(\mu + \mu_k)\frac{\partial k'}{\partial x_i}\frac{\partial \tau'}{\partial x_i} \\ &\quad - \frac{2}{\tau'}(\mu + \mu_k)\frac{\partial \tau'}{\partial x_i}\frac{\partial \tau'}{\partial x_i} - 0.06 S \tau'^3\left(\frac{\partial^2 u_i}{\partial x_k \partial x_j}\right)\end{aligned}$$

where

$$\begin{aligned} S &= \tau'\sqrt{S_{ij}S_{ij}/2} \\ S_{ij} &= \tfrac{\partial u_i}{\partial x_j} + \tfrac{\partial u_j}{\partial x_i} - \tfrac{2}{3}\tfrac{\partial u_i}{\partial x_j}\delta_{ij} \\ c_{\epsilon_1} &= 1.44 \\ c_{\epsilon_2} &= 1.92\left[1 - 0.3\exp\left(-Re_t^2\right)\right] \\ Re_t &= \tfrac{k^2}{\nu\epsilon} \end{aligned}$$

The eddy viscosity is given by

$$\mu_t = \rho\, c_\mu\, f_\mu\, k'\, \tau'$$

with

$$\begin{aligned} c_\mu &= \frac{0.3}{1 + 0.35 S^{3/2}}\left[1 - \exp\left(-\frac{0.36}{\exp(-0.75S)}\right)\right] \\ f_\mu &= 1 - \exp\left[-\left(\frac{Re_t}{90}\right)^1/2 - \left(\frac{Re_t}{400}\right)^2\right] \end{aligned}$$

where $\epsilon = \nu \overline{\partial u_i'/\partial x_j \, \partial u_i'/\partial x_j}$ is the turbulent dissipation rate.

Then the Reynolds stress is modeled as

$$
\begin{aligned}
-\overline{\rho u_i'' u_j''} = -\overline{\rho}\widetilde{u_i' u_j'} = \mu_t S_{ij} - \frac{2}{3}k'\delta_{ij} - c_1\mu_t\tau'\left(S_{ik}S_{kj} - \frac{1}{3}S_{kl}S_{kl}\delta_{ij}\right) \\
- c_2\mu_t\tau'\left(\Omega_{lk}S_{kj} + \Omega_{jk}S_{kj}\right) - c_3\mu_t\tau'\left(\Omega_{lk}\Omega_{jk} + \frac{1}{3}\Omega_{kl}\Omega kl\delta_{ij}\right) \\
+ c_\mu\mu_t\tau'^2\left\{c_4\left(S_{kl}\Omega_{lj} + S_{kj}\Omega_{li} - \frac{2}{3}S_{km}\Omega_{lm}\delta ij\right) + S_{kl}\right. \\
\left. + c_5\left(S_{ik}S_{jl} - \frac{1}{3}S_{mk}S_{ml}\delta_{ij}\right)S_{kl} + c_6 S_{ij}S_{kl}S_{kl} + c_7 S_{ij}\Omega_{kl}\Omega_{kl}\right\}
\end{aligned}
$$

where

$$\Omega_{ij} = \frac{\partial u_i}{\partial x_j} - \frac{\partial u_j}{\partial x_i}$$

and the model constants have the values

$$
\begin{aligned}
c_1 &= -0.1 \\
c_2 &= 0.1 \\
c_3 &= 0.26 \\
c_4 &= -0.081 \\
c_5 &= 0 \\
c_6 &= 0.0405 \\
c_7 &= -0.0405.
\end{aligned}
$$

Finally, the subgrid-scale Reynolds stress is obtained from the relation

$$-\overline{\rho u_i'' u_j''} = -\overline{\rho}\widetilde{u_i'' u_j''} = \rho c_\mu k'\tau' S_{ij} - \frac{2}{3}\rho k'\delta_{ij} - \left(\rho v_i' v_j' + \frac{2}{3}\rho k'\delta_{ij}\right),$$

or simply

$$-\overline{\rho u_i'' u_j''} = -\overline{\rho}\widetilde{u_i'' u_j''} = \rho c_\mu k'\tau' S_{ij} - \rho v_i' v_j',$$

where $v_i'$ are random velocities calculated at each time step through a Langevin-type equation

$$(v_i')^n = (v_i')^{n-1}\left(1 - \frac{\Delta t}{\tau'}\right) + Z_i^n \sqrt{\frac{\Delta t}{\tau'}\left(2 - \frac{\Delta t}{\tau'}\right)\frac{2}{3}k'}$$

using the independent random number $Z_i \in (-1\,,\,1)$ with the initialization at the first time step $(v_i')^0 = \sqrt{\frac{2}{3}k'}$ and $\langle((v_i')^n)^2\rangle = \frac{2}{3}k'$. Further details on the model and its derivation can be found in Craft *et al.* (1995) and Magagnato & Gabi (2002).

# Appendix B

# Additional Results

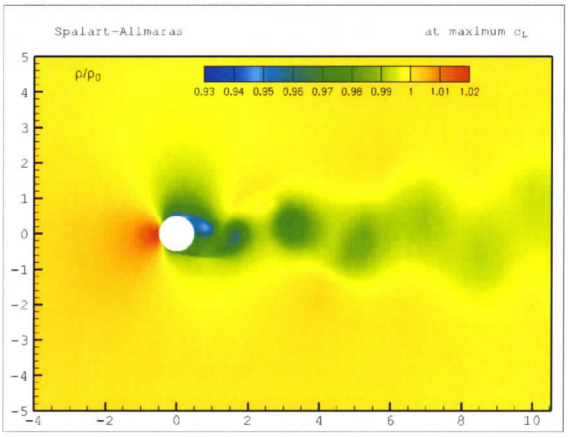


(a) SA $\rho$ at max $c_L$

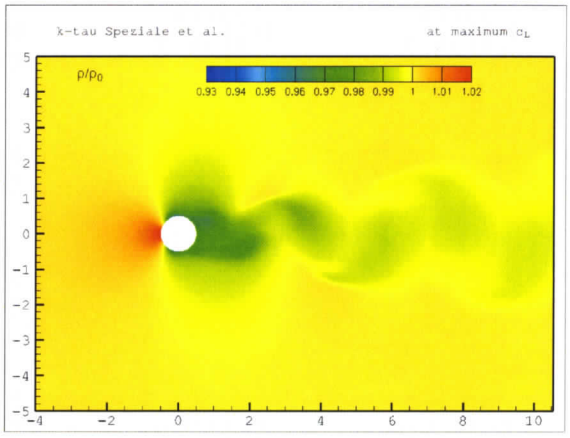


(b) Sp $\rho$ at max $c_L$

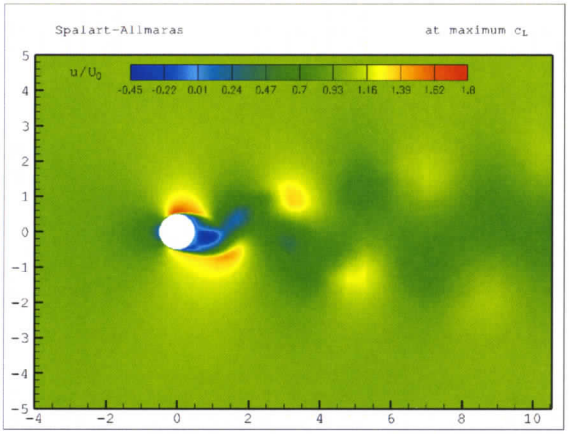


(c) SA $u$ at max $c_L$

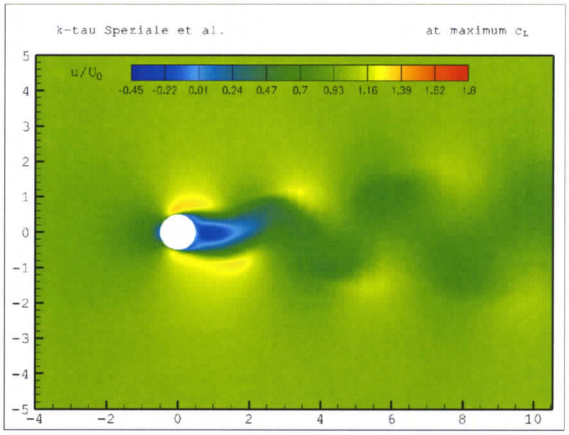


(d) Sp $u$ at max $c_L$

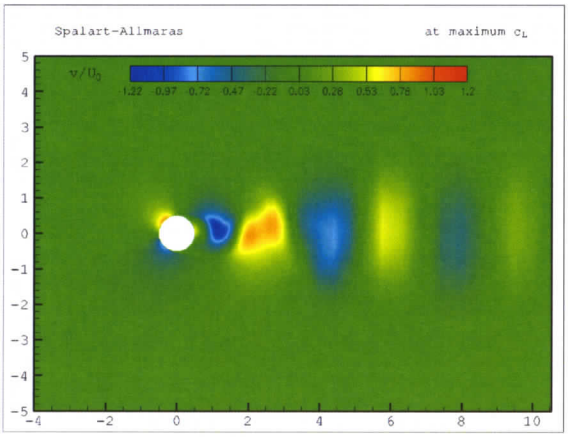


(e) SA $v$ at max $c_L$

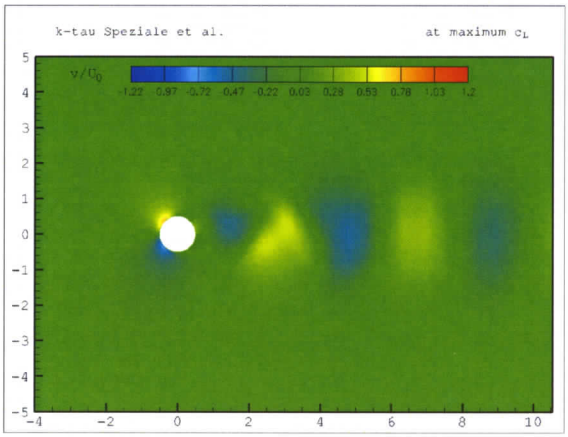


(f) Sp $v$ at max $c_L$

Figure B.1: Instantaneous non-dimensional density, longitudinal and normal velocity components for the flow past a static circular cylinder at $Re_D = 3900$ at time corresponding to a local maximum in $c_L$: comparison of URANS models Spalart-Almaras (left) and k-$\tau$ Speziale et al. (right).

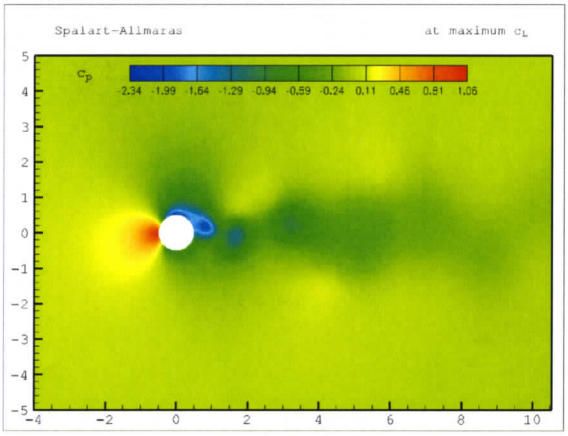


(a) SA $c_p$ at max $c_L$

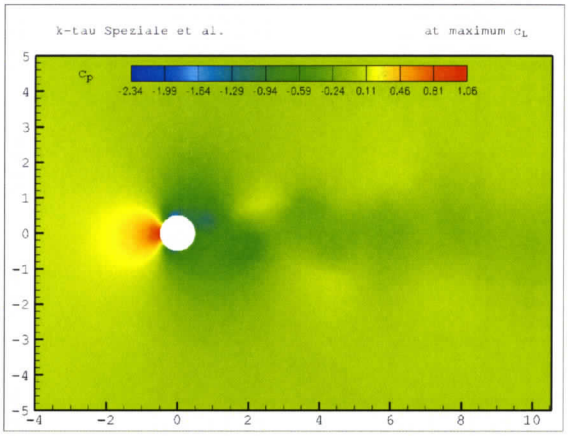


(b) Sp $c_p$ at max $c_L$

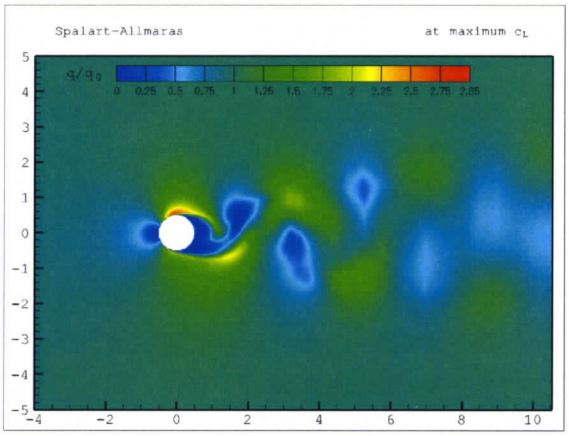


(c) SA $q$ at max $c_L$

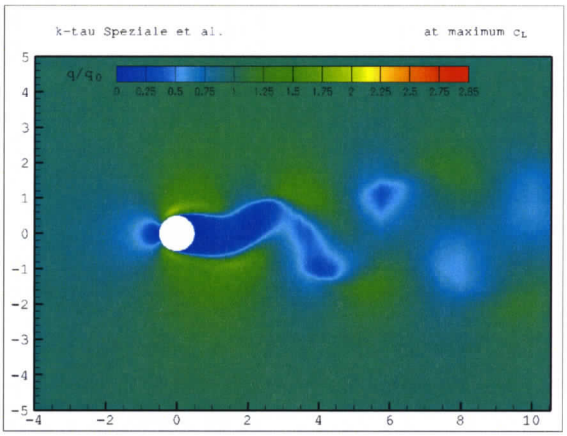


(d) Sp $q$ at max $c_L$

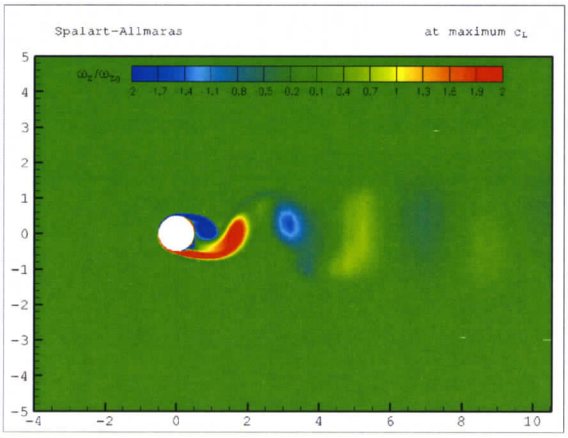


(e) SA $\omega_z$ at max $c_L$

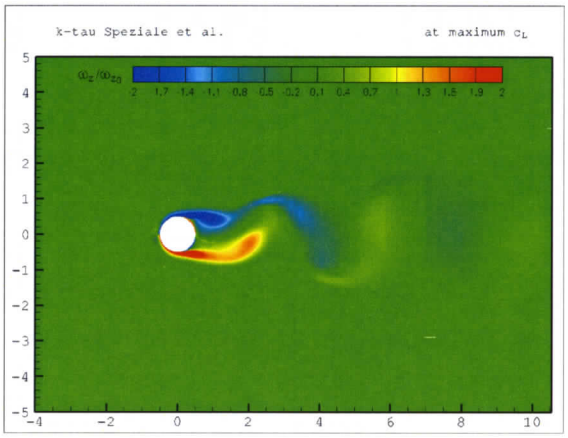


(f) Sp $\omega_z$ at max $c_L$

Figure B.2: Instantaneous pressure coefficient and non-dimensional dynamic pressure for the flow past a static circular cylinder at $Re_D = 3900$ at the time corresponding to a local maximum in $c_L$: comparison of URANS models Spalart-Almaras (left) and k-$\tau$ Speziale et al. (right).

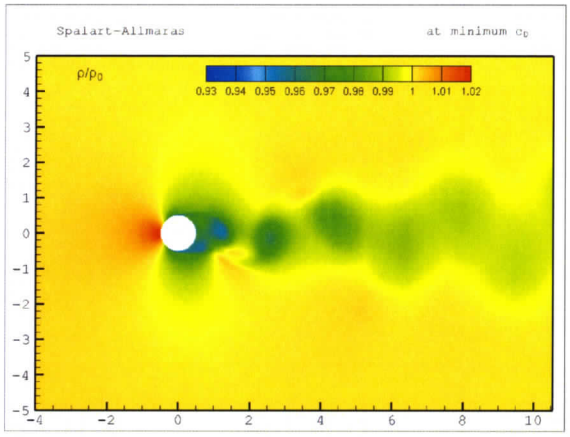


(a) SA $\rho$ at min $c_D$

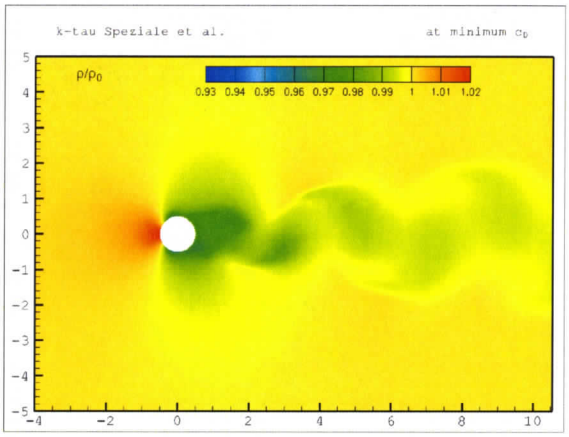


(b) Sp $\rho$ at min $c_D$

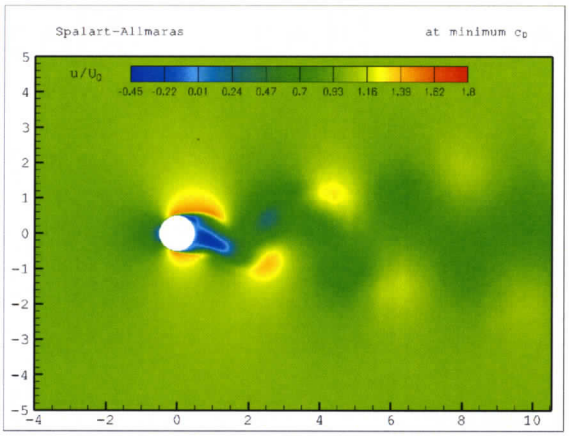


(c) SA $u$ at min $c_D$

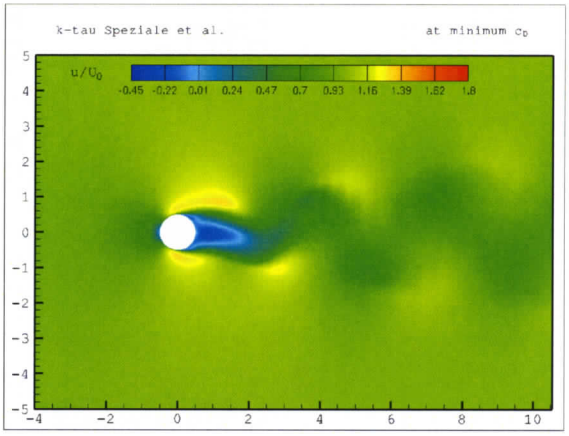


(d) Sp $u$ at min $c_D$

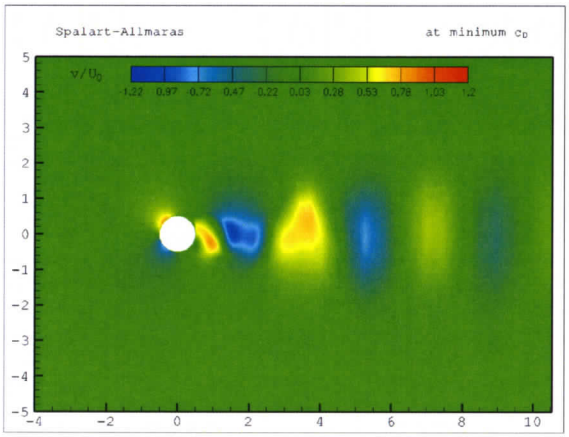


(e) SA $v$ at min $c_D$

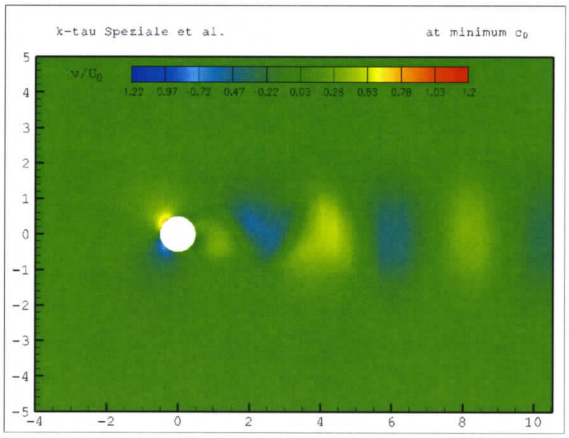


(f) Sp $v$ at min $c_D$

Figure B.3: Instantaneous non-dimensional longitudinal and normal velocity components for the flow past a static circular cylinder at $Re_D = 3900$ at time corresponding to a local minimum in $c_D$: comparison of URANS models Spalart-Almaras (left) and k-$\tau$ Speziale et al. (right).

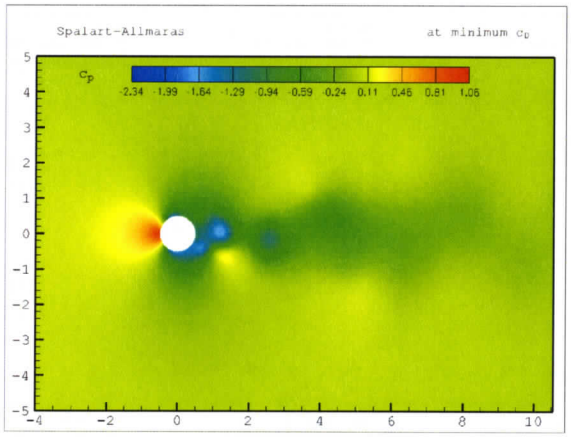


(a) SA $c_p$ at min $c_D$

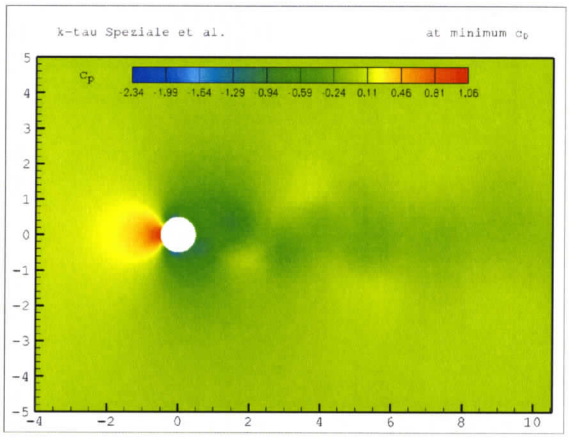


(b) Sp $c_p$ at min $c_D$

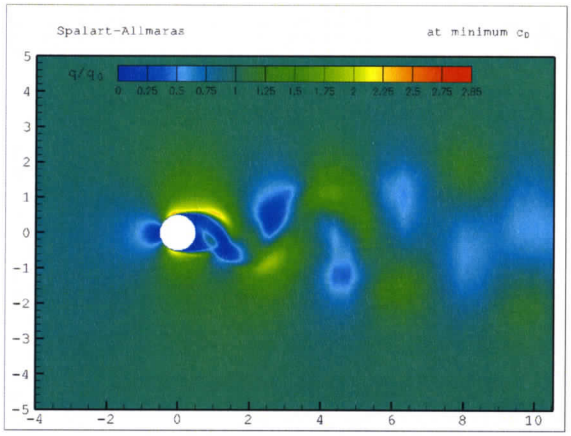


(c) SA $q$ at min $c_D$

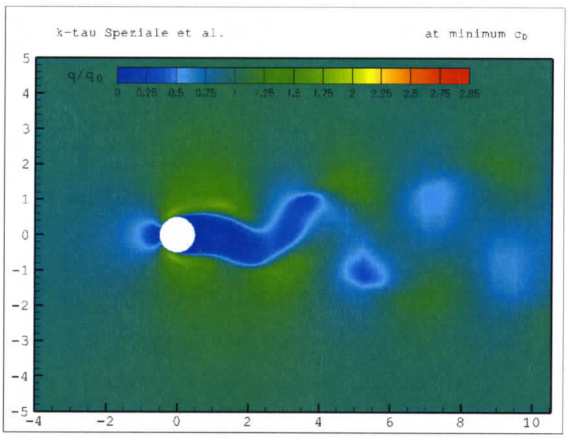


(d) Sp $q$ at min $c_D$

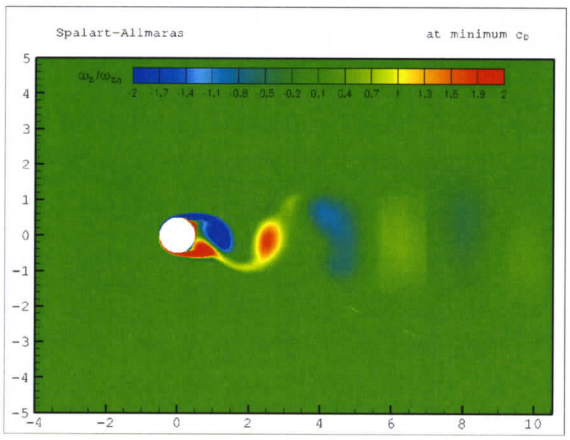


(e) SA $\omega_z$ at min $c_D$

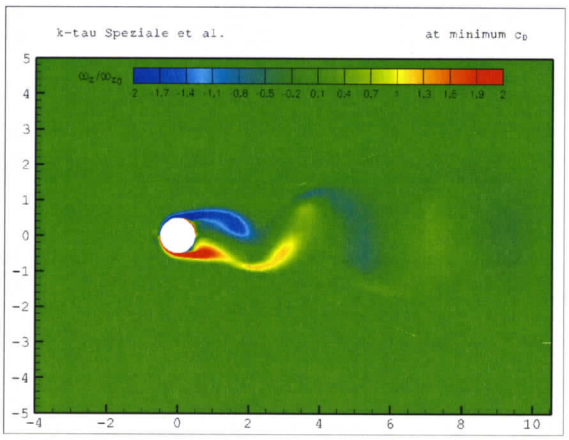


(f) Sp $\omega_z$ at min $c_D$

Figure B.4: Instantaneous non-dimensional density and pressure coefficient the flow past a static circular cylinder at $Re_D = 3900$ at the time corresponding to a local minimum in $c_D$: comparison of URANS models Spalart-Almaras (left) and k-$\tau$ Speziale et al. (right).

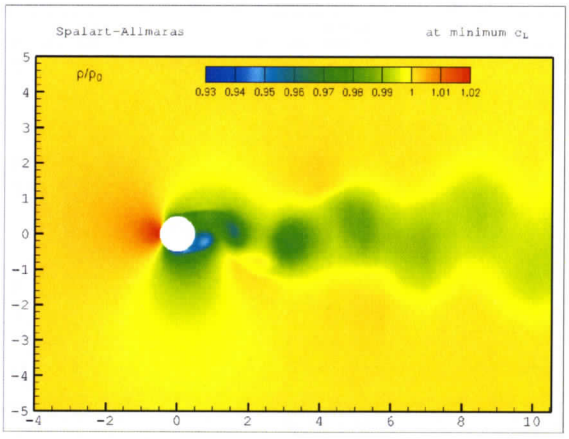


(a) SA $\rho$ at min $c_L$

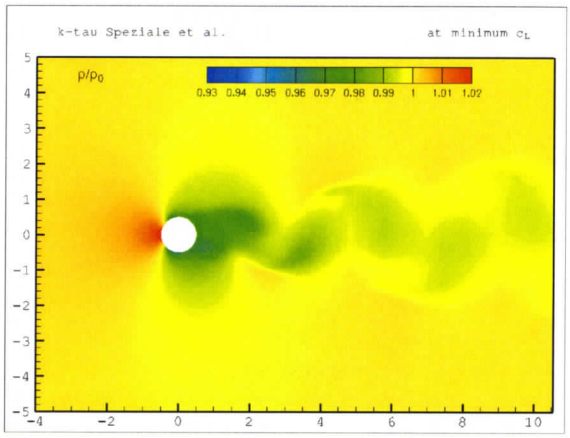


(b) Sp $\rho$ at min $c_L$

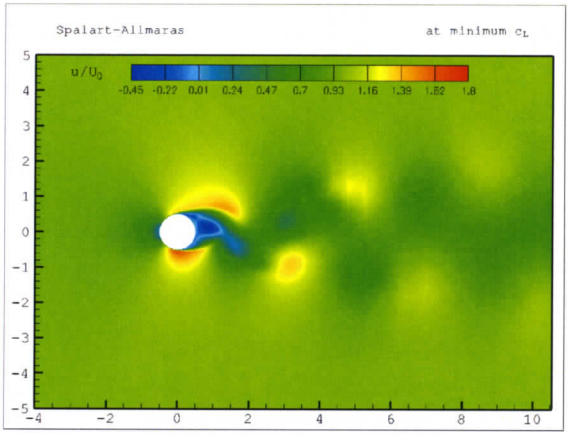


(c) SA $u$ at min $c_L$

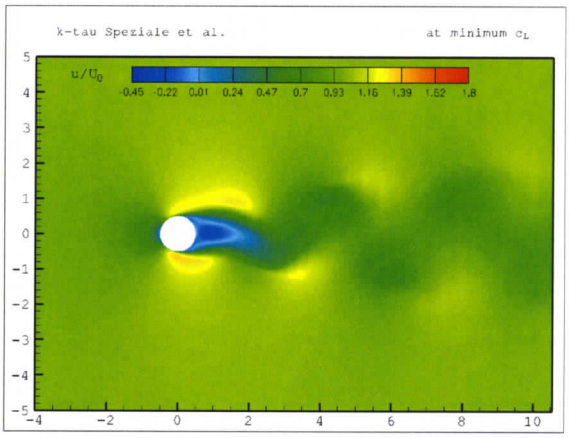


(d) Sp $u$ at min $c_L$

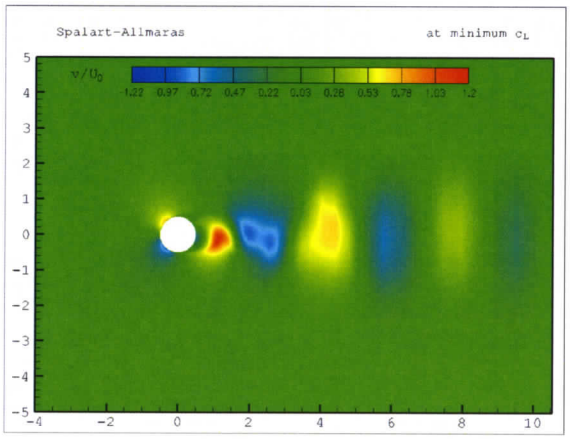


(e) SA $v$ at min $c_L$

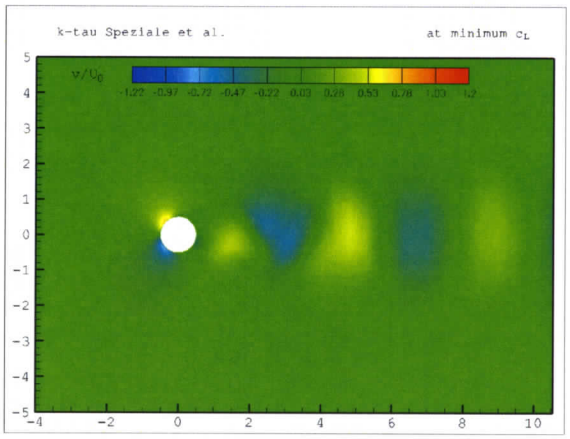


(f) Sp $v$ at min $c_L$

Figure B.5: Instantaneous non-dimensional density, longitudinal and normal velocity components for the flow past a static circular cylinder at $Re_D = 3900$ at time corresponding to a local minimum in $c_L$: comparison of URANS models Spalart-Almaras (left) and k-$\tau$ Speziale et al. (right).

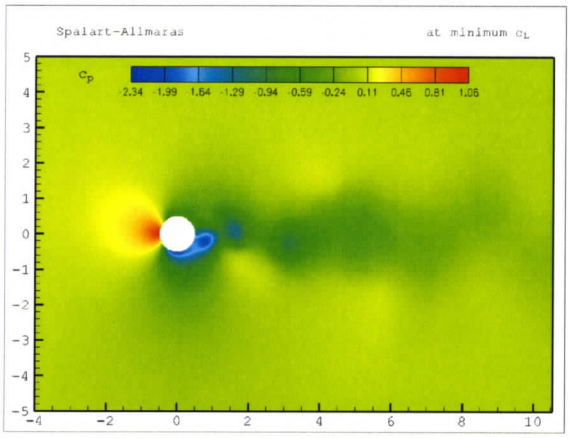


(a) SA $c_p$ at min $c_L$

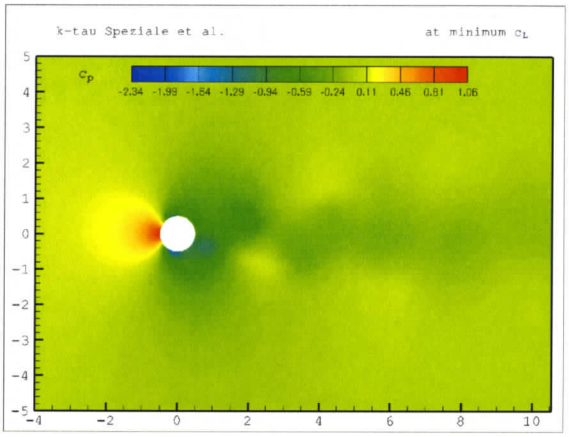


(b) Sp $c_p$ at min $c_L$

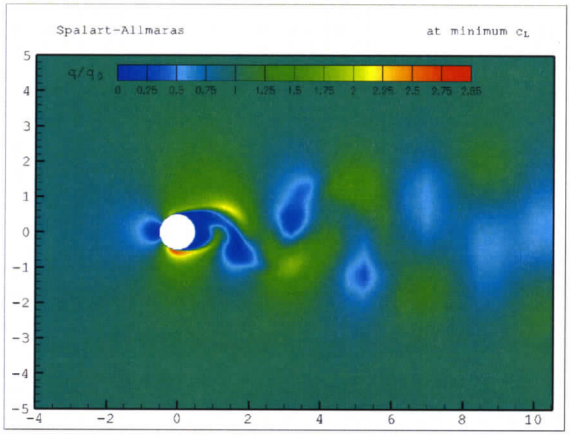


(c) SA $q$ at min $c_L$

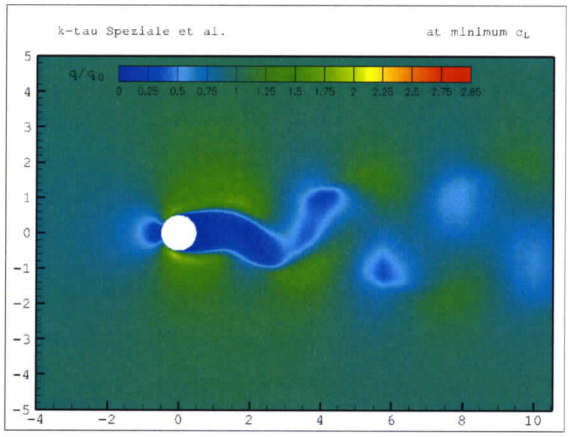


(d) Sp $q$ at min $c_L$

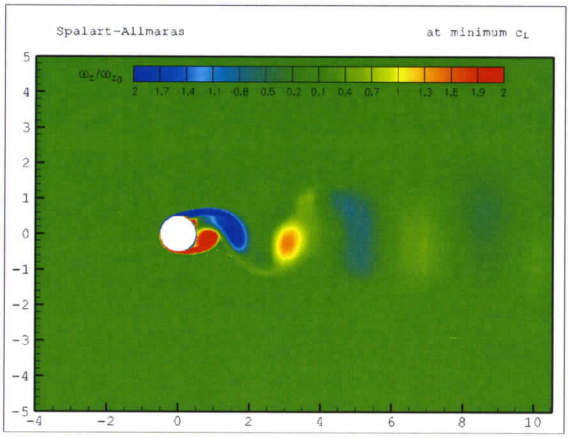


(e) SA $\omega_z$ at min $c_L$

Figure B.6: Instantaneous pressure coefficient and non-dimensional dynamic pressure for the flow past a static circular cylinder at $Re_D = 3900$ at the time corresponding to a local minimum in $c_L$: comparison of URANS models Spalart-Almaras (left) and k-$\tau$ Speziale et al. (right).

# References

ALLMARAS, S.R. 1993 Contamination of laminar boundary layers by artificial dissipation in navier-stokes solutions. In *Numerical Methods for Fluid Dynamics* (ed. M.J. Baines & K.W. Morton). Oxford University Press.

ANAGNOSTOPOULOS, P., ILIADIS, G. & RICHARDSON, S. 1996 Numercial study of the blockage effects on viscous flow past a circular cylinder. *International Journal for Numerical Methods in Fluids* **22**, 1061–1074.

ANAGNOSTOPOULOS, P. & MINEAR, R. 2004 Blockage effect of oscillatory flow past a fixed cylinder. *Applied Ocean Research* **26**, 147–153.

ANDERSON, J. D. 2003 *Modern Compressible Flow with Historical Perspective*, 3rd edn. McGrawHill.

ARNONE, A., LIOU, M.-S. & POVINELLI, L.A. 1995 Integration of Navier-Stokes equations using dual time stepping and multigrid method. *AIAA Journal* **33** (6), 985–990.

BARDINA, J. 1983 Improved turbulence models based on large eddy simulation of homogeneous, incompressible, turbulent flows. PhD thesis, Dept. of Mechanical Engineering, Stanford University.

BARDINA, J., FERZIGER, J. H. & REYNOLDS, W.C. 1980 Improved subgrid models for large eddy simulation. *AIAA paper 80-1357* .

BEARMAN, P.W. 1984 Vortex shedding from oscillating bluff bodies. *Annual Review of Fluid Mechanics* **16**, 195–222.

BEAUDAN, P. 1994 Numerical experiments on the flow past a circular cylinder at sub-critical reynolds number. PhD thesis, Dept. of Mechanical Engineering, Stanford University.

BÉNARD, H. 1908 Formation de centres de giration à l'arrière d'un obstacle en mouvement. *Comptes Rendus de l'Academie des Sciences* **147**, 839–842.

BÉNARD, H. 1926 On the frequency law of alternative eddies behind an obstacle (titre francais?). *Comptes Rendus de l'Academie des Sciences* **182**, 1375–1377.

BERGER, E. & WILLE, R. 1972 Periodic flow phenomena. *Annual Review of Fluid Mechanics* **4**, 313–340.

BISHOP, R.E.D. & HASSAN, A.Y. 1964 The lift and drag forces on a circular cylinder oscillating in a flowing fluid. *Proceedings of the Royal Society (London)* **A 277**, 51–75.

BLACKBURN, H. M. & HENDERSON, R. D. 1999 A study of the two-dimensional flow past an oscillating cylinder. *Journal of Fluid Mechanics* **385**, 255–286.

BREUER, M. 1993 A dual time-stepping method for 3-d, viscous, incompressible vortex flows. *Computers Fluids* **22** (4/5), 467–484.

BREUER, M. 1998 Numerical and modeling influences on large eddy simulation for the flow past a circular cylinder. *International Journal of Heat and Fluid Flow* **19**, 512–521.

CRAFT, T.J., LAUNDER, B.B. & SUGA, K. 1995 A non-linear eddy viscosity model including sensitivity to stress anisotropy. *10th Symposium on Turbulent Shear Flows, Pennsylvania State University* .

DE PALMA, P., PASCAZIO, G. & NAPOLITANO, M. 2001 Accurate and efficient solutions of unsteady viscous flows. *International Journal of Numerical Methods for Heat and Fluid Flow* **11** (4), 286–307.

DJILALI, N., GARTSHORE, I.S. & SALCUDEAN, M. 1991 Turbulent flow around a bluff rectangular plate. Part II: Numerical predictions. *Journal of Fluids Engineering* **113**, 60–67.

FAVRE, A. 1965 Equations des gas turbulents compressibles. *Journal de Mécanique* **4** (3), 361–421.

FEDERENKO, R.P. 1964 The speed of convergence of one iterative process. *USSR Comp. Math. and Math. Physics* .

FERZIGER, J. H. & PERIĆ, M. 2002 *Computational Methods for Fluid Dynamics*, 3rd edn. Springer.

FRANKE, J. & FRANK, W. 2002 Large eddy simulation of the flow past a circular cylinder at $Re_D = 3900$. *Journal of Wind Engineering and Industrial Aerodynamics* **90**, 1191–1206.

FRÖHLICH, J., RODI, W., KESSLER, PH., PARPAIS, S., BERTOGLIO, J. P. & LAURENCE, D. 1998 Large eddy simulation of flow around a circular cylinders on structured and unstructured grids. In *Numerical Fluid Mechanics* (ed. E.H. Hirschel editor), pp. 319–338. Braunschweig: Vieweg.

GATSKI, T.B., HUSSAINI, M.Y. & LUMLEY, J. L., ed. 1996 *Simulation and Modeling of Turbulent Flows*. Oxford University Press.

GERMANO, M. 1992 Turbulence: the filtering approach. *Journal of Fluid Mechanics* **238**, 325–336.

GERMANO, M. 1996 A statistical formulation of the dynamic model. *Physics of Fluids* **8** (2), 565–570.

GERMANO, M., PIOMELLI, U., MOIN, P. & CABOT, W.H. 1991 A dynamic subgrid-scale eddy viscosity model. *Physics of Fluids* **A3(7)**, 1760–1765.

GOLDSTEIN, S. 1969 Fluid mechanics in the first half of this century. *Annual Review of Fluid Mechanics* **1**.

HINZE, J. O. 1975 *Turbulence*, 2nd edn. McGraw-Hill.

JAMESON, A. 1983 Transonic flow calculations. MAE Report 1651, Mechanical and Aerospace Engineering Dept., Princeton University, Princeton, NJ.

JAMESON, A. 1985 Non-oscillatory shock capturing scheme using flux limited dissipation. In *Lectures in Applied Mathematics* (ed. B.E. Engquist, S. Osher & R.C.J. Sommerville), , vol. 22, pp. 345–370. AMS.

JAMESON, A. 1986 Multigrid algorithms for compressible flow calculations. *Lecture Notes in Mathematics, Springer-Verlag* **1228**, 166–201.

JAMESON, A. 1991 Time dependent calculations using multigrid, with applications to unsteady flow past airfoils and wings. *AIAA Paper 91-1596* .

JAMESON, A. 1995*a* Analysis and design of numerical schemes for gas dynamics, part I: artificial dissipation, upwind biasing, limiters and their effect on accuracy and multigrid convergence. *International Journal of Computational Fluid Dynamics* **4**, 171–218.

JAMESON, A. 1995*b* Analysis and design of numerical schemes for gas dynamics, part II: artificial diffusion and discrete shock structure. *International Journal of Computational Fluid Dynamics* **5**, 1–38.

JAMESON, A., SCHMIDT, W. & TURKEL, E. 1981 Numerical simulations of the Euler equations by finite volume methods using Runge-Kutta time-stepping schemes. *AIAA Paper 81-1259* .

KÁRMÁN, TH. VON 1912 On the mechanism of resistance in fluids. *Physikalische Zeitschrift* pp. 351–358.

KAWAGUTI, M 1953 Numerical solution of the NS equations for the flow around a circular cylinder at reynolds number 40. *Journal of the Physical Society of Japan* **8**, 747–757.

KRAVCHENKO, A. G. & MOIN, P. 2000 Numerical studies of flow over a circular cylinder at $Re_D = 3900$. *Physics of Fluids* **12** (2), 403–417.

LANDAU, L. D. & LIFSCHITZ, E. M. 1959 *Fluid Mechanics*. London: Pergamon.

LEONARD, A. 1974 Energy cascade in large eddy simulations of turbulent fluid flows. *Advances in Geophysics* **18A**, 237–248.

LILLY, D.K. 1967 The representation of small-scale turbulence in numerical simulation experiments. In *Proc. IBM Scientific Computing Symposium on Environmental Sciences* (ed. H.H. Goldstine), pp. 195–210. Yorktown Heights, NY.

LILLY, D.K. 1992 A proposed modification of the Germano subgrid scale closure method. *Physics of Fluids* **A4**, 633–635.

LIOU, M.-S. & STEFFEN, C.J. 1993 A new flux splitting scheme. *Journal of Computational Physics* **107**, 23–39.

LORENZ, E.N. 1993 *The Essence of Chaos*. University of Washington Press.

LOURENCO, L.M. & SHIH, C. 1993 Characteristics of the plane turbulent near wake of a cylinder, a particle image velocimetry study. Data reported from Beaudan and Moin (1997).

MA, X., KARAMANOS, G.-S. & KARNIADAKIS, G. E. 2000 Dynamics and low-dimensionality of a turbulent near wake. *Journal of Fluid Mechanics* **410**, 29–65.

MAGAGNATO, F. 2000 *SPARC Structured PArallel Research Code*. Dept. of Fluid Machinery, University of Karlsruhe, Germany.

MAGAGNATO, F. & GABI, M. 2002 A new adaptive turbulence model for unsteady flow fields in rotating machinery. *International Journal of Rotating Machinery* **8** (3), 175–183.

MARTINELLI, L. 1987 Calculations of viscous flow with a multigrid method. PhD thesis, Mechanical and Aerospace Engineering Dept., Princeton University.

MITTAL, R. 1996 Progress on LES of flow past a circular cylinder. *Tech. Rep.*. Annual Research Briefs, Center for Turbulence Research, Stanford.

MITTAL, R. & MOIN, P. 1997 Suitability of upwind-biased finite difference schemes for large-eddy simulation of turbulent flow. *AIAA Journal* **35** (8), 1415–1417.

MOIN, P. & KIM, J. 1997 Tracking turbulence with supercomputers. *Scientific American* **276**, 62–68.

MOIN, P., SQUIRES, K., CABOT, W. & LEE, S. 1991 A dynamic subgrid-scale model for compressible turbulence and scalar transport. *Physics of Fluids* **A3(11)**, 2746–2757.

ONG, L. & WALLACE, J. 1996 The velocity field of the turbulent very near wake of a circular cylinder. *Experiments in Fluids* **20**, 441–453.

ÖNGÖREN, A. & ROCKWELL, D. 1988 Flow structure from an oscillating cylinder. Part 1: Mechanisms of phase shift and recovery in the rear wake. *Journal of Fluid Mechanics* **191**, 197–223.

PÉNÉAU, F., BOISSON, H.C., KONDJOYAN, A. & DJILALI, N. 2004 Structure of a flat plate boundary layer subjected to free-stream turbulence. *International Journal of Computational Fluid Dynamics* **18** (2), 175–188.

PÉNÉAU, F., DJILALI, N. & BOISSON, H.C. 2000 Large eddy simulation of the influence of a high free-stream turbulence on spatially evolving boundary layer. *International Journal of Heat and Fluid Flow* **21**, 640–647.

POPE, S. B. 2000 *Turbulent Flows*. Cambridge University Press.

ROSHKO, A. 1961 Experiments on the flow past a circular cylinder at very high reynolds numbers. *Journal of Fluid Mechanics* **10** (345-356).

SMAGORINSKY, J. 1963 General circulation experiments with the primitive equations, Part I: the basic experiments. *Monthly Weather Review* **91** (3), 99–164.

SPALART, P.R. & ALLMARAS, S.R. 1994 A one-equation turbulence model for aerodynamic flows. *Recherche Aérospatiale (also AIAA Paper 92-0429)* pp. 5–21.

SPEZIALE, C.G. 1985 Galilean invariance of subgrid-scale stress models in large-eddy simulation of turbulence. *Journal of Fluid Mechanics* **156**, 55–62.

SPEZIALE, C.G. 1998 Turbulence modeling for time-dependent RANS and VLES: A review. *AIAA Journal* **36** (2), 173–184.

SPEZIALE, C.G., ABID, R. & ANDERSON, E.C. 1992 Critical evaluation of two-equation models for near-wall turbulence. *AIAA Journal* **30** (2), 324–331.

STANSBY, P. K. 1976 The locking-on of vortex shedding due to the cross-stream vibration of circular cylinders in uniform and shear flows. *Journal of Fluid Mechanics* **74**, 641–665.

SUTHERLAND, W. 1893 The viscosity of gases and molecular force. *Phil. Mag.* **5**, 507–531.

SWANSON, R.C., RADESPIEL, R. & TURKEL, E. 1997 Comparison of several dissipation algorithms for central difference schemes. *AIAA Paper 97-1945* .

SWANSON, R.C., RADESPIEL, R. & TURKEL, E. 1998 On some numerical dissipation schemes. *Journal of Computational Physics* **147**, 518–544.

SWANSON, R.C. & TURKEL, E. 1992 On central-difference and upwind schemes. *Journal of Computational Physics* **101**, 292–306.

TANIDA, Y., OKAJIMA, A. & WATANABE, Y. 1973 Stability of a circular cylinder oscillating in a uniform flow. *Journal of Fluid Mechanics* **61** (4), 769–784.

TENNEKES, H. & LUMLEY, J. L. 1972 *A First Course in Turbulence*, 3rd edn. Cambridge, Massachussetts: MIT Press.

THOM, A. 1933 The flow past circular cylinders at low speeds. *Proceedings of the Royal Society (London)* **A141**, 651–666.

TREMBLAY, F., MANHART, M & FRIEDRICH, R. 2000 DNS of flow around a circular cylinder at a subcritical Reynolds number with cartesian grids. *Eighth European Turbulence Conference, Barcelona, Spain, EUROMECH, CIMNE* pp. 659–662.

VREMAN, A.W. 1995 Direct and large-eddy simulation of the compressible turbulent mixing layer. PhD thesis, Dept. of Applied Mathematics, University of Twente.

WHITE, F. M. 1991 *Viscous Fluid Flow*, 2nd edn. McGraw Hill.

WIESELSBERGER, C. 1921 New data on the law of hydro and aerodynamic resistance. *Physikalische Zeitschrift* **22**, 321–328.

WILLIAMSON, C. H. K. 1996 Vortex dynamics in the cylinder wake. *Annual Review of Fluid Mechanics* **28**, 477–539.

WILLIAMSON, C. H. K. & ROSHKO, A. 1988 Vortex formation in the wake of an oscillating cylinder. *Journal of Fluids and Structures* **2**, 355–381.

YOSHIZAWA, A. 1986 Statistical theory for compressible turbulent shear flows with the application to subgrid modelling. *Physics of Fluids* **29**, 2152–2164.

ZANG, Y., STREET, R.L. & KOSEFF, J.R. 1993 A dynamic mixed subgrid-scale model and its application to turbulent recirculating flows. *Physics of Fluids* **A5(12)**, 3186–3196.

ZDRAVKOVICH, M.M. 1982 Modification of vortex shedding in the synchronization range. *ASME Journal of Fluids Engineering* **104**, 513–517.

ZDRAVKOVICH, M.M. 1997 *Flow Around Circular Cylinders, Vol.1: Fundamentals*. Oxford University Press.

ZINGG, D.W., DE RANGO, S., NEMEC, M. & PULLIAM, T.H. 1999 Comparison of several spatial discretizations for the Navier-Stokes equations. *AIAA Paper 99-3260*